



저작자표시-비영리-변경금지 2.0 대한민국

이용자는 아래의 조건을 따르는 경우에 한하여 자유롭게

- 이 저작물을 복제, 배포, 전송, 전시, 공연 및 방송할 수 있습니다.

다음과 같은 조건을 따라야 합니다:



저작자표시. 귀하는 원저작자를 표시하여야 합니다.



비영리. 귀하는 이 저작물을 영리 목적으로 이용할 수 없습니다.



변경금지. 귀하는 이 저작물을 개작, 변형 또는 가공할 수 없습니다.

- 귀하는, 이 저작물의 재이용이나 배포의 경우, 이 저작물에 적용된 이용허락조건을 명확하게 나타내어야 합니다.
- 저작권자로부터 별도의 허가를 받으면 이러한 조건들은 적용되지 않습니다.

저작권법에 따른 이용자의 권리는 위의 내용에 의하여 영향을 받지 않습니다.

이것은 [이용허락규약\(Legal Code\)](#)을 이해하기 쉽게 요약한 것입니다.

[Disclaimer](#)

Thesis for the Degree of Doctor of Philosophy

Study on soluble semiconducting
functional materials for photovoltaic
application



by

Insoo Shin

Department of Physics
The Graduate School
Pukyong National University

February 2020

Study on soluble semiconducting functional materials for photovoltaic application

(광전소자를 위한 용액형 기능성 반도체 소재 연구)

Advisor: Prof. Sung Heum Park

by
Insoo Shin

A thesis submitted in partial fulfillment of the requirements
for the degree of

Doctor of Philosophy

in Department of Physics, The Graduate School,
Pukyong National University

February 2020

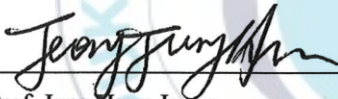
Study on soluble semiconducting functional materials for
photovoltaic application

A dissertation

by

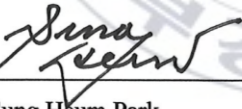
Insoo Shin

Approved by:



Prof. Jung Hyun Jeong

Chairman



Prof. Sung Heum Park

Member



Prof. Woon Ik Park

Member



Prof. Bo Ram Lee

Member



Prof. Semo Son

Member

February 2020

CONTENTS

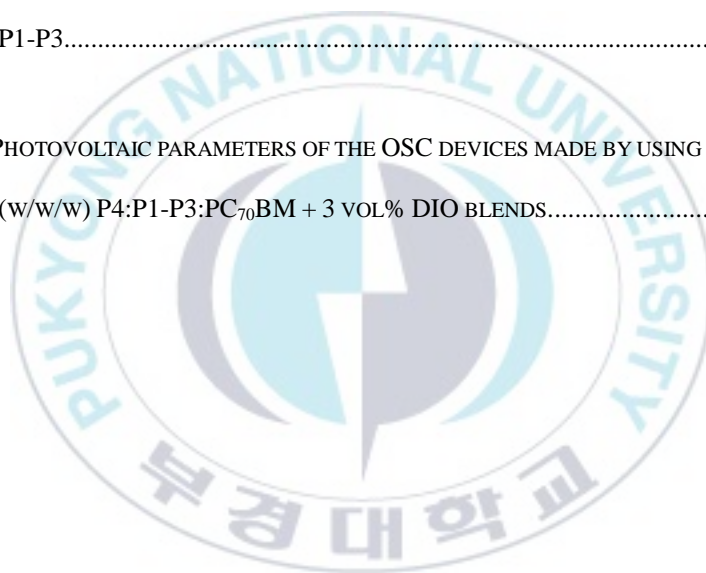
CHAPTER 1	INTRODUCTION	1
1.1	MOTIVATION	1
1.2	GENERAL BACKGROUND OF SOLAR CELLS	3
1.2.1	<i>Conjugated Polymer in Photovoltaic application</i>	3
1.2.2	<i>Perovskite in photovoltaic application</i>	5
1.2.3	<i>Structure and Mechanism of Solar Cell Operation</i>	7
1.2.4	<i>Characterization of photovoltaics</i>	11
1.3	FUNCTIONAL MATERIALS	22
1.3.1	<i>Role of Function Materials in Solar Cells</i>	22
1.3.2	<i>Mainstream Functional Materials in Research</i>	24
CHAPTER 2	EXPERIMENTAL	26
2.1	MATERIAL PREPARATION	26

2.1.1	<i>Polymeric Functional Materials</i>	26
2.1.2	<i>Metal Oxide based Functional Materials</i>	27
2.2	DEVICE PREPARATION	28
2.2.1	<i>Polymer Solar Cells</i>	28
2.2.2	<i>Perovskite Solar Cells</i>	29
CHAPTER 3 DESIGN AND CHARACTERIZATION OF NOVEL FUNCTIONAL MATERIALS		30
3.1	NOVEL POLYMERIC FUNCTIONAL MATERIALS	30
3.1.1	<i>Introduction</i>	30
3.1.2	<i>Result and Discussion</i>	34
3.1.3	<i>Summary</i>	46
3.2	INCORPORATION OF NOVEL POLYMERIC FUNCTIONAL MATERIAL IN ORGANIC BHJ SOLAR CELL	47
3.2.1	<i>Introduction</i>	47
3.2.2	<i>Result and Discussion</i>	51

3.2.3	<i>Conclusion</i>	61
CHAPTER 4	STUDY ON THE NOVEL METAL OXIDE BASED FUNCTIONAL MATERIALS	62
4.1	PREPARATION AND CHARACTERIZATION OF NOVEL METAL OXIDE BASED FUNCTIONAL MATERIALS	62
4.1.1	<i>Introduction</i>	62
4.1.2	<i>Result and Discussion</i>	63
4.1.3	<i>Conclusion</i>	75
4.2	INCORPORATION OF NOVEL METAL OXIDE BASED FUNCTIONAL MATERIAL IN PEROVSKITE SOLAR CELL.....	76
4.2.1	<i>Impact of morphology on perovskite solar cells</i>	77
4.2.2	<i>Incorporation of metal oxide based functional material in perovskite</i>	81
CHAPTER 5	CONCLUSION	87
CHAPTER 6	REFERENCES	89

LIST OF TABLES

TABLE 3-1. PROPERTIES OF TPTI- AND TPTK- BASED POLYMERS.	36
TABLE 3-2. CARRIER MOBILITIES OF TPTK- AND TPTI-BASED POLYMERS	42
TABLE 3-3. MOLECULAR WEIGHT, PHOTO-PHYSICAL, AND ELECTROCHEMICAL PROPERTIES OF P1-P3.....	52
TABLE 3-4. PHOTOVOLTAIC PARAMETERS OF THE OSC DEVICES MADE BY USING X:X:X (w/w/w) P4:P1-P3:PC ₇₀ BM + 3 VOL% DIO BLENDS.....	57



LIST OF FIGURES

FIGURE 1-1. CRYSTALLINE STRUCTURE OF PEROVSKITE.....	6
FIGURE 1-2. GENERAL STRUCTURE OF PLANAR STRUCTURE SOLAR CELL. (UP : PEROVSKITE SOLAR CELL, DOWN : POLYMER SOLAR CELL).....	8
FIGURE 1-3. J-V CHARACTERISTICS UNDER THE DARK AND LIGHT CONDITION.	11
FIGURE 1-4. EQUIVALENT CIRCUIT MODEL FOR IDEAL AND PRACTICAL PHOTOVOLTAIC DEVICE.	12
FIGURE 1-5. J-V CHARACTERISTICS FOR IDEAL AND PRACTICAL DIODE.	13
FIGURE 1-6. EQUIVALENT CIRCUIT MODEL FOR PRACTICAL DIODE.....	14
FIGURE 1-7. EQUIVALENT CIRCUIT MODEL FOR PHOTOVOLTAICS UNDER DARK AND UNDER LIGHT ILLUMINATION.	15
FIGURE 1-8. J-V CHARACTERISTICS OF PHOTOVOLTAICS UNDER ILLUMINATION.	16
FIGURE 3-1. CHEMICAL STRUCTURE OF TPT, TPTI, TPTK, AND TPTI- AND TPTK- BASED POLYMERS DISCUSSED IN THIS STUDY.....	33

FIGURE 3-2. ABSORPTION SPECTRA OF THE POLYMER P(BDTT-TPTI) AND P9BDTT-TPTK (A), P(DTBT-TPTI) AND P(DTBT-TPTK) (B), P(DKPP-TPTI) AND P(DKPP-TPTK) (C), AND THE OPTIMIZED STRUCTURES OF TPTI AND TPTK DERIVATIVES (D).	35
FIGURE 3-3. CV SPECTRA OF P(BDTT-TPTK), P(DTBT-TPTK), P(DKPP-TPTK), AND P(DTBT-TPTI).....	37
FIGURE 3-4. J-V CHARACTERISTICS OF OSCs FABRICATED USING P(BDTT-TPTK):PC ₇₀ BM (A), P(DTBT-TPTK):PC ₇₀ BM (B), P(DKPP-TPTK):PC ₇₀ BM (C), AND P(DTBT-TPTI):PC ₇₀ BM (D), BLENDS UNDER DIFFERENT CONDITIONS SUCH AS DIFFERENT POLYMER:PC ₇₀ BM RATIOS (1:1 WT%, 1:2 WT%, AND 1:3 WT%).....	38
FIGURE 3-5. IPCE SPECTRA OF THE OSCs	39
FIGURE 3-6. J-V CURVES OF HOLE-ONLY (ITO/PEDOT:PSS/POLYMER:PC ₇₀ BM /MoO ₃ /AL) DEVICES (A), AND ELECTRON-ONLY (ITO/ZNO/POLYMER:PC ₇₀ BM/AL) DEVICES (B).....	41
FIGURE 3-7. (A AND B) SMALL ANGLE X-RAY DIFFRACTION (SAXS) AND (C AND D) WIDE X- RAY DIFFRACTION (XRD) SPECTRA OF POLYMER AND POLYMER:PC ₇₀ BM FILMS.	43
FIGURE 3-8. OPTIMIZED STRUCTURE OF THE REPEATING UNITS OF POLYMERS P(BDTT-TPTI), P(BDTT-TPTK), AND P(DTBT-TPTI).	44

FIGURE 3-9. CHEMICAL STRUCTURES OF PBDTPPD AND PBDTDTFFBT	49
FIGURE 3-10. SYNTHETIC ROUTE TO P1-P3.	50
FIGURE 3-11. FILM STATE ABSORPTION SPECTRA (A), CYCLIC VOLTAMMOGRAM (B) FOR P1-P3.	51
FIGURE 3-12. FILM STATE XRD (A), AND SAXS SPECTRA (B) FOR P1-P3.	52
FIGURE 3-13. (A) STRUCTURES OF DONOR AND ACCEPTOR MATERIALS. (B) ABSORPTION SPECTRA OF DONOR POLYMERS. (C) ENERGY LEVELS OF DONOR AND ACCEPTOR MATERIALS. (D-F) THE J-V CURVES OF THE PSCS MADE BY USING DIFFERENT RATIOS OF P4:P1-P3:PC70BM + 3 VOL% DIO BLENDS.	54
FIGURE 3-14. THE IPCE SPECTRA OF THE BI- AND TER-PSCS MADE BY USING DIFFERENT RATIOS OF P4:P1-P3:PC70BM + 3 VOL% DIO BLENDS.	56
FIGURE 3-15. J-V CURVES FOR HOLE-ONLY (A) AND ELECTRON-ONLY (B) DEVICES.	58
FIGURE 3-16. SAXS AND XRD (A AND B) SPECTRA FOR THE ACTIVE LAYER FILMS. (INSET : SMOOTHENED XRD SPECTRA)	59
FIGURE 3-17. TEM IMAGES FOR THE ACTIVE LAYER FILMS.....	60
FIGURE 4-1. CONCEPTUAL FIGURE OF THIS WORK: A COMPARISON BETWEEN SOLID-STATE	

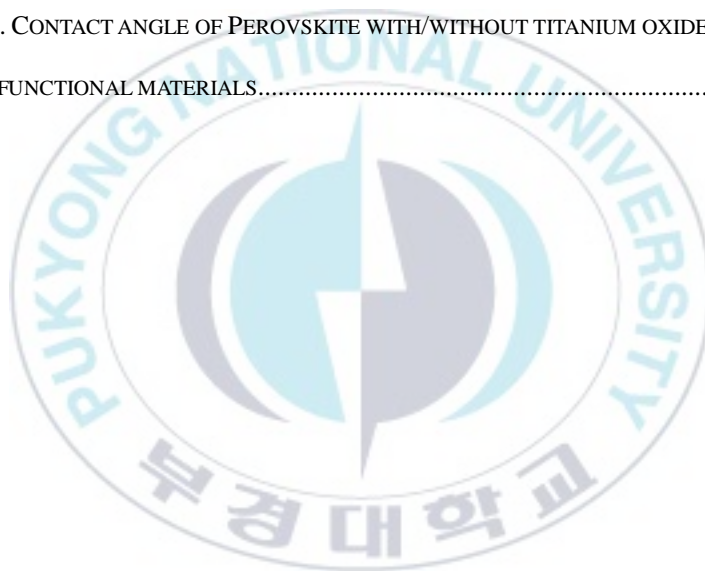
METAL OXIDE PRECURSOR AND CONVENTIONAL SOL-GEL DERIVED METAL OXIDE PRECURSOR.....	63
FIGURE 4-2. ABSORPTION SPECTRA OF STO (A), AND THE PICTURE OF STO(B) AND PTO BEFORE/AFTER STORAGE IN AMBIENT CONDITION FOR 10 DAYS AND SOLUBILITY OF PTO IN VARIOUS SOLVENT(C).....	64
FIGURE 4-3. THE XPS SPECTRA OF O1s IN STO AND PTO. (A) O1s SPECTRA OF STO BEFORE EXPOSURE TO AIR, (B) AFTER EXPOSURE TO AIR. (C) O1s SPECTRA OF PTO BEFORE EXPOSURE TO AIR, (D) AFTER EXPOSURE TO AIR.	65
FIGURE 4-4. THE CHEMICAL PROPERTIES OF PTO. (A) XPS N1s SPECTRA (INSET : N1s SPECTRA OF TiO ₂), (B) FTIR, AND (C) XRD OF PTO FILM.....	67
FIGURE 4-5. PROPERTIES OF PTO FILM. (A) ABSORPTION SPECTRA, (B) FE-SEM IMAGE, AND (C) CONTACT ANGLE OF PTO FILM, (D) WORK FUNCTION OF ALUMINUM WITH/WITHOUT PTO FILM ON TOP.....	68
FIGURE 4-6. PERFORMANCE OF OSCs WITH/WITHOUT PTO LAYER. (A) J-V CHARACTERISTICS AND (B) NORMALIZED PCE AS A FUNCTION OF STORAGE TIME.	69
FIGURE 4-7. ROLE OF PTO FILM AS AN OPTICAL SPACER FOR OSCs. (A) IPCE AND (B) ABSORPTION SPECTRA OF OSCs WITH/WITHOUT PTO IN REFLECTION GEOMETRY.	70

FIGURE 4-8. (A) J_{SC} AND (B) V_{OC} DEPENDENCE UPON INCIDENT LIGHT INTENSITY, (C) DARK J-V CHARACTERISTICS OF OSCs WITH/WITHOUT PTO LAYER, AND (D) CALCULATED IDEALITY FACTOR FROM DARK J-V CHARACTERISTICS.	72
FIGURE 4-9. NYQUIST PLOTS OF OSCs WITH(A) AND WITHOUT PTO LAYER(B) AND EQUIVALENT CIRCUIT MODEL WITHOUT(C) AND WITH ADDITIONAL INTERFACIAL TRAP.(D).....	73
FIGURE 4-10. PERFORMANCE OF SOLAR CELLS WITH/WITHOUT PTO LAYER. (A) J-V CHARACTERISTICS AND (B) IPCE OF OSCs WITH PCDTBT:PC ₇₀ BM. (C) J-V CHARACTERISTICS AND (D) IPCE OF MAPbI ₃ PEROVSKITE SOLAR CELLS.	74
FIGURE 4-11. CONCEPT OF HAAP	77
FIGURE 4-12. THE TOP-VIEW FE-SEM IMAGES OF THE PEROVSKITE FILMS FORMED USING THE (A) CONVENTIONAL, (B) MPT, (C) HAAP METHOD AND (D-F) GRAIN SIZE DISTRIBUTIONS OF THE FILMS.	79
FIGURE 4-13. ABSORPTION SPECTRA OF PEROVSKITE FILMS	80
FIGURE 4-14. IMPACT OF INCORPORATING PTO ON MORPHOLOGY OF PEROVSKITE	81
FIGURE 4-15. XRD SPECTRA OF PEROVSKITE FILMS WITH VARIOUS QUANTITY OF PTO INCORPORATION.....	82

FIGURE 4-16. IMPACT OF INCORPORATING PTO IN PERFORMANCE OF PEROVSKITE SOLAR CELLS. (A) J-V CHARACTERISTICS OF DEVICE, (B) LIGHT INTENSITY VERSUS JSC, AND (C) LIGHT INTENSITY VERSUS VOC OF THE DEVICE WITH/WITHOUT PTO.84

FIGURE 4-17. CONTACT ANGLE OF VARIOUS TITANIUM OXIDE BASED FUNCTIONAL MATERIALS85

FIGURE 4-18. CONTACT ANGLE OF PEROVSKITE WITH/WITHOUT TITANIUM OXIDE BASED FUNCTIONAL MATERIALS.....86



광전소자 응용을 위한 용액형 기능성 반도체 소재 연구

신인수

부경대학교 대학원 물리학과

요 약

최근 화석연료의 매장량 한계와 화석연료의 사용으로 발생한 환경문제로 인해 대체에너지원에 대한 수요가 증가하고 있으며, 그 중에서도 환경친화적이고 지리적조건의 영향에서 비교적 자유로운 태양전지는 차세대 에너지원으로 각광받고 있다. 공액고분자와 유-무기 하이브리드 페로브스카이트로 대표되는 저온 용액공정 기반의 태양전지는 저렴한 대면적 공정이 가능하며 전기적특성 및 광학적 특성이 뛰어나 초저가 대량 생산형 태양전지 시장의 핵심소재로 떠오르고 있다.

용액공정 기반 소자와 같은 평판(planar) 구조 태양전지에서 전하의 이동은 층간 계면의 전기/화학적 특성 및 활성층의 전하 이동도에 큰 영향을 받고, 전하의 이동도는 모폴로지에 영향을 받기 때문에, 용액공정 기반 소자에서 계면특성과 더불어 모폴로지를 조절하는 것이 매우 중요하다. 하지만 용액공정을 통해 형성된 박막은 여러 결정립으로 구성되거나 무작위적으로 상분리된 다중도메인(multi-domain) 박막을 형성하며, 박막의 형성이 공정 조건에 매우 민감하기 때문에 박막의 결정성 및 도메인 크기와 배열을 비롯한 모폴로지의 조절이 어렵다. 따라서 소자의 계면특성 및 모폴로지를 조절하는 연구가 매우 중요하며, 특히 소자에 도입하여 계면특성 및 모폴로지를 효과적으로 조절할 수 있는 기능성소재에 대한 연구가 필요하다.

본 연구에서는 활성층의 모폴로지와 계면의 특성을 조절할 수 있는 저온 용액공정이 가능한 새로운 고분자 및 금속산화물 기반의 기능성소재를 개발하였고, 각 기능성소재를 공액고분자와 유무기 하이브리드 페로브스카이트 태양전지에 각각 도입하여 이에 따른 소자의 특성변화를 분석하였다. 각 기능성소재를 활성층 내부에 도입한 결과, 활성층 박막의 결정성 및 결정 배열과 도메인 크기 및 커버리지(coverage)를 비롯한 모폴로지의 전반적인 향상이 나타났으며, 이에 따라 활성층 내 전하 수송

특성이 향상되었다. 또한, 기능성소재를 활성층의 계면에 도입한 결과, 계면에서 전하 추출특성과 소자의 동작수명이 크게 향상되었다.



Chapter 1 Introduction

1. 1 Motivation

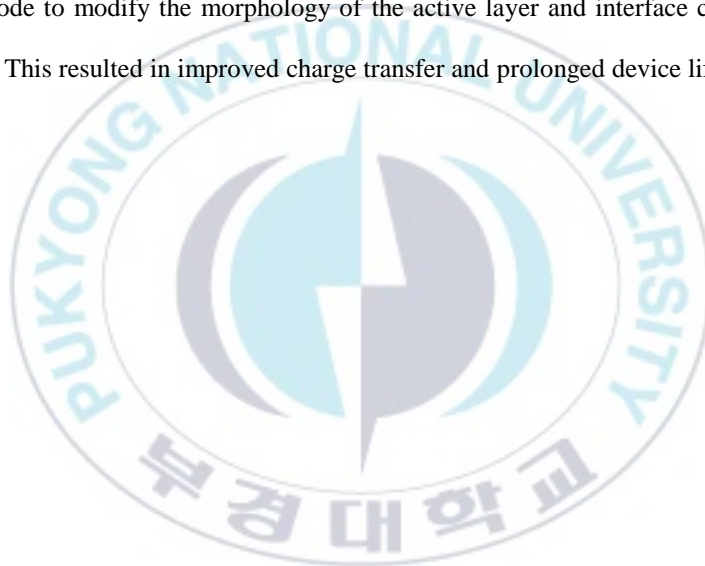
It goes without saying that our lives heavily depend on energy and with the world's population on the increase, our needs are growing further every year. While fossil fuels have served our civilization as the biggest energy supply for more than two centuries, there is no doubt that we are facing the limit of fossil fuel reserves. Furthermore, the irreversible environmental damage resulting from their use is increasingly becoming a threat to world security. Obviously, our reliance on this finite resource has to diminish, and we soon have to come up with alternatives that are economically viable and environmentally friendly.

Renewable energy sources (e.g. wind, solar, tidal energy) are considered as promising alternatives to fossil fuels. In particular, solar cells have the potential to afford the high energy demand in every region of the world because can be quickly and economically deployed owing to their modular design. There are numerous studies on photovoltaic technologies with various structures and materials. Of the current technology of solar cells referred to as 3rd generation solar cells, solution processable planar structured solar cells have been intensively studied over the last decade. This is due to their high functionality and economic feasibility.

Since the performance of the PSC devices relies strongly on the nature of the interface, the research on interfacial layer engineering has become more intense as the spotlight on PSCs increases. Numerous types of interfacial layers have been studied and incorporated into various interfaces within PSCs, have accordingly shown various functionalities such as injecting/extracting/blocking of charges selectively at the interface, modifying the light

interference within the device, enhancing device stability, and modifying the device morphology. Overall, the huge improvement was noted on the power conversion efficiency(PCE) of PSCs is accompanied by desirable influences on the device characteristics such as enhanced device stability and reproducibility.

In this work, I developed new soluble functional materials, each based on conjugated polymers and metal oxide, and investigated the impact of functional materials on the PSCs characteristics. Each functional material was incorporated in the active layer and the interface of the electrode to modify the morphology of the active layer and interface characteristics, respectively. This resulted in improved charge transfer and prolonged device lifetime.



1. 2 General Background of Solar Cells

1.2.1 Conjugated Polymer in Photovoltaic application

Organic polymers are large 1-dimensional linear molecules with a 1-dimensional carbon chain and a molecular weight exceeding 10,000 grams/mole. Carbon atoms have four covalent electrons that usually form two hybrid structures in a molecule – a tetrahedral configuration and a hexagonal configuration. Conventional polymer molecules have a form tetrahedral configuration in the molecule with saturated C-C bonds. Such polymers find applications that range from fabrics to engineering plastic. But they do not exhibit any electrical conductivity since all covalent electrons are bounded by chemical bonds.

In contrast, conjugated polymers that were discovered by Heeger, MacDiarmid, and Shirakawa can become electrically conducting doping.¹ Conjugated polymer molecules have a hexagonal configuration. In the hexagonal configuration, three of four covalent electrons of carbon form covalent bonds with neighboring atoms while the fourth electron forms π -bond with neighboring carbon atoms due to the attractive interaction with carbon nuclei. In contrast with covalent bonds, the π -bond is delocalized along the conjugated molecule chain. Hence, conjugated polymers are natural semiconductors and can even be made to conduct electricity using doping processes.² Thus, conjugated polymers not only share advantages of conventional polymers (plastics) such as solution processability and flexibility but also have a band gap that can be controlled by altering the chemical structure.³

In the field of the solar cell, the bulk heterojunction(BHJ) of conjugated polymer with fullerene derivatives are mostly studied.^{4,5} Recently, organic molecule based various non-

fullerene acceptors (NFAs) are emerging as an alternative acceptor, performing higher efficiency ~17 %, originated from extended light absorption spectrum and reduced open-circuit voltage loss.⁶ However, low stability under the ambient condition still remains a severe issue for its commercialization.⁷⁻⁹



1.2.2 Perovskite in photovoltaic application

Perovskite is the name of mineral, CaTiO_3 which found by Gustav Rose and named after Russian mineralogist L. A. Perovski.¹⁰ Later on, the perovskite became a name of class of compounds with the formula of ABX_3 , the same type of crystal structure with CaTiO_3 . Among the various class of perovskites, the organic-inorganic halide perovskite attracts great attention recently, due to their superior optical/electrical properties, making them a prospective material for optoelectronic applications. The chemical formula for organic-inorganic halide perovskite is ABX_3 , consisting of monovalent large organic cation (A : aliphatic or aromatic ammonium) and divalent metal cation (B : Pb^{2+} , Sn^{2+} , Ge^{2+} , etc...) with halogen anions (X : Cl^- , Br^- , I^-). Figure 1-1 shows the structure of ABX_3 perovskite crystal. The ideal structure is a cube consisting of corner-sharing BX_6 octahedron with A cation at the center as illustrated in Figure 1-1. However, structural distortions are commonly found, since the radius and outer electronic structure of organic cations, metal ions and halogen anions will affect the octahedron structure of BX_6 . Since many physical properties including electronic, magnetic and dielectric properties of perovskite are depend severely on this distortion, the properties could be easily fine-tuned by substitution of cations.

In the field of solar cells, MAPbI_3 or FAPbI_3 has mostly been studied, and currently, their mixture with MAPbBr_3 or FAPbBr_3 is commonly used for higher performance and better stability. Since the halide perovskite was first successfully incorporated in the solar cell in 2009 by T. Miyasaka, and in a solid-state solar cell in 2012 by Nam-Gyu Park, halide perovskite has attracted prominent attention in the field of photovoltaic application, demonstrated a meteoric rise in power conversion efficiency and now exceeded all other thin-

film technologies. Halide perovskite exhibits several outstanding properties for photovoltaic applications such as high optical coefficient, tunable bandgap (generally 1.4~2.3 eV), low exciton binding energy (<50 meV), and long exciton diffusion length(100~1000 nm for thin film and ~175 μm for single crystal) and lifetime. However, the low reproducibility due to random morphology from solution-processed film and low chemical stability, especially, the low stability toward the humidity in ambient air is considered as a major hindrance for its commercialization.

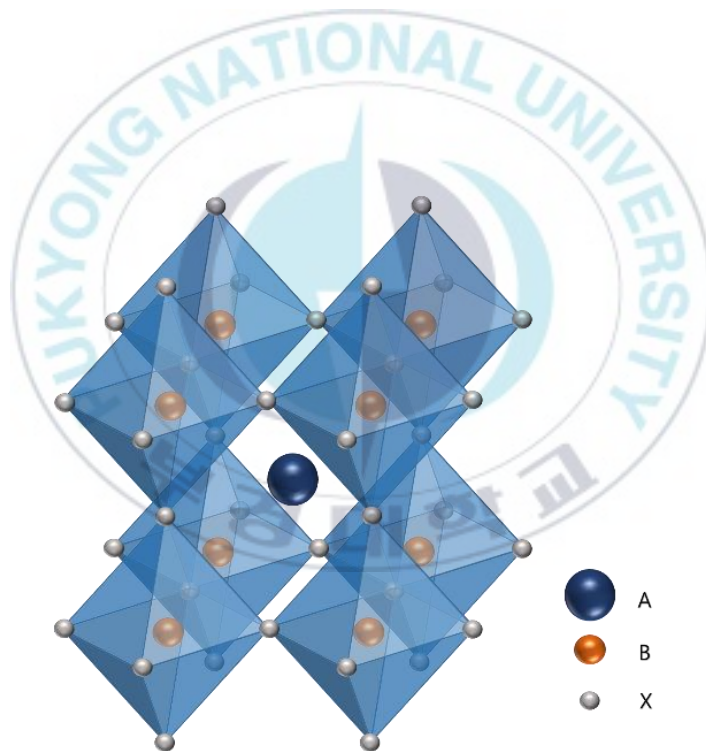


Figure 1-1. Crystalline structure of Perovskite

1.2.3 Structure and Mechanism of Solar Cell Operation

The solution-processable planar-structured solar cells (PSCs) including polymer solar cells (OSCs) and perovskite solar cells (PeSCs) have many common features that originated from the similarity of the device structure. Although the study on PeSCs started from the liquid-electrolyte based dye-sensitized solar cells (DSSCs), however, currently the device structure became quite similar to OSCs as the DSSCs changed from liquid to solid state. Since, J. Jeng et al., have demonstrated that the mesoscopic structure is not essential for device operation,¹¹ many studies have been attempted with a planar structure having many significant advantages in device application.¹²⁻¹⁵

Figure 1-2 shows the general structure of PeSCs and OSCs in planar configuration. Generally, the PSCs have an MSM architecture, which has semiconducting layers sandwiched between metal contact and least one of them is transparent, letting the light incident to the active layer. When the light absorbed by active layer, the absorbed photon generates exciton which strongly bounded electron-hole pair. The binding energy of each bounded pair determined by the properties of active layer, can be divided into strongly bounded pair (Frankel exciton, OSCs), and weakly bounded pair (Mott-Wannier exciton). In the case of Mott-Wannier type exciton (e.g. Perovskite), readily separated at the room temperature, results in separated charges. On the other hand, Frankel type exciton can't be separated by the thermal energy at room temperature (e.g. Organic polymer), requires an additional component to separate the bounded exciton (acceptor) into holes and electrons. Each separated charges extracted by the built-in electric field toward the corresponding electrodes. In MSM configuration, the built-in electric field is determined by the electrode and functional materials

at the interface, since the built-in electric field is formed by the contact work-function (effective work-function) difference between each electrode, and the effective work-function is strongly affected by the functional materials at the interface. Forasmuch as the operation of solar cell is a competition between generation/dissociation of exciton and transport toward the corresponding electrodes, and trap/accumulate/recombination of exciton and separated charges, the functional layer which controls the built-in electric field, interfacial energy alignment, trap density at the interface, and even the morphology of the active layer, holds significant importance on the PSCs operation. Because of the difference in the electronic properties of the active layer, the detailed mechanism and the role of functional material could be different for OSCs and PeSCs.



Figure 1-2. General structure of planar structure solar cell. (up : Perovskite solar cell, down : Polymer solar cell)

(1) Polymer solar cell

The BHJ polymer solar cell is made by a mixture of donor (conjugated polymer) and acceptor (generally, fullerene derivatives). As mentioned above, the excitons are strongly bounded, and the dissociation of excitons only occurs at the interface between donor and acceptor. Therefore, the ideal bulk heterojunction refers to the junction between evenly blended donor polymer and acceptor component for having sufficient area of D / A interface within the active layer. Since the diffusion length of exciton generated within the organic semiconductor is very short, having nanometer-scale of finely inter-mixed domains and continuous interpenetrating network with well-connected domains at the same time is significant for device operation.^{1,2}

On the other hand, because of this complex architecture of active layer, in practice, the BHJ OSCs contain considerable traps and often undergo non-ideal charge transfer due to incomplete interpenetrating network, caused by the randomness of film fabrication procedure.³⁻⁵ Further, the non-ideal contact at the interface with electrode involves charge accumulation and recombination due to the energetic barrier at the interface, and thus, hinders charge extraction.⁶⁻⁹ These issues could be suppressed by adopting proper functional materials at the interface, reducing energetic barriers and enhancing built-in potential, the driving force to extract the separated charges. Recently, many attempts been made to achieve ideal charge transfer within the active layer by optimizing interpenetrating network and carrier mobility of active layer through incorporating functional material into BHJ blend (ternary BHJ), and demonstrated impressive results.¹⁰⁻¹⁵

(2) Perovskite solar cell

In general, the structure of PeSCs can be categorized into mesoscopic and planar structure, contingent on the existence of an oxide skeleton layer. The incorporation of an oxide skeleton induces several pros and cons in terms of device performance and fabrication procedure, however, regardless of the oxide skeleton, with respect to the carrier dynamics, the structure of PeSCs can be simplified to p-i-n (or n-i-p) structure.

Contrary to the OSCs, halide perovskite generates weakly bounded exciton or readily separated charge pairs under illumination due to strong dielectric screening effect originate from high dielectric constant. Furthermore, halide perovskite demonstrates remarkably long-range ambipolar charge transport properties, which allows forming sufficient thickness of the active layer (~400 nm) for light harvesting. Such outstanding electrical properties of perovskite allows efficiently collecting the charges generated from light absorption.

On the other hand, the morphology of the crystalline perovskite film could significantly be affected by the fabricate condition and induces considerable loss during charge collection process due to the substantial traps and defects at the grain boundary. Since the morphology of the solution-processed film is strongly affected by the interface. Further, the surface states such as defect, trap density, and energetic alignment at the interface are determined by the interface. Therefore, the incorporation of adequate functional materials at the interface holds significant importance on the performance of PeSCs. Recently, many research has been done with functional materials to suppress the defects of perovskite film by applying the functional material prior to forming a complete perovskite film, resulting in outstanding performance and stability by successfully suppressing the traps and ion-migration.

1.2.4 Characterization of photovoltaics

(1) Current density- voltage characteristics

The most important parameter of a photovoltaic is the 'light to electrical power conversion efficiency'(PCE). The current density – voltage (J-V) characteristics are one of the most commonly used methods to determine the performance of photovoltaics including PCE. In this measurement, each electrode of the solar cells is connected and the flowing current through the cell at certain bias voltages are measured. This measurement is performed for a range of bias voltages as seen in Figure 1-3. This process can be performed either under the illumination (light J-V) or under the dark condition (dark J-V).

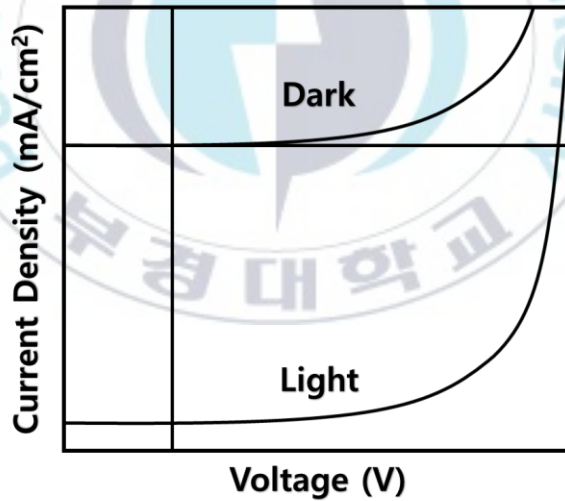


Figure 1-3. J-V characteristics under the dark and light condition.

(1)-1 Dark J-V characteristics

From the J-V characteristics measured under the dark condition, the carrier transport within the photovoltaic device can be analyzed with the Shockley equation. Under the dark condition (without incident photon), the photovoltaics are behaving as a diode which follows the Shockley equation. The general Shockley equation for ideal diode¹⁶ is given as follow;

$$J(V) = J_0 \left[\exp\left(\frac{qV}{k_B T}\right) - 1 \right] \quad (1.1)$$

where J_0 is the reverse saturation current density, V is the applied bias, k_B is Boltzmann constant, and T is temperature. However, in practical devices, the J-V characteristics deviate from the ideal behavior due to the resistance and defects. To take account the resistance and the defects, the equivalent circuit model (Figure 1-4) and the Shockley equation for practical diode^{17,18} is modified as follow;

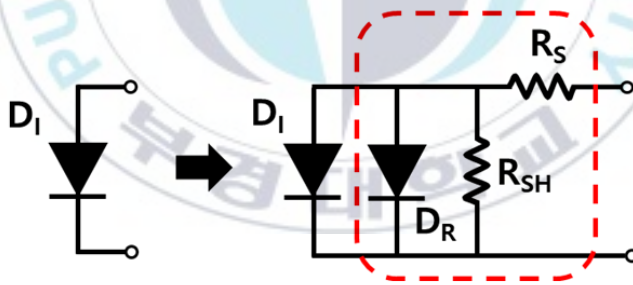


Figure 1-4. Equivalent circuit model for ideal and practical photovoltaic device.

$$J(V) = J_R \left[\exp\left(\frac{q(V - JR_S)}{n_R k_B T}\right) - 1 \right] + J_I \left[\exp\left(\frac{q(V - JR_S)}{n_I k_B T}\right) - 1 \right] + \left[\frac{(V - JR_S)}{R_{sh}} \right] \quad (1.2)$$

where R_S is series resistance, R_{SH} is shunt resistance, and n is the ideality factor. The R_S and

R_{SH} correspond to series resistance and the leakage path exists within the device, respectively. The voltage term is modified to $V - R_S J$, in accordance with the voltage drop at the series resistance R_S . And the third term in the equation corresponds to ohmic shunt current caused by a parallel resistance R_{sh} . That resistances are defined to be area related (Ωcm^2). From Figure 1-4, the additional diode component D_R corresponds to recombination current, in accordance with the Shockley-Read-Hall (SRH) recombination, the theory of recombination via traps, where D_I is ideal diode corresponding to drift current. Therefore, the ideality factor n_I is often assumed to be 1, whereas n_R is set to 2. As shown in the semi-logarithmic dark J-V characteristics in Figure 1-5, the R_S and R_{SH} are corresponding to the deviation in the high (region III) and low voltage region (region I), respectively. The J_R affects the slope of the semi-logarithm J-V plot, majorly in the region II. As described in Figure 1-5, the slope in the region II approaches the value of recombination current ($n_R = 2$, according to SRH formalism) as recombination current dominates the current within the device.

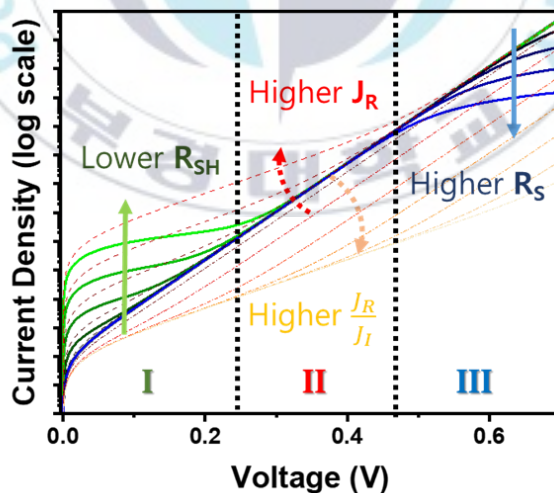


Figure 1-5. J-V characteristics for ideal and practical diode.

The practical Shockley equation can be simplified to the one diode model for limited bias range (usually between the maximum power point and V_{oc} of the photovoltaic device) as Figure 1-6 and Equation(1.3).¹⁸

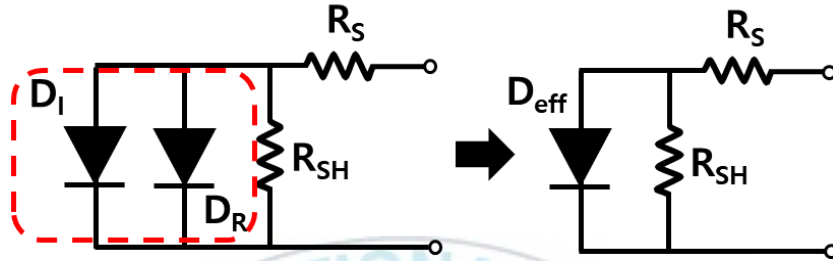


Figure 1-6. Equivalent circuit model for practical diode.

$$J(V) = J_0 \left[\exp \left(\frac{q(V - JR_S)}{n^{eff} k_B T} \right) - 1 \right] + \left[\frac{(V - JR_S)}{R_{sh}} \right] \quad (1.3)$$

From Equation(1.3), the contribution of recombination current is contained in J_0 and n^{eff} . As mentioned above, the contribution of trap-assisted recombination on the net dark current is reflected as a deviation in the slope of the semi-logarithm J-V plot in region II, which corresponds to a change in effective ideality factor from ‘ideal’($n=1$) to ‘SRH recombination’($n=2$). Therefore, the effective dark ideality factor (n^{eff} , or n_d), the ideality factor for the net dark current in region II, is concerned as a strong indicator of the effect of trap-assisted recombination on the diode current.

(1)-2 Light J-V characteristics

In the presence of light illumination, the equivalent circuit model for solar cells is described by the combination of a photo-generated controlled current source J_{ph} with the diode as shown in Figure 1-7. Accordingly, the general Shockley equation for photovoltaics^{19,20} are given as follow;

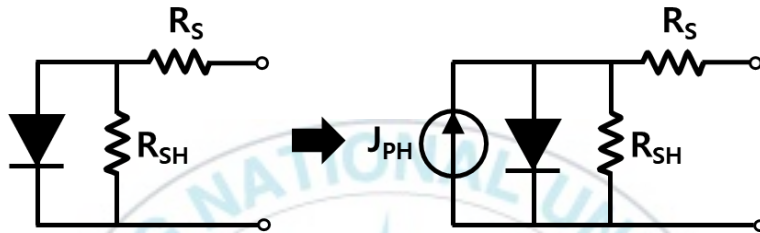


Figure 1-7. Equivalent circuit model for photovoltaics under dark and under light illumination.

$$J(V) = J_0 \left[\exp \left(\frac{q (V - J R_s)}{n_l k_B T} \right) - 1 \right] + \left[\frac{(V - J R_s)}{R_{sh}} \right] - J_{ph} \quad (1.4)$$

where, J_{ph} is the photo-generated current from photovoltaics, and n_l is the effective light ideality factor of the photovoltaic device, respectively.

From the J-V characteristics under the illumination, a few important parameters can be extracted. The most prominent factors are the short circuit current density (J_{sc}), open circuit voltage (V_{oc}), fill factor (FF), and power conversion efficiency (PCE).

Short circuit current density (J_{sc}) is the current flowing through the photovoltaic device when the external bias is zero (short circuit condition) as marked on the J-V curve in Figure 1-8. The J_{sc} characterizes the maximum current that the photovoltaic device can provide. There

are several factors that affect J_{sc} such as the number of incident photons, the spectrum of the incident light, the optical properties of the absorber, and the collection probability of photovoltaic device.

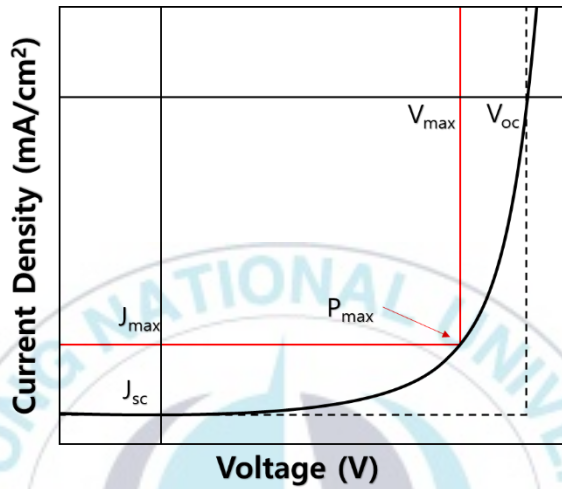


Figure 1-8. J-V characteristics of photovoltaics under illumination.

From the general Shockley equation for photovoltaics(Equation(1.4)), the photocurrent at zero bias (J_{sc}) is given as Equation(1.5).^{20,21}

$$J_{sc} = -J_{ph} = -edGP_c(I, V) \quad (1.5)$$

Where G is the generation rate of free charge carriers per unit volume, d is the distance between each electrode, and $P_c(I, V)$ is the charge collection probability. Under short circuit condition, most of the charges generated within the active layer of the photovoltaic device are swept out of the device prior to recombination due to a strong internal electric field ($P_c(I, V=0) \rightarrow 1$). Therefore, for an ideal device, the J_{sc} solely determined by the generation rate, hence, J_{sc} has a linear dependency on the incident light intensity (P_{in}).

Open circuit voltage (V_{oc}) is the output voltage from the photovoltaic device when the current is zero (open circuit condition). Under the open circuit condition, the photo-generated charges will accumulate at the corresponding electrodes, offset the built-in potential. Since the generation and recombination of carriers are counterbalanced, the system became a quasi-equilibrium state. Under this condition, the potential difference between each electrode generates the V_{oc} , which is the maximum voltage that the photovoltaic device can provide.

In general, the V_{oc} is determined by the difference in the quasi-Fermi levels of hole and electron at the charge extraction contact, formed by light illumination. Therefore, the V_{oc} is not only affected by the energy levels of donor and acceptor (or CBM and VBM of the absorber in the case of single absorber layer) but also affected by the interfacial contact, electrode, carrier accumulation and recombination that can affect to the distribution of photo-generated carriers. From the general Shockley equation for photovoltaics (Equation(1.4)), the V_{oc} , where $J=0$, and $R_{sh} \gg R_s$ is given as Equation(1.6).

$$V_{OC} = \frac{n_i k_B T}{q} \ln \left(\frac{J_{ph}}{J_0} + 1 \right) \quad (1.6)$$

Equation(1.6) shows that the V_{oc} has inversely proportional to J_0 and directly proportional to J_{ph} and n_i .

Fill factor (FF) is the ratio between the maximum power of the device to the product of I_{sc} and V_{oc} . The FF is determined by carrier extraction efficiency which strongly affected by carrier mobility, resistance, and dominant recombination mechanism. Therefore, the FF is an important parameter which reflects the ideality of carrier transport within the photovoltaic device.

$$FF = \frac{V_{max} \times I_{max}}{V_{oc} \times I_{sc}} \quad (1.7)$$

Power conversion efficiency (PCE) is defined by the ratio between maximum power of the device to the power of incident light. PCE is the most significant parameter which represents the performance of photovoltaic.

$$PCE = \frac{P_{out}}{P_{in}} = \frac{V_{oc} \times J_{sc} \times FF}{P_{in}} \quad (1.8)$$



(2) Light intensity dependent measurement

According to the general Shockley equations for photovoltaics under illumination, J_{sc} and V_{oc} are directly proportional to the incident light intensity, and the proportional tendency is strongly affected by the charge transport and recombination dynamics within the photovoltaic under operating condition. Therefore, the light intensity dependent measurement of J_{sc} and V_{oc} gives significant information on the recombination dynamics which limits the photovoltaic performance.

(2)-1 Intensity dependence of short circuit current density

The general Shockley equation for photovoltaics under short circuit condition in Equation(1.5), is clearly indicating that the J_{sc} has a linear dependency on the incident light intensity. However, in practical devices, the J_{sc} does not always scale exactly linearly to incident light intensity. Generally, the current density at short circuit shows power-law dependency on the P_{in} as Equation(1.9).²¹

$$J_{ph} = -J_{sc} \propto P_{in}^{\alpha} \quad (1.9)$$

where α ranges from 0.85 to 1 for typical fullerene-based BHJ polymer solar cells. The index $\alpha \equiv 1$ implies that the most of photogenerated charges are extracted prior to recombination, and the deviation of α known to arises from the loss of carriers via bimolecular recombination, a build-up of space charge in the device, variation in the mobility of two carriers, or variations in the distribution of density of states.

(2)-2 Intensity dependence of open circuit voltage

The light intensity dependency of V_{oc} provides the details of the recombination mechanism within the photovoltaic device. Equation(1.6) shows that the V_{oc} has a logarithmically proportional to incident light intensity. Based on the general considerations on quasi-Fermi levels, we can provide an alternative equation for V_{oc} (Equation(1.10)) as derived by Koster et al.^{21,22}

$$V_{oc} = \frac{E_g^{eff}}{q} - \frac{k_B T}{q} \ln \left(\frac{N_c N_v}{np} \right) \quad (1.10)$$

where, E_g^{eff} is the effective band gap, corresponding to the gap between the quasi-Fermi level of hole and electron, n and p are the electron and hole density at open circuit, and N_c, N_v are the density of states in the conduction and valence band.

When the bimolecular recombination (Langevin recombination) is dominant, the recombination rate is given as,

$$R_{bi} = \gamma np = G \quad (1.11)$$

where R_{bi} is a rate of bimolecular recombination per unit volume, γ is the bimolecular recombination constant. Since G is proportional to the incident light intensity I , this results in the following correlation when it substituted into equation(1.10).

$$V_{oc} \propto \frac{k_B T}{q} \ln (I) \quad (1.12)$$

On the other hand, if the SRH recombination (trap-assisted) is dominant, the

recombination rate is given as,

$$R_{SRH} = \frac{C_n C_p N_t}{C_n(n + n_1) + C_p(p + p_1)} np = G \quad (1.13)$$

where, N_t is the trap density, C_n , C_p are the trap coefficients that correspond to the probability of carriers in the corresponding band will be captured when the trap is filled with an opposite charge, n_1 and p_1 are the thermally occupied trap densities. When the traps act as the recombination center, it can be further simplified as follow.

$$np = \frac{4G^2}{C_n C_p N_t^2} \quad (1.14)$$

Therefore, when the SRH recombination is dominant, the correlation between V_{oc} and incident light intensity becomes the following equation.

$$V_{oc} \propto \frac{k_B T}{q} \ln(I^2) = \frac{2k_B T}{q} \ln(I) \quad (1.15)$$

According to the Shockley equation, the slope of the V_{oc} versus $\ln(I)$ plot is corresponding to $\frac{n_1 k_B T}{q}$. Hence, the ideality factor (n_1) of 1 indicates that the bimolecular (Langevin) recombination is dominant, while the n_1 of 2 indicates the SRH (trap-assisted) recombination is dominant at open circuit condition. In general, the n_1 ranges from 1 to 2, suggesting that recombination at open circuit is a combination of SRH and bimolecular process.

1. 3 Functional Materials

1.3.1 Role of Functional Materials in Solar Cells

The functional material plays a significant role in determining the performance of SCs and the device characteristics depend on the location and properties of incorporated functional material.^{4,5,7,23} When the functional material is incorporated at the interface between the electrode and active layer, (i) could eliminate the interfacial charge accumulation by forming Ohmic contact,^{12,24-28} (ii) could reducing the charge recombination by blocking/extracting the carrier selectively,^{7,22,26,29,30} and (iii) reducing the contact resistance by forming better contact at the interface.^{23,28,31} In addition, if the functional material is incorporated at the top interface, the interfacial layer (i) could modulate the light interference within the device as an optical spacer^{30,32-34}, (ii) protect the active layer during thermal evaporation and thermal annealing by preventing the diffusion of aluminum ion,^{35,36} and (iii) isolate the active layer from humidity thus, enhance the stability of device.^{9,29,31,37} On the other hand, if the functional material is incorporated at the bottom interface, it could form better contact at the interface by modulating the adhesion between the active layer and the substrate.^{23,38,39}

Recently, many types of research have been attempted to control the morphology or passivate the trap sites by applying functional materials within the active layer, which is shown to be very effective. Especially, in the field of PSCs, the addition of 3rd component is shown to be efficient to control the morphology, and thus carrier mobility of active layer.⁴⁰⁻⁴⁴ Meanwhile, in the field of PeSCs, by applying functional materials in the middle of perovskite film formation^{29,37,45-47} or even by adding it into the perovskite precursor solution,⁴⁸⁻⁵¹ the film

morphology including crystallinity, surface trap density, and film coverage has successfully modified, furthermore the stability of PeSC has significantly improved.



1.3.2 Mainstream Functional Materials in Research

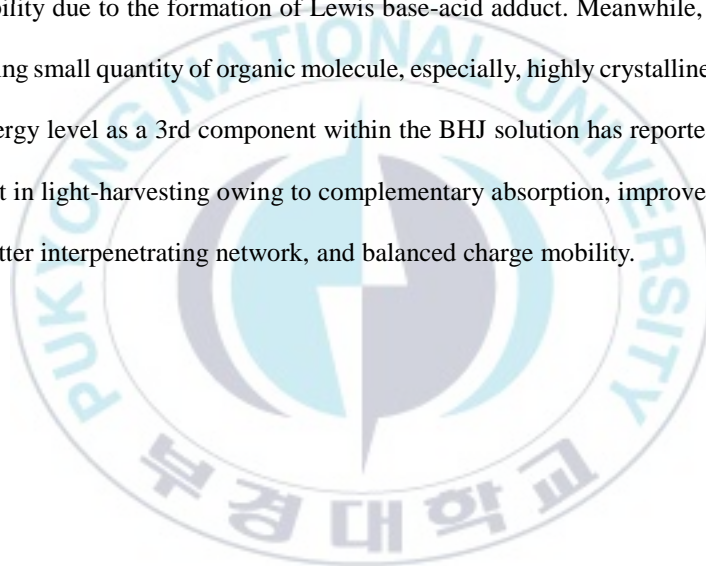
During decades of researches on the field of optoelectronic devices, numerous functional materials have been made, however, a few of them meet the requirement for being applied in solution-processed planar structured solar cells (PSCs). Among the various materials, the organic molecules and metal oxides are mostly used materials owing to their various ideal characteristics that meet the requirement for being incorporated into PSCs.

In order to be incorporated into PSCs as an interfacial layer, the functional material should satisfy several criteria. First, it is mandatory to provide a proper energy level alignment with the corresponding active layer to efficiently block/transfer the charges selectively. Second, it requires to be stable under light, heat, and moisture to ensure the long-term stability of the device. Third, it is required to form a complete layer at low temperature by a solution process for low-cost fabrication, and for further applications such as flexible devices.

Metal oxides with a wide bandgap are advantageous in maximizing the light-harvesting of PSCs, and its adjustable energy level provides better energy level alignment at the charge extraction interface. Furthermore, their superior chemical/thermal stability is advantageous for the long-term stability of the device. Among various metal oxides, TiO_2 , ZnO , SnO_2 are focused owing to ease of process, and superior electrical/optical properties. Especially, sol-gel derived titanium sub-oxide (STO) has been focused as an effective cathode interfacial material because of its low-temperature solution processability and ease of fabrication. It is known that the STO based interfacial layer has many advantages such as enhancement of the charge selectivity by modifying the energy level alignment at the interface, reinforcement of the light intensity within the active layer by redistribution of light intensity, and enhancement

the device stability by protecting active layer and scavenging O_2 / H_2O from the active layer.

Organic molecules, especially conjugated polymers are attracting significant attention as functional materials due to their tunable energy level, and ease of fabrication through a low-temperature solution process. Especially, PEDOT:PSS is the most commonly used material in the field of PSCs. Recently, conjugated polymers, that initially designed as donor materials for OSCs, are adopted on top of perovskite precursor film or even within the precursor solution, results in better film quality with a lower density of defects, better morphology, and better ambient stability due to the formation of Lewis base-acid adduct. Meanwhile, in the field of PSCs, adopting small quantity of organic molecule, especially, highly crystalline polymer with adequate energy level as a 3rd component within the BHJ solution has reported a significant enhancement in light-harvesting owing to complementary absorption, improved morphology including better interpenetrating network, and balanced charge mobility.



Chapter 2 Experimental

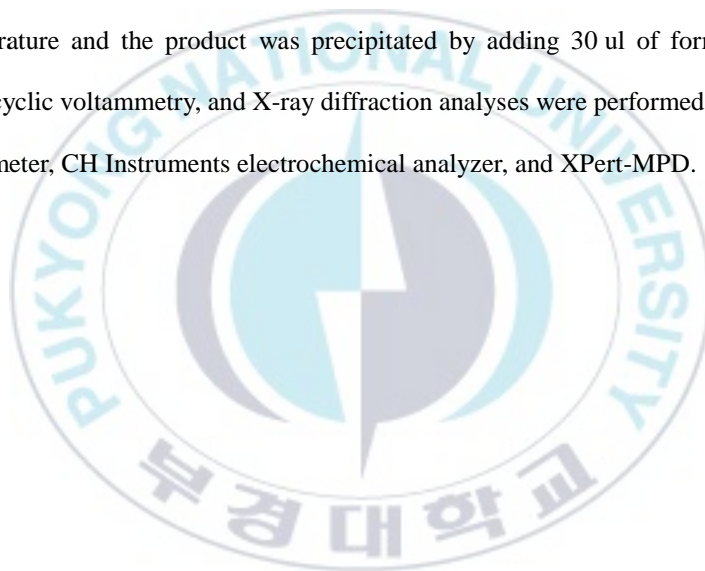
2. 1 Material Preparation

2.1.1 Polymeric Functional Materials

Polymer PCE10 (namely P4 in this work), namely poly([2,6'-4,8-di(5-ethylhexylthienyl)benzo[1,2-b;3,3-b]dithiophene]{3-fluoro-2[(2-ethylhexyl)carbonyl]thieno[3,4-b]thiophenediyl}) was received from Organic Nano Electronic (ONE=1) Materials. Whereas, the monomers 2,6-bis(trimethyltin)-4,8-bis(2-ethylhexyloxy)benzo[1,2-b:4,5-b']dithiophene (BDT) 4,6-bis(5-bromothiophen-2-yl)-2,5-dioctylpyrrolo[3,4-c]pyrrole-1,3(2H,5H)-dione (PPD) and 4,7-bis(5-bromo-4-octylthiophen-2-yl)-5,6-difluorobenzo[c][1,2,5]thiadiazole (DTffBT), were prepared in our group, using the literature. The molecular weights, absorption, cyclic voltammetry and X-ray diffraction analyses were performed on Agilent 1200 Infinity Series separation module, JASCO V-570 spectrometer, CH Instruments electrochemical analyzer, and XPert-MPD.

2.1.2 Metal Oxide based Functional Materials

The sol-gel procedure for producing novel titanium based metal oxide(PTO) is as follows: Titanium(IV) isopropoxide (sigma aldrich, 5 ml), 2-methoxyethanol (sigma Aldrich, 20 ml), and ethanolamine (sigma Aldrich, 2 ml) were injected into dried and nitrogen purged three-neck flask. Injected precursors were stirred and heated at 80 °C for 1 hour. Then, the temperature increased to 120 °C and stirred for 3 hours while carefully purging the nitrogen to condense the precursor. The precursor extracted by adding 10 ml of isopropyl alcohol at room temperature and the product was precipitated by adding 30 ul of formic acid. The absorption, cyclic voltammetry, and X-ray diffraction analyses were performed on JASCO V-570 spectrometer, CH Instruments electrochemical analyzer, and XPert-MPD.



2. 2 Device Preparation

2.2.1 Polymer Solar Cells

The pre-cleaned glass-ITO substrates were dried and PEDOT:PSS (Baytron PH) was spin-cast on glass-ITO substrate. Subsequently, the glass-ITO/PEDOT:PSS substrates were dried at 140 °C for 15 min in an open atmosphere. The resulting substrates were transferred to a glove box for coating the active layers. The respective active layer solution, P1-P3:P4:PC₇₀BM at different ratio in 97:3 (v/v) dichlorobenzene (DCB):1,8-diiodooctane (DIO), was then spin-cast onto the PEDOT:PSS layer. Subsequently, the substrates were dried for 1 h in a glove box. Then, aluminum (Al, 100 nm) electrode was deposited onto the glass-ITO/PEDOT:PSS/active layer substrates by thermal evaporation at approximately 3×10^{-6} Torr. The current density-voltage (J-V) profiles of the OSC devices were acquired using a Keithley 2400 Source Measure Unit. The solar cell performance was determined using an Air Mass 1.5 Global (AM 1.5 G) solar simulator with an irradiation intensity of 1000 Wm^{-2} . The spectral mismatch factor was calculated by comparing the solar-simulator spectrum with the AM 1.5 G spectrum at RT. The incident photon-to-current efficiencies (IPCEs) of the OSCs were measured as functions of wavelength in the 300–1000 nm range using a xenon lamp as the light source, calibrated against a silicon reference cell.

2.2.2 Perovskite Solar Cells

The pre-cleaned glass-ITO substrates were dried and PEDOT:PSS (Baytron PH) was spin-cast on glass-ITO substrate. Subsequently, the glass-ITO/PEDOT:PSS substrates were dried at 140 °C for 15 min in open atmosphere. The resulting substrates were transferred to a glove box for coating the active layers. The respective active layer solution, P1-P3:P4:PC₇₀BM at different ratio in 97:3 (v/v) dichlorobenzene (DCB):1,8-diiodooctane (DIO), was then spin-cast onto the PEDOT:PSS layer. Subsequently, the substrates were dried for 1 h in a glove box. Then, aluminum (Al, 100 nm) electrode was deposited onto the glass-ITO/PEDOT:PSS/active layer substrates by thermal evaporation at approximately 3×10^{-6} Torr. The current density-voltage (J-V) profiles of the OSC devices were acquired using a Keithley 2400 Source Measure Unit. Solar cell performance was determined using an Air Mass 1.5 Global (AM 1.5 G) solar simulator with an irradiation intensity of 1000 Wm^{-2} . The spectral mismatch factor was calculated by comparing the solar-simulator spectrum with the AM 1.5 spectrum at RT. The incident photon-to-current efficiencies (IPCEs) of the OSCs were measured as functions of wavelength in the 300–1000 nm range using a xenon lamp as the light source, calibrated against a silicon reference cell.

Chapter 3 Design and Characterization of Novel Functional Materials

3. 1 Novel Polymeric Functional Materials

3.1.1 Introduction

The OSCs have shown much attention due to their high power conversion efficiency (PCE) via the simple solution processability, mechanical flexibility, lightweight, and roll-to-roll printing technique for the fabrication of large-area devices. It was established well that the blend of electron-donor and electron-acceptor is required to effectively separate the charges generated on the photoactive layer of OSCs⁵²⁻⁵⁸, and the literature reveals that the π -conjugated polymers and fullerene derivatives^{52,53} or π -conjugated organic small molecules^{54,55} are used as an electron-donor and electron-acceptor materials. In conventional OSC devices, single photoactive layer which is composed of bulk heterojunction(BHJ) with one type of donor and acceptor materials is used for light harvesting⁵²⁻⁵⁵ and charge generation, and consequently, the phase-separated and molecular order of BHJ blends became very important for efficient charge separation and transfer since the exciton diffusion length in the organic molecules are quite limited.

To date, various efforts to control the morphology of OSCs have been studied by change the polymer crystallinity, processing conditions such as annealing temperature or processing solvent, and doping with additive. The concept of ternary OSCs with 3rd component was initially presented to efficiently harvest a wider range of solar spectrum while maintaining the

fabrication process to be simple^{59–66}. However, it was shown that the addition suitable of 3rd component not only promotes the light absorption but also efficiently promotes the charge separation and charge transport via improving crystallinity and carrier mobility of BHJ blended active layer. Especially, the inclusion of high aggregation or crystalline materials is found to greatly improve the performance of ternary OSCs. More recently, the properties of 3rd component were fine-tuned via side-chain engineering and studied their effects on ternary OSCs. However, there were no reports on the property modulation of 3rd component via the main-chain engineering effects on the characteristics of ternary OSCs. We think that the photovoltaic performance of binary OSCs might improve via altering the properties, such as absorption, crystallinity, and carrier mobility, of 3rd component via backbone modification.

In this work, we fabricate the novel polymeric functional material, conjugated polymer containing TPT unit. TPT units have been extensively explored in our research group as electron-rich units to prepare π -conjugated polymers for OSCs.^{67–72} TPT derivatives have been polymerized with various π -conjugates, such as indenofluorene (IF)⁶⁷, benzodithiophene (BDT)⁶⁸, phenylene (P), thiophene (T)⁶⁹, benzothiadiazole (BT)⁷⁰, 4,7-bis(2-thienyl)benzothiadiazole (BTBT)⁷¹, and 4,7-bis(2-thienyl)thiadiazoloquinoxaline (TDQ)⁷², with the aim of improving their photovoltaic properties by tuning their photophysical and charge transport properties. Interestingly, the insertion of an electron-withdrawing imide functional group on the 3- and 4-positions of the pyrrole moiety of the TPT unit (imide-functionalized TPT unit » TPTI) results in a deep HOMO⁷³ as well as balanced charge transport⁷⁴ for the polymer:PC₇₀BM blend.

TPTI-based polymers (e.g., P(BDTT-TPTI)) incorporating benzodithiophene (BDTT)

derivatives show high V_{oc} ($\gg 0.9$ V), FF ($\gg 70$ %), and the PCE (~ 7 %) ⁷³, even with their wide band-gap ($E_g \gg 2.0$ eV). In addition, it displayed a good complementary absorption with PCE10. A TPTI-based low band-gap polymer (P(DKPP-TPTI), $E_g \gg 1.37$ eV) incorporating a pyrrolo[3,4-c]pyrrole-1,4(2H,5H)-dione (DKPP) derivative has been recently reported ⁷⁵. Unfortunately, the overall PCE of P(DKPP-TPTI) was found to be poor. The deeper LUMO level ($\gg -3.98$ eV) of P(DKPP-TPTI) may lead to insufficient charge separation at the donor/acceptor interface, which leads to a low J_{sc} . However, P(DKPP-TPTI) shows an impressive V_{oc} ($\gg 0.8$ V) despite its narrow band gap ($\gg 1.37$ eV) ⁷⁵.

We believe that insertion of a relatively strong electron-withdrawing 1-keto-substituent, instead of an imide group, at the 3- and 4-position of the pyrrole moiety in the TPT unit would yield efficient polymers for OSCs. The high efficiency obtained for recently reported polymers with keto-functionalized side chains supports our idea ^{76,77}. Thus encouraged, we prepared a TPT-based new monomer unit (keto-functionalized TPT unit \gg TPTK) incorporating 1-decanone (ketone) at 3, and 4-position of the pyrrole. To obtain TPTK-based polymers with dissimilar band-gaps and energy levels, we polymerized TPTK with distannyl derivatives of three different conjugates, benzodithiophene (BDTT), benzothiadiazole (DTBT), and pyrrolo[3,4-c]pyrrole-1,4-dione (DKPP), to afford three new polymers P(BDTT-TPTK), P(DTBT-TPTK), and P(DKPP-TPTK). Here, we report the preparation, as well as the photophysical, electrochemical, and photovoltaic properties of the TPTK-based polymers. We also briefly compared the properties of the TPTK-based polymers with those of the corresponding TPTI-based polymers, P(BDTT-TPTI), P(DTBT-TPTI), and P(DKPP-TPTI), to understand the effects of keto-substituents replacing the imide group. Note that TPTI-based polymers P(BDTT-TPTI) ⁷³ and P(DKPP-TPTI) ⁷⁵ are already reported, and P(DTBT-TPTI)

has been newly prepared in this study. The chemical structures of the three different 2,5-bis(2-thienyl)pyrrole units (TPT, TPTI, and TPTK), as well as the TPTI- and TPTK-based polymers discussed in this study are shown in Figure 3-1 for ease of understanding.

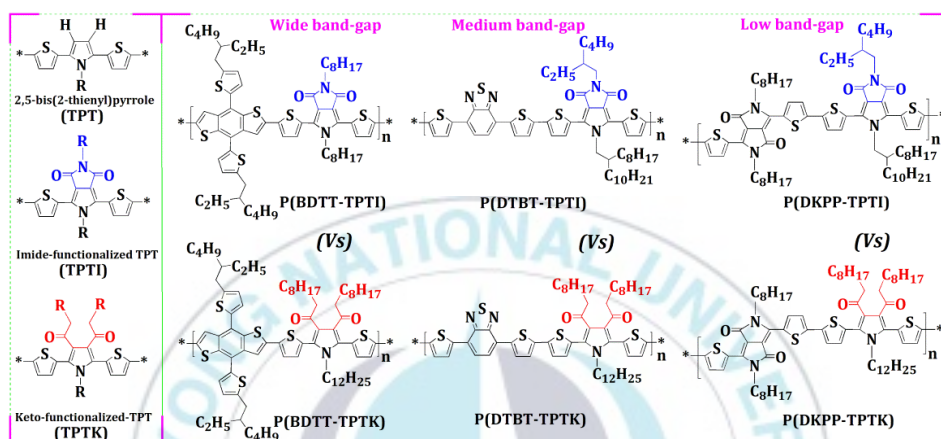


Figure 3-1. Chemical structure of TPT, TPTI, TPTK, and TPTI- and TPTK- based polymers discussed in this study.

3.1.2 Result and Discussion

(1) Optical Properties

Figure 3-2 compares the absorption spectra of the TPTK-based polymers with those of their respective TPTI-based polymers. P(BDTT-TPTK), P(DTBT-TPTK), and P(DKPP-TPTK) showed improved interchain interactions in film than in solution, and consequently, displayed a broad and red-shifted absorption band in the film state as compared to that in solution. As we can see, the absorption spectrum of P(BDTT-TPTK) covers the region from 300 nm to 500 nm, with the absorption onset at 512 nm ($E_g \gg 2.42$ eV), in the film state. However, the absorption spectra of P(DTBT-TPTK) and P(DKPP-TPTK) were extended up to 650 nm and 900 nm, with the absorption onset at 645 nm and 875 nm ($E_g \gg 1.92$ eV and 1.42 eV), respectively, in the film state. The absorption maximum peaks appeared at 404 nm for P(BDTT-TPTK); 383 and 533 for P(DTBT-TPTK); and 368, 603, and 649 for P(DKPP-TPTK) in the thin-film state. The corresponding bands appeared at 514 nm for P(BDTT-TPTI)⁷³; 439 and 562 for P(DTBT-TPTI); and 423, 651, and 700 for P(DKPP-TPTI)⁷⁵.

The absorption bands of the TPTK-based polymers were considerably blue-shifted as compared to those of the corresponding TPTI-based polymers. Notably, the absorption peaks resulting from transition as well as internal charge transfer (ICT) were significantly blue-shifted for all the three TPTK-based polymers. The structures of the TPTI- and TPTK-based polymers were identical except for the substituents attached to the pyrrole backbone. We believe that the difference in the planarity of the TPTI and TPTK units is the main reason for the large difference in the absorption spectra. Consequently, we optimized the structures of TPTI and TPTK using DFT calculations; the results are shown in Figure 3-2 (d). The

calculated twist angles between the thiophene and pyrrole aromatics of TPTI was $\gg 33^\circ$ and it increased to $\gg 50^\circ\text{--}70^\circ$ for TPTK. The decreased planarity of TPTK is expected to suppress electronic transitions as well as interchain interactions. Therefore, the TPTK-based polymers displayed blue-shifted absorption bands compared to those of the TPTI-based polymers.

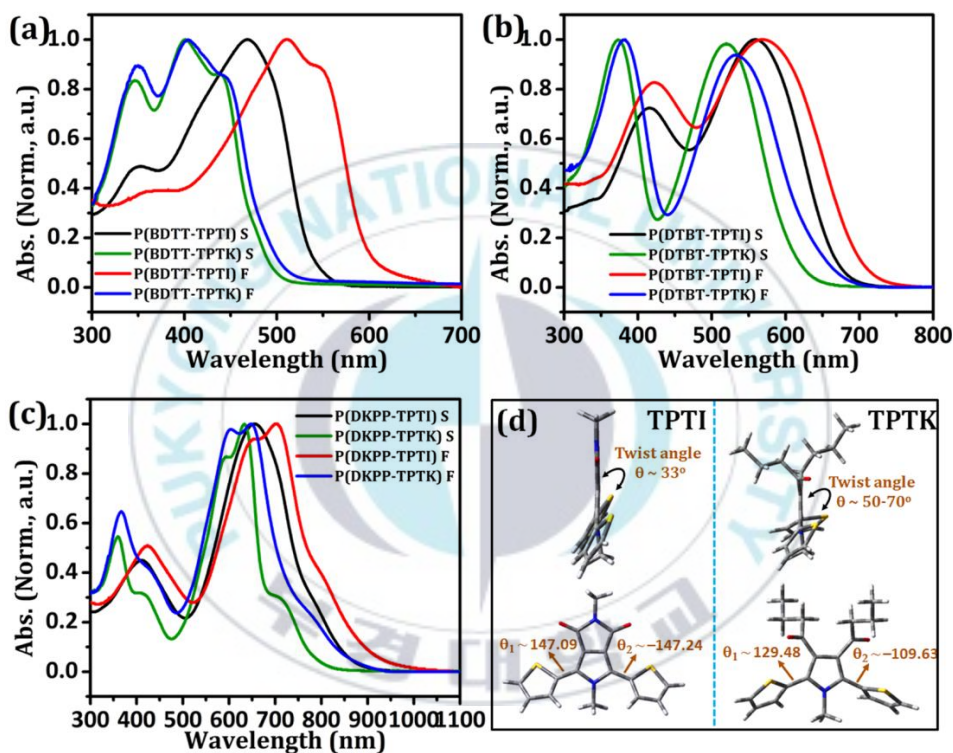


Figure 3-2. Absorption spectra of the polymer P(BDTP-TPTI) and P(BDTP-TPTK) (a), P(DTBT-TPTI) and P(DTBT-TPTK) (b), P(DKPP-TPTI) and P(DKPP-TPTK) (c), and the optimized structures of TPTI and TPTK derivatives (d).

Table 3-1. Properties of TPTI- and TPTK- based polymers.

Polymer	M_w (g/mol) ^c	M_n (g/mol) ^c	PDI ^c	$\lambda_{\max, \text{soln}}$ (nm) ^d	$\lambda_{\max, \text{film}}$ (nm) ^d	E_g (eV) ^d	HOMO (eV) ^e	LUMO (eV) ^e
P(BD TT-TPTI) ^a	3.72 x 10 ⁴	1.85 x 10 ⁴	2.01	471	514	2.04	5.44	3.40
P(BD TT-TPTK)	4.61 x 10 ⁴	1.79 x 10 ⁴	2.58	402	404	2.42	5.58	3.16
P(DTBT-TPTI)	1.67 x 10 ⁴	1.05 x 10 ⁴	1.59	415, 560	439, 562	1.75	5.42	3.67
P(DTBT-TPTK)	2.60 x 10 ⁴	1.82 x 10 ⁴	1.43	373, 520	383, 533	1.92	5.48	3.56
P(DKPP-TPTI) ^b	3.47 x 10 ⁴	1.46 x 10 ⁴	2.37	412, 658	423, 651, 700	1.37	5.35	3.98
P(DKPP-TPTK)	3.26 x 10 ⁴	1.75 x 10 ⁴	1.86	360, 592, 633	368, 603, 649	1.42	5.31	3.89

(2) Electrochemical Properties

Cyclic voltammetry (CV) analysis was performed with P(BDTT-TPTK), P(DTBT-TPTK), P(DKPP-TPTK), and P(DTBT-TPTI) to determine the energy levels of the polymers. The calculated onset oxidation potentials ($E_{ox, onset}$) of P(BDTT-TPTK), P(DTBT-TPTK), P(DKPP-TPTK), P(DTBT-TPTI) and ferrocene from Figure 3-3 were 1.35 V, 1.25 V, 1.08 V, 1.19 V, and 0.57 V, respectively. The standard empirical formulas were used to determine the highest occupied/lowest unoccupied molecular orbital (HOMO/LUMO) energy levels of the polymers. The calculated HOMO/LUMO levels of P(BDTT-TPTK), P(DTBT-TPTK), P(DKPP-TPTK), and P(DTBT-TPTI) were 5.58 eV / 3.16 eV, 5.48 eV / 3.56 eV, 5.31 eV / 3.89 eV, and 5.42 eV / 3.67 eV, respectively. The energy levels of the TPTI- and TPTK-based polymers are summarized in Table 3-1 for comparison. P(BDTT-TPTK) and P(DTBT-TPTK) showed deeper HOMO and higher LUMO levels than those of P(BDTT-TPTI) and P(DTBT-TPTI). However, P(DKPP-TPTK) exhibited slightly higher HOMO and LUMO levels than those of P(DKPP-TPTI).

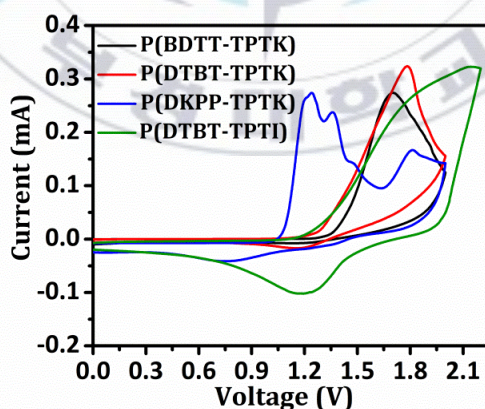


Figure 3-3. CV spectra of P(BDTT-TPTK), P(DTBT-TPTK), P(DKPP-TPTK), and P(DTBT-TPTI)

(3) Photovoltaic Properties

We fabricated OSCs using the newly prepared polymers, P(BDTT-TPTK), P(DTBT-TPTK), P(DKPP-TPTK), and P(DTBT-TPTI) as the donor and PC₇₀BM as the acceptor. The J–V curves of the OSCs fabricated by using P(BDTT-TPTK):PC₇₀BM, P(DTBT-TPTK):PC₇₀BM, P(DKPP-TPTK):PC₇₀BM blends and P(DTBT-TPTI):PC₇₀BM (a, b, c, and d, respectively) under different conditions are presented in Figure 3-4.

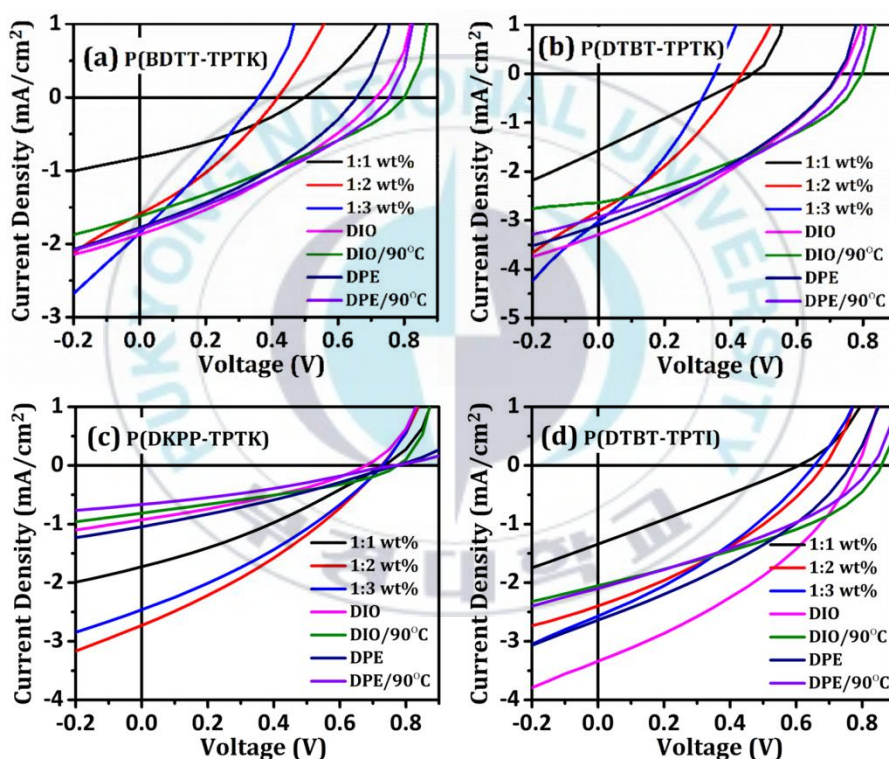


Figure 3-4. J-V characteristics of OSCs fabricated using P(BDTT-TPTK):PC₇₀BM (a), P(DTBT-TPTK):PC₇₀BM (b), P(DKPP-TPTK):PC₇₀BM (c), and P(DTBT-TPTI):PC₇₀BM (d), blends under different conditions such as different polymer:PC₇₀BM ratios (1:1 wt%, 1:2 wt%, and 1:3 wt%)

The maximum PCE achieved for P(BDIT-TPTK), P(DTBT-TPTK), and P(DKPP-TPTK) was 0.43 %, 0.79 %, and 0.63 %, respectively, and the corresponding values for P(BDIT-TPTI), P(DTBT-TPTI), and P(DKPP-TPTI) were 6.57 %, 0.98 %, and 0.91 %. Notably, P(BDIT-TPTK) and P(DTBT-TPTK) showed slightly improved PCE in the case of the devices prepared with additives as compared to that of the devices prepared without any additive. In contrast, P(DKPP-TPTI) showed a decreased PCE for the device processed with additives. A similar trend was observed for TPTI-based polymers. The photocurrent obtained from the J-V measurements were verified with the calculated photocurrent obtained from the incident photon to current efficiency (IPCE) spectra of OSCs. The IPCE spectra are shown in Figure 3-5.

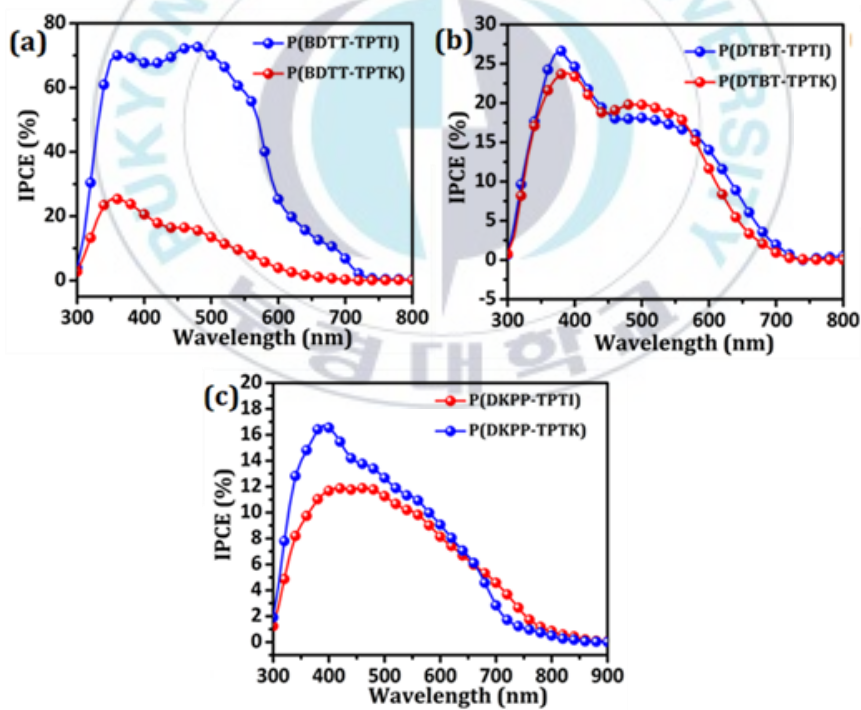


Figure 3-5. IPCE spectra of the OSCs

P(BDTT-TPTK), P(DTBT-TPTK), and P(DKPP-TPTK) showed a lower PCE than that of the corresponding TPTI-based polymers, P(BDTT-TPTI), P(DTBT-TPTI), and P(DKPP-TPTI). Especially, P(BDTT-TPTK) showed much decreased PCE compared to that of P(BDTT-TPTI). On the other hand, the PCEs of P(DTBT-TPTK) and P(DKPP-TPTK) are slightly lower or comparable with those of P(DTBT-TPTI) and P(DKPP-TPTI), respectively. Notably, TPTK-based polymers gave lower V_{oc} than those of their respective TPTI-based polymers though the former polymers showed deeper the HOMO levels than later polymers. In addition, other two photovoltaic parameters such as J_{sc} and FF are also found to be considerably lower for TPTK-based polymers compared to TPTI-based polymers. The decrease in all these photovoltaic parameters such as V_{oc} , J_{sc} , and FF for TPTK-based polymers suggest that the big difference in any one of the parameters such as crystallinity, charge transporting ability, planarity or polymer backbone curvature, and surface morphology could be the reason for the dissimilar performances of TPTK- and TPTI-based polymers. Therefore, we studied all those properties listed above.

(4) Charge Transport Properties

We estimated the hole and electron mobilities of polymer:PC₇₀BM blends using the space-charge-limited current (SCLC) method. The hole- and electron-only devices prepared using P(BD TT-TPTK), P(DTBT-TPTK), P(BD TT-TPTI), and P(DTBT-TPTI) were processed with 3 vol% DIO, while the devices prepared with P(DKPP-TPTK) and P(DKPP-TPTI) were processed without DIO. The J–V curves of the hole- and electron-only devices are shown in Figure 3-6. The estimated hole and electron mobilities are summarized in Table 3-2. The hole mobilities of the TPTK-based polymer:PC₇₀BM blends were in the order of $10^{-5} \text{ cm}^2\text{V}^{-1}\text{s}^{-1}$, and the electron mobilities were one order lower ($10^{-6} \text{ cm}^2\text{V}^{-1}\text{s}^{-1}$) than that of hole mobilities. In contrast, the determined hole and electron mobilities of TPTI-based polymer:PC₇₀BM blends were found to be relatively higher compared to those of their respective TPTK-based polymer:PC₇₀BM blends. Notably, P(BD TT-TPTI) showed balanced carrier mobilities but all other polymers exhibited unbalanced carrier mobilities. The balanced carrier mobilities of P(BD TT-TPTI) could be one of the reasons for their high photovoltaic performance compared to other polymers.

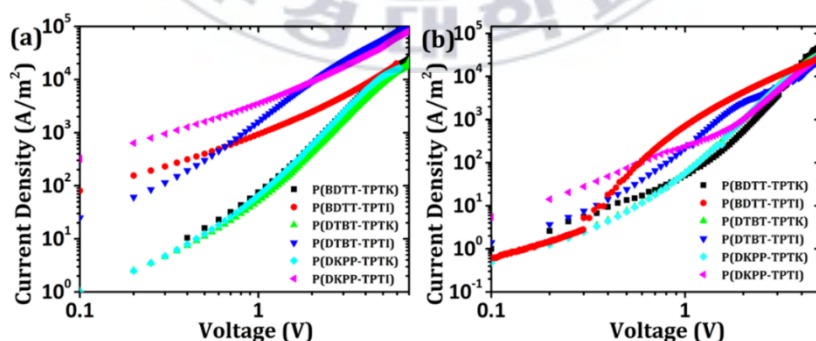


Figure 3-6. J–V curves of hole-only (ITO/PEDOT:PSS/polymer:PC₇₀BM/MoO₃/Al) devices (a), and electron-only (ITO/ZnO/polymer:PC₇₀BM/Al) devices (b).

Table 3-2. Carrier mobilities of TPTK- and TPTI-based polymers

Polymer:PC ₇₀ BM	hole mobility (cm ² V ⁻¹ s ⁻¹) ^a	electron mobility (cm ² V ⁻¹ s ⁻¹) ^b
P(BDTT-TPTK):PC₇₀BM	3.61 × 10 ⁻⁵	3.67 × 10 ⁻⁶
P(BDTT-TPTI):PC ₇₀ BM	3.36 × 10 ⁻⁴	5.76 × 10 ⁻⁴
P(DTBT-TPTK):PC₇₀BM	2.98 × 10 ⁻⁵	1.76 × 10 ⁻⁶
P(DTBT-TPTI):PC ₇₀ BM	7.62 × 10 ⁻⁵	2.58 × 10 ⁻⁶
P(DKPP-TPTK):PC₇₀BM	7.71 × 10 ⁻⁵	4.32 × 10 ⁻⁶
P(DKPP-TPTI):PC ₇₀ BM	3.08 × 10 ⁻⁴	4.89 × 10 ⁻⁵

(5) Crystallinity of the Polymers

Generally, the crystallinity of the polymers play a significant role on the carrier mobilities of the polymer or polymer: PC₇₀BM blends. Therefore, we measured the small angle x-ray diffraction (SAXS) and wide angle x-ray diffraction (XRD) spectra for polymers and polymer:PC₇₀BM films. The respective SAXS and XRD spectra are shown in Figure 3-7.

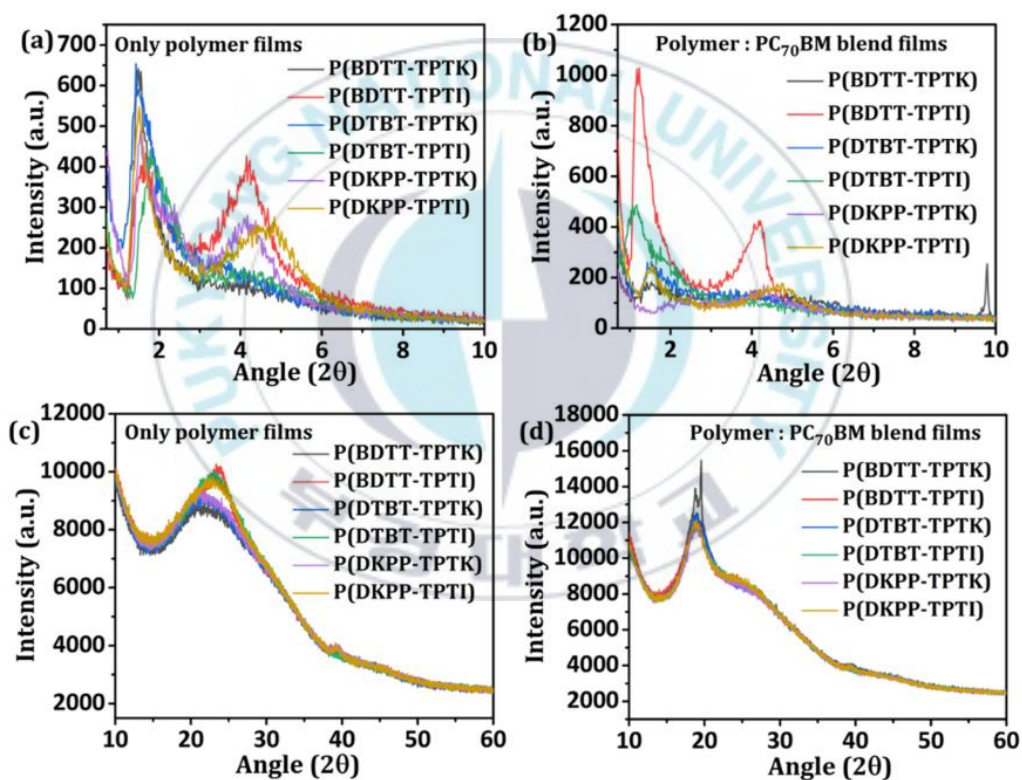


Figure 3-7. (a and b) Small angle X-ray diffraction (SAXS) and (c and d) wide X-ray diffraction (XRD) spectra of polymer and polymer:PC₇₀BM films.

It is very clear that the crystallinity of P(BDTT-TPTI) is superior over all other polymers (See Figure 3-7 (a) and (b)). Therefore, P(BDTT-TPTI) provided the highest mobilities. In addition, the peak at 2θ of $15\text{-}30^\circ$ generally referred for the π - π stacking of polymer chains (see Figure 3-7 (c) and (d)). In this instance, TPTI-based polymers have a relatively higher π - π stacking ability than those of TPTK-based polymers. These results suggest that the planarity and crystallinity of TPTI-based polymers are relatively higher than that of TPTK-based polymers, and consequently, TPTI-based polymers exhibit higher mobilities than TPTK-based polymers.

(6) Curvature of Polymer Backbone

To find the reasons for the much different mobility, crystallinity and photovoltaic performance between P(BDTT-TPTI) and P(BDTT-TPTK), we optimized the structure of the dimer model of the repeating units of P(BDTT-TPTI) and P(BDTT-TPTK).

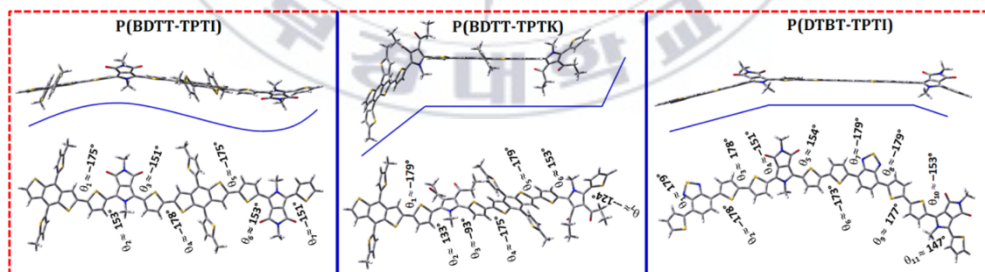


Figure 3-8. Optimized structure of the repeating units of polymers P(BDTT-TPTI), P(BDTT-TPTK), and P(DTBT-TPTI).

As seen in Figure 3-8, P(BDTT-TPTI) shows well controlled wavy structured backbone but P(BDTT-TPTK) exhibits v-shape structured backbone. These results indicate that P(BDTT-TPTI) allows efficient interpenetrating networks formation when it is blended with PC₇₀BM. However, P(BDTT-TPTK) is expected to create charge trap sites due to its hindered structure. It is better to note that the planarity or curvature of the TPT-based polymers is controlled mainly by the twist angles located between the pyrrole and thiophene (refer 2 and 3 on the structures of P(BDTT-TPTI) and P(BDTT-TPTK)) units. All other twist angles are comparable except 2 and 3. Consequently, the similar trend is expected for all TPTK-based polymers. To understand the reason for the poor performances of P(DTBT-TPTI) and P(DKPP-TPTI) compared to P(BDTT-TPTI), we also optimized the structure of P(DTBT-TPTI). Interestingly, P(DTBT-TPTI) shows an arc-like backbone though its planarity is similar to P(BDTT-TPTI). The arc-like structure is also not favorable to get high efficiency. According to the literature⁷⁸⁻⁸⁰, the curvature of the polymer backbone is also crucial to achieving high photovoltaic performance. These results suggest that TPTI is a better candidate than TPTK to develop new materials for optoelectronics. However, careful design such as inserting five or six membered cyclic substituents on the pyrrole backbone of the TPT unit and polymerizing with fused-aromatics (example: benzodithiophene, cyclopentadithiophene, and dithienosilole etc...) is expected to offer efficient polymers for optoelectronic applications.

3.1.3 Summary

Three new alternating polymers, P(BDTP-TPTK), P(DTBT-TPTK), and P(DKKP-TPTK), containing TPTK and BDTP, DTBT, or DKPP were prepared. The calculated E_g s of the polymers were 2.42 eV, 1.92 eV, and 1.42 eV, respectively. The estimated HOMO/LUMO levels of the polymers were -5.58 eV / -3.16 eV, -5.48 eV / -3.56 eV, -5.31 eV / -3.89 eV, and -5.42 eV / -3.67 eV. The determined hole mobilities of the three polymers were on the order of 10^{-5} $\text{cm}^2\text{V}^{-1}\text{s}^{-1}$, and the maximum PCE of the OSCs prepared using P(BDTP-TPTK), P(DTBT-TPTK), and P(DKKP-TPTK) was around 1%. Comparison of the properties of the TPTK-based polymers with those of structurally similar TPTI-based polymers revealed that the substituents attached to the 3- and 4-positions of the pyrrole moiety of TPT unit significantly altering the properties of resulting polymers. In particular, the replacement of the cyclic imide functional group with the acyclic keto functional group led to a higher band-gap and lowers the charge transport properties of the resulting polymers. Consequently, the TPTK-based polymers provided lower PCEs than did the TPTI-based polymers. This study indicates that the incorporation of appropriate substituents, such as strongly electron-accepting cyclic substituents, on the TPT backbone may provide efficient materials for optoelectronics.

3.2 Incorporation of Novel Polymeric Functional Material in Organic BHJ Solar Cell

3.2.1 Introduction

It has been well established that a blend of electron-donor and electron-acceptor is required to effectively separate the charges generated on the photoactive layer of PSCs,⁵²⁻⁵⁸ and the literature reveals that π -conjugated polymers and fullerene-derivatives,^{52,53} or π -conjugated organic small molecules^{54,55} are used as electron-donor and electron-acceptor materials. In conventional PSC devices, a single photoactive layer that contains only one type of donor and acceptor material is used for light-harvesting,⁵²⁻⁵⁵ and consequently, it is difficult to harvest light effectively across the full (UV-visible to near infra-red) solar spectrum. Maximizing the light absorption of the PSC device as much as possible is essential to obtaining a high short-circuit current (J_{sc}), and thereby good *PCE*.

Therefore, researchers have introduced the concept of tandem PSCs (tan-PSCs): two or more photoactive layers, each containing different donor and/or acceptor materials with dissimilar absorption bands, are connected serially or in parallel to improve the photovoltaic performances of the PSCs.⁸¹⁻⁸⁹ It is worth noticing that the fabrication of tan-PSCs is more challenging than that of conventional PSCs. The idea of ternary PSCs (ter-PSCs) is presented, because the fabrication process is similar to that of conventional PSCs, and the photovoltaic performance can be maximized.⁵⁹⁻⁶⁶ On ter-PSCs, a single photoactive layer is used, but three or more appropriate electron-donor and/or -acceptor materials having different absorption bands are employed for

light absorption and charge separation. Consequently, the resulting ter-PSCs exhibited improved photovoltaic performances compared with bi-PSCs.^{59–66}

The reports on binary PSCs have suggested that the electron-donating polymer P4 (PTB7-Th) obtained a higher *PCE* when it was blended with electron-accepting PC₇₀BM via the good complementary absorption between P4 (intense absorption range: 550–770 nm) and PC₇₀BM (intense absorption range: 300–450 nm).^{90–94} The photovoltaic performance of the P4:PC₇₀BM blend was greatly improved further via the inclusion of a suitable co-absorbent, a π -conjugated polymer or organic small molecule, which improved the absorption, crystallinity, and carrier mobility of P4:PC₇₀BM blends.^{95–111} Consequently, the ter-PSCs fabricated using a P4:co-absorbent:PC₇₀BM blend exhibited a higher *PCE* than the P4:PC₇₀BM blend.^{95–111} In particular, the inclusion of highly aggregated or crystalline materials was found to greatly improve the performances of ter-PSCs.^{41–43,109,110} More recently, the properties of co-absorbing polymers were fine-tuned via side-chain engineering, and their effects on ter-PSCs were studied.¹¹² However, there have been no reports on the performances of ter-PSCs using property modulation of co-absorbing wide band-gap polymers with main-chain engineering. We expect that the photovoltaic performance of the P4:PC₇₀BM blend might also improve by altering the properties, such as absorption, crystallinity, and carrier mobilities, of the co-absorbing wide band-gap polymers via backbone modification. One of the polymers that we reported, PBDTTPPD, containing benzodithiophene (BDT) and di(thiophene)pyrrolo[3,4-c]pyrrole-1,3-dione (PPD) derivatives displayed a wide band-gap (intense absorption range: 300–600 nm) and good complementary absorption with P4.⁷³ However, the polymer PBDTDTffBT, which incorporates BDT and di(thiophene)-5,6-difluorobenzo[c][1,2,5]thiadiazole (DTffBT) derivatives, showed high crystallinity but an

absorption region (intense absorption range: 500–750 nm) quite similar to that of P4.¹¹³ The structures of PBDTPPD and PBDTDTffBT are shown in Figure 3-9. The polymer PBDTPPD might be a better candidate than PBDTDTffBT for use as a co-absorbent with the P4:PC₇₀BM blend. However, the inclusion of DTffBT on the PBDTPPD backbone is expected to induce red-shift absorption and increase the crystallinity of the resulting polymers, which should be helpful in improving the *PCE* of the P4:PC₇₀BM blend. Therefore, a series of polymers, **P1–P3**, containing different ratios of BDT:PPD:DTffBT were prepared, and their photovoltaic properties were studied in binary and ternary PSCs.

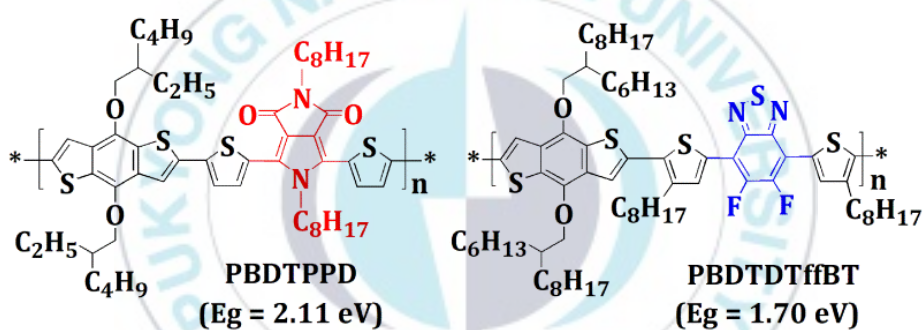


Figure 3-9. Chemical structures of PBDTPPD and PBDTDTffBT

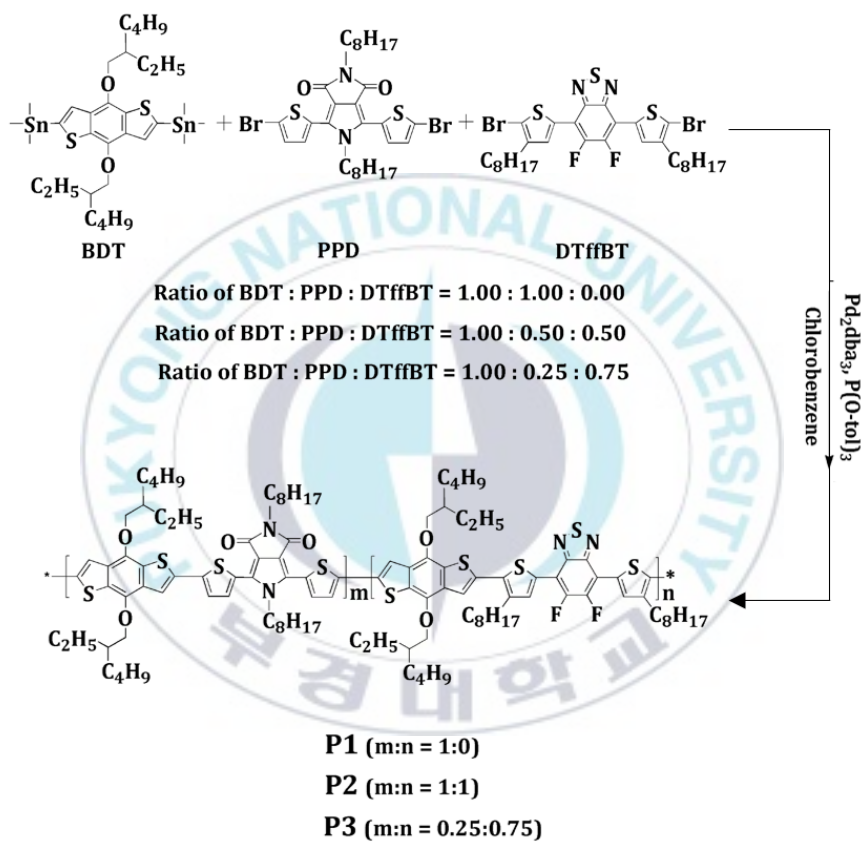


Figure 3-10. Synthetic route to P1-P3.

3.2.2 Result and Discussion

The conventional Stille polymerization of respective monomers as shown in Figure 3-10 afforded polymers P1-P3. Polymers P1 and P2 exhibited good solubility, in chloroform (CF), chlorobenzene (CB), and dichlorobenzene (DCB) with a concentration of 10 mg/ml, but P3 showed moderate solubility in all three solvents at ambient temperature.

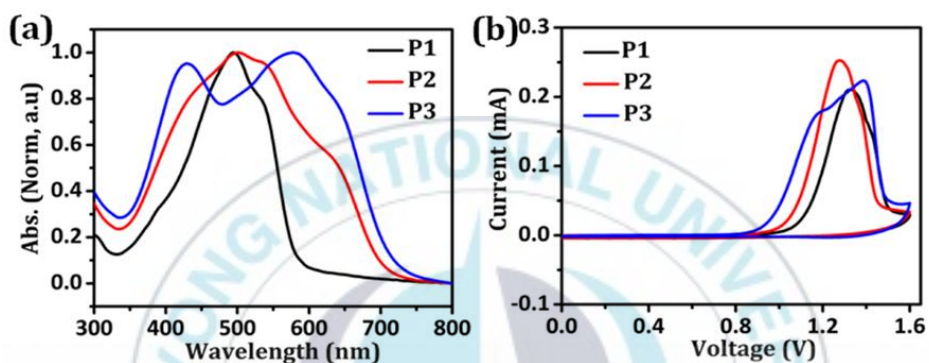


Figure 3-11. Film state absorption spectra (a), cyclic voltammogram (b) for P1-P3.

The absorption spectra (UV), cyclic voltammograms (CV) for P1-P3 are shown in Figure 3-11. The absence of DTffBT unit on the polymer backbone results narrow absorption band with higher E_g (P1 ~ 2.11 eV) compared to the polymers containing DTffBT unit on their backbone (P2: E_g ~ 1.74 eV and P3: E_g ~ 1.71 eV). The absorption of P1 results only from π - π^* electronic transitions, whereas those originating from the companied electronic transitions such as π - π^* and internal charge transfer between BDT and DTffBT units for P2 and P3. It is well known that the benzothiadiazole unit promotes the efficient internal charge transfer between adjacent aryl π -conjugates and benzothiadiazole.^{71,114-117} Therefore, the insertion of DTffBT unit on P1 backbone significantly lowering the band-gaps and also

broadening the absorption bands for the resulting polymers P2 and P3. The cyclic voltammetry analysis indicates that the HOMO levels of the polymers were gradually increased from -5.38 to -5.26 eV when the amount of DTffBT unit increased on the backbone of the polymer. The determined molecular weights, absorption maxima, optical band-gaps, and energy levels of P1-P3 are presented in Table 3-3.

Table 3-3. Molecular weight, photo-physical, and electrochemical properties of P1-P3.

Polymer	M_n (g/mol) ^a	M_w (g/mol) ^a	PDI ^a	$\lambda_{\max, \text{film}}$ (nm) ^b	E_g (eV) ^b	HOMO (eV) ^c	LUMO (eV) ^c
P1	1.98×10^4	4.40×10^4	2.22	494	2.11	-5.38	-3.27
P2	1.54×10^4	3.83×10^4	2.49	501	1.74	-5.32	-3.58
P3	1.51×10^4	4.12×10^4	2.73	430,578	1.71	-5.26	-3.55

The small-angle X-ray scattering (SAXS), and X-ray diffraction (XRD) spectra for P1-P3 are shown in Figure 3-12.

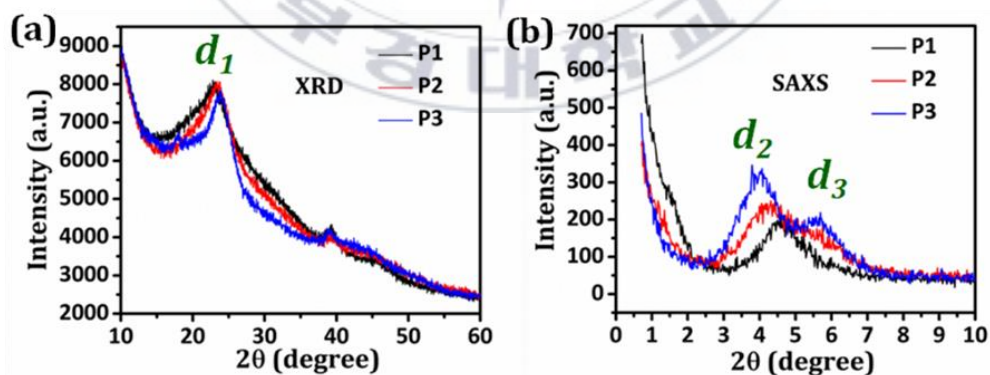


Figure 3-12. Film state XRD (a), and SAXS spectra (b) for P1-P3.

The XRD and SAXS spectra of the polymers P1-P3 indicates that their crystallinity is greatly alerted via the incorporation of different ratio of DTffBT unit on polymer backbone. The peaks correspond to π - π stacking ($2\theta \sim 23.00, 23.40, \text{ and } 23.72^\circ$, respectively for P1, P2, and P3) between the polymer chains clearly indicates that the crystallinity of the polymers is increased in the order of $P1 < P2 < P3$, and the calculated π - π stacking spacing (d_1) between the polymer chains were 3.86, 3.80, and 3.75 Å, respectively.¹¹⁸ The inclusion of higher amount of DTffBT unit on polymer backbone notably increased the crystallinity of the resulting polymer, and the relatively narrow peak appeared at 2θ of $23\text{-}24^\circ$ and shorter π - π stacking spacing confirmed our argument. On the other hand, the peaks correlated to inter-chain spacing ($2\theta \sim 2\text{-}7^\circ$) of the polymer chains are also significantly altered via the incorporation of DTffBT unit on polymer backbone.¹¹⁸ Polymer P1 displayed single inter-chain spacing ($2\theta \sim 4.58^\circ$) of 19.28 Å. In contrast, polymers P2 and P3 showed two different inter-chain spacing (d_2 and d_3 at $2\theta \sim 4.27, 5.69^\circ$ and $4.03, 5.69^\circ$) of 20.68, 15.52 Å, and 21.91, 15.52 Å, respectively. Overall, polymers P2 and P3 showed additional shorter inter-chain spacing of 15.52 Å compared to P1. The XRD analysis confirmed that crystallinity of P3 is superior over P2 and P1.

The bi-PSCs were fabricated using P1-P3 as an electron-donor and PC₇₀BM as an electron-acceptor with a configuration of ITO/PEDOT:PSS/1:1.5 (w/w) Polymer:PC₇₀BM + 3 vol% DIO/Al. The PSCs offered a maximum PCE of 5.41 % ($V_{oc} \sim 0.88$ V, $J_{sc} \sim 9.04$ mA/cm², and FF ~ 0.68), 5.55 % ($V_{oc} \sim 0.84$ V, $J_{sc} \sim 10.80$ mA/cm², and FF ~ 0.61), and 4.01 % ($V_{oc} \sim 0.74$ V, $J_{sc} \sim 10.42$ mA/cm², and FF ~ 0.52), respectively, for P1, P2, and P3. Polymers P2 exhibited higher J_{sc} but lower V_{oc} compared to P1 due to their extended absorption and higher HOMO levels. However, P3 expected to provide higher J_{sc} and PCE than those of P2 but it

offered comparable J_{sc} and PCE with P2. It is worth to note that the good solubility of the polymer is essential for solution processability, and which assists the formation of uniform photoactive layer film and also efficient interpenetrating networks between polymer and PC₇₀BM. As we mentioned above, the solubility of P3 is moderate in CB and DCB. Therefore, the P3:PC₇₀BM blend solution in DCB blend is not possible to filter (we need to add the filter details, 0.4 μm) even after stirred at 80 °C for 3 h. However, we successfully fabricated the PSC device without filtering the P3:PC₇₀BM blend solution. Impressively, the resulting PSC device made by using P3 also exhibited comparable PCE but lower J_{sc} than expected value. The lower V_{oc} is reasonable but the J_{sc} and FF are expected to improve by improving the

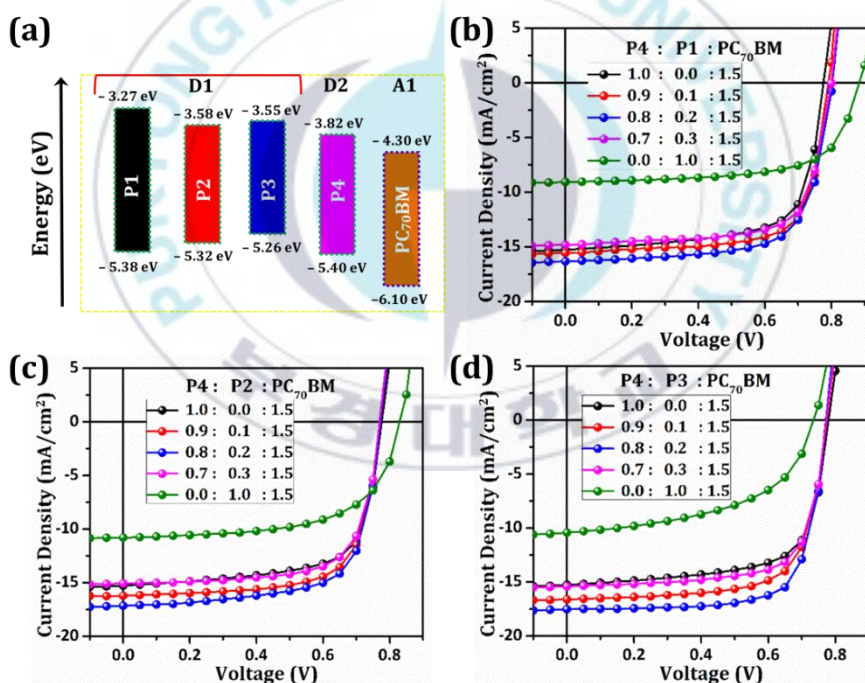


Figure 3-13. (a) Energy levels of donor and acceptor materials. (b-d) The J-V curves of the PSCs made by using different ratios of P4:P1-P3:PC₇₀BM + 3 vol% DIO blends.

solubility of P3. We would like to insist that our motive is not to develop efficient polymers for bi-PSCs, and to study the possibility of enhancing the performance of ter-PSCs via the property modulation co-absorbing wide band-gap polymers. Consequently, ter-PSCs were fabricated using P4:P1-P3:PC₇₀BM + 3 vol% DIO blends at different ratio. For the better understanding, the energy levels (c), and the J-V curves of the bi- and ter-PSC devices (d-f) are shown in Figure 3-13. The bi-PSC device fabricated from 1:1.5 (w/w) P4:PC₇₀BM + 3 vol% DIO blend offered a maximum PCE of 8.20 % with a V_{oc} of 0.79 V, J_{sc} of 15.27 mA/cm², and FF of 0.68. On the other hand, the ter-PSC devices prepared using 0.8:0.2:1.5 (w/w/w) P4:P1-P3:PC₇₀BM + 3 vol% DIO blends provided an improved PCE of 9.31 % (V_{oc} ~ 0.80 V, J_{sc} ~ 16.29 mA/cm², and FF ~ 0.71), 9.60 % (V_{oc} ~ 0.79 V, J_{sc} ~ 17.12 mA/cm², and FF ~ 0.71), and 9.85 % (V_{oc} ~ 0.78 V, J_{sc} ~ 17.54 mA/cm², and FF ~ 0.72). The photovoltaic parameters of the PSC devices made with different ratio of P4:P1-P3:PC₇₀BM + 3 vol% DIO blends are summarized in Table 3-4. The improved performances of ter-PSCs compared to that of P4 mainly attributed from their enhanced J_{sc}. In order to verify the J_{sc}, we measured the absorption spectra of P1-P4, and the IPCE spectra of bi- and ter-PSCs and those are presented in Figure 3-14. The calculated J_{sc} from the IPCE spectra were 8.59, 10.38, 10.55, 15.33, 15.97, 16.82, and 17.32 mA/cm² for the PSCs made with P1:PC₇₀BM, P2:PC₇₀BM, P3:PC₇₀BM, P4:PC₇₀BM, P4:P1:PC₇₀BM, P4:P2:PC₇₀BM, and P4:P3:PC₇₀BM blends, respectively. These values are found to be similar to the J_{sc} values, 9.04, 10.80, 10.42, 15.27, 16.29, 17.12, and 17.54 mA/cm², obtain from the J-V curves of PSCs. Impressively, the IPCE responses of ter-PSCs were found to be increased in the hole region of the spectra compared to that of bi-PSCs made with P4:PC₇₀BM blend. On the other hand, we also noted a slight variation on the V_{oc} of ter-PSCs compared to that of the bi-PSCs made with P4:PC₇₀BM blend, and which is

expected to originate from the differences in the energy levels of P1-P3. Notably, the FFs of the ter-PSCs are increased gradually while the inclusion of P1-P3 on P4:PC₇₀BM blend. According to the reports, all the photovoltaic parameters were increased when the highly crystalline organic small molecule or π -conjugated polymer included on P4:PC₇₀BM blend.⁴ 1-43,109,110 As seen in Figure 4-11, the crystallinity of the polymers is increased in the order of P1 < P2 < P3, and consequently, the enhanced photovoltaic parameters of the ter-PSCs are expected to recognize from the good complementary absorption and improved charge extraction via the suppressed charge recombination.

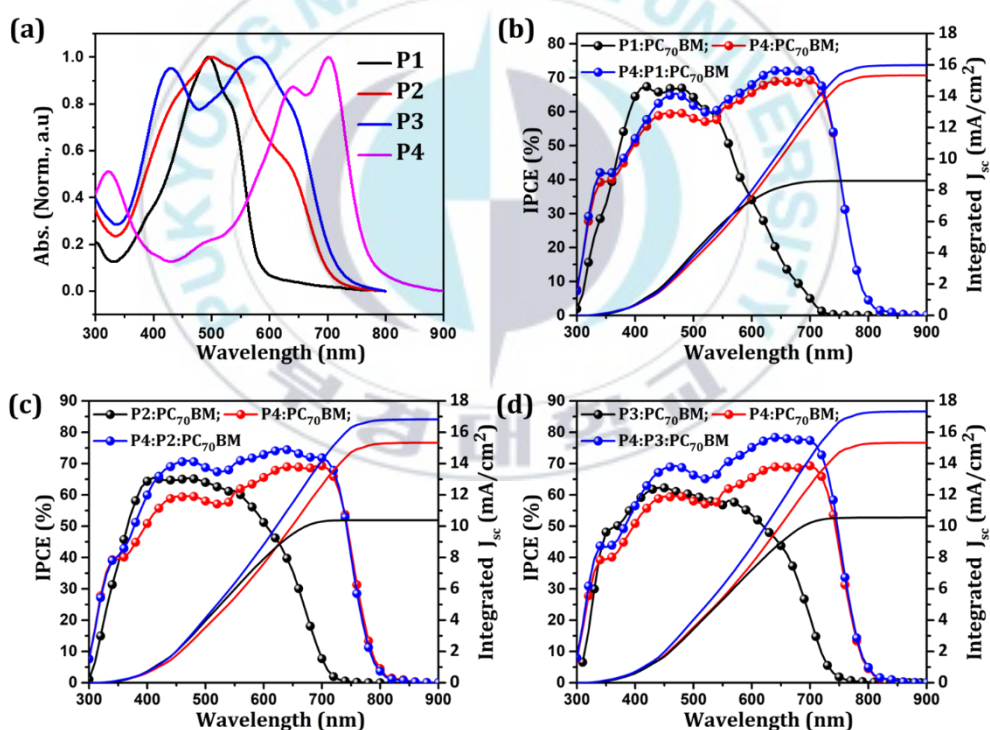


Figure 3-14. (a) Absorption spectra of P1-P4, (b) IPCE spectra of the bi- and ter-PSCs made by using different ratios of P4:P1-P3:PC₇₀BM + 3 vol% DIO blends.

Table 3-4. Photovoltaic parameters of the OSC devices made by using X:X:X (w/w/w) P4:P1-P3:PC₇₀BM + 3 vol% DIO blends.

Active layer	x:x:x wt%	J_{sc} (mA/cm ²) ^a	V_{oc} (V) ^b	FF (%) ^c	PCE (%) ^d
PTB7- Th:AP1:PC ₇₀ BM	1.0:0.0:1.5	15.27	0.79	68	8.20
	0.9:0.1:1.5	15.56	0.79	70	8.67
	0.8:0.2:1.5	16.29	0.80	71	9.31
	0.7:0.3:1.5	14.86	0.80	69	8.20
	0.0:1.0:1.5	9.04	0.88	68	5.41
PTB7- Th:RP1:PC ₇₀ BM	1.0:0.0:1.5	15.27	0.79	68	8.20
	0.9:0.1:1.5	16.16	0.79	70	9.02
	0.8:0.2:1.5	17.12	0.79	71	9.60
	0.7:0.3:1.5	15.07	0.78	70	8.22
	0.0:1.0:1.5	10.80	0.84	61	5.55
PTB7- Th:RP2:PC ₇₀ BM	1.0:0.0:1.5	15.27	0.79	68	8.20
	0.9:0.1:1.5	16.70	0.78	71	9.24
	0.8:0.2:1.5	17.54	0.78	72	9.85
	0.7:0.3:1.5	15.42	0.78	71	8.54
	0.0:1.0:1.5	10.42	0.74	52	4.01

To verify the charge extraction and suppressed charge recombination, we determined the hole (μ_h) and electron (μ_e) mobilities of x:x:x (w/w/w) P4:P1-P3:PC₇₀BM + 3 vol% DIO blends by using space-charge limited current (SCLC) method. We fabricated the hole-only (ITO/PEDOT/active layer/MoO₃/Ag) and electron-only (ITO/ZnO/active layer/Al) devices with an active layer of x:x:x (w/w/w) P4:P1-P3:PC₇₀BM + 3 vol% DIO blends. The $J-V$ curves of the hole-only and electron-only devices are shown in Figure 3-15 and the mobilities were calculated using space-charge limited current (SCLC) method. The P1-P4:PC₇₀BM blends exhibited the hole and electron mobilities (μ_h and μ_e) of 6.12×10^{-5} , 6.69×10^{-5} , 1.91×10^{-4} , $8.62 \times 10^{-4} \text{ cm}^{-2}\text{V}^{-1}\text{s}^{-1}$, and 5.02×10^{-4} , 2.01×10^{-4} , 8.10×10^{-4} , $4.05 \times 10^{-4} \text{ cm}^{-2}\text{V}^{-1}\text{s}^{-1}$,

respectively. Whereas, the P4:**P1-P3**:PC₇₀BM blends showed the μ_h and μ_e of 8.26×10^{-4} , 7.35×10^{-4} , $7.95 \times 10^{-3} \text{ cm}^{-2}\text{V}^{-1}\text{s}^{-1}$, and 6.29×10^{-4} , 6.05×10^{-4} , $8.32 \times 10^{-4} \text{ cm}^{-2}\text{V}^{-1}\text{s}^{-1}$, respectively. Notably, P4:PC₇₀BM blend displayed μ_h/μ_e ratio of 2.12, but the inclusion of 20 wt% of each of **P1**, **P2**, and **P3** on P4:PC₇₀BM blends significantly lowers the μ_h/μ_e ratios to 1.31, 1.21, and 0.96. The μ_h/μ_e ratio value closer to 1 is expected to show very good charge transport between active layer and electrodes. Therefore, the PSCs made by using P4:**P3**:PC₇₀BM blend shown better or improved photovoltaic performance than that of the devices prepared using P4:**P1**:PC₇₀BM, P4:**P2**:PC₇₀BM, and P4:PC₇₀BM blends.

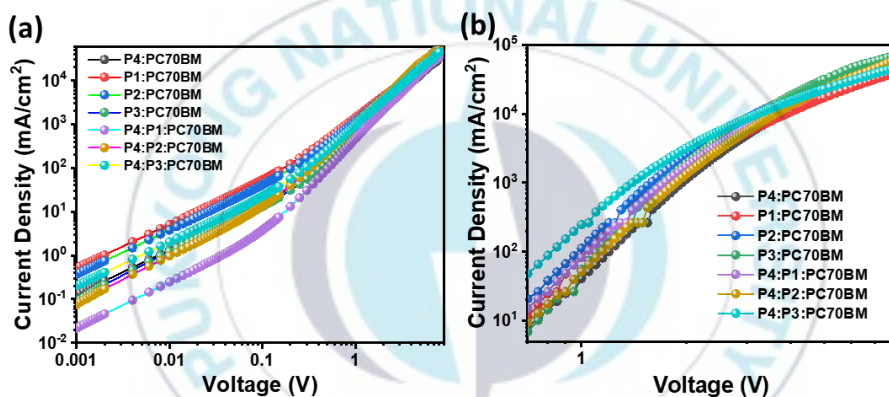


Figure 3-15. J-V curves for hole-only (a) and electron-only (b) devices.

We thought that the difference in the crystallinity or morphological modification of ternary blends such as P4:P1:PC₇₀BM, P4:P2:PC₇₀BM, and P4:P3:PC₇₀BM compared with binary blends, namely P4:PC₇₀BM, could be the main reason for the difference in their mobilities. Therefore, we performed thin film XRD and SAXS analysis for the P4:PC₇₀BM, P4:P1:PC₇₀BM, P4:P2:PC₇₀BM, and P4:P3:PC₇₀BM films, and the respective images are shown in Figure 3-16. The SAXS spectra of the P4:PC₇₀BM and the ternary blends are quite similar. However, the intensity ratio between each peaks corresponding to π - π stacking

(d_2/d_1 , where d_1 and d_2 at 2θ of 18.9° and 22.5°) are higher for the ternary blends, indicating that closer π - π stacking exists between polymers of ternary blends compared to that of the P4:PC₇₀BM blend. Overall, a slight modification occurred in the crystallinity of the photoactive layer of the ternary blends compared with the P4:PC₇₀BM blend.

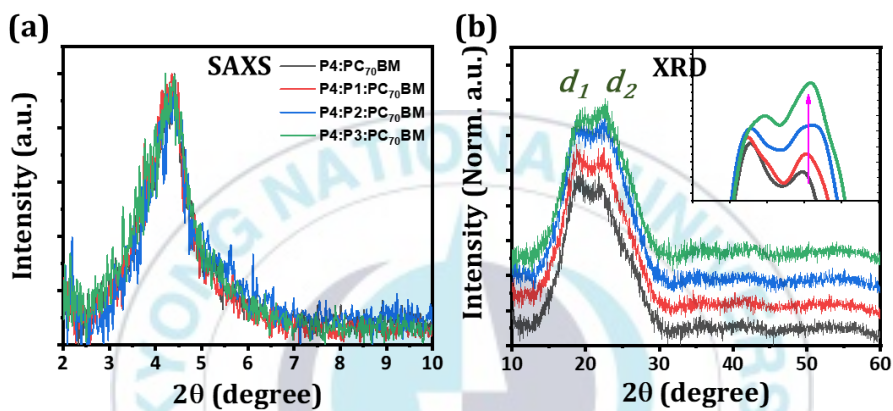


Figure 3-16. SAXS and XRD (a and b) spectra for the active layer films. (inset : smoothed XRD spectra)

The morphologies of the films prepared using P4:PC70BM, P4:P1:PC70BM, P4:P2:PC70BM, and P4:P3:PC70BM blends were studied using TEM, and the respective TEM images are shown in Figure 3-17. All four films showed good surface morphologies. However, the ternary blends, such as P4:P1:PC70BM, P4:P2:PC70BM, and P4:P3:PC70BM, showed relatively improved interpenetrating networks between the polymers and PC70BM compared to binary blend namely P4:PC70BM. Overall, the crystallinity and morphology of P4:PC70BM blend notably altered via the inclusion of co-adsorbing polymers P1-P3, and which leads to higher photovoltaic performances.

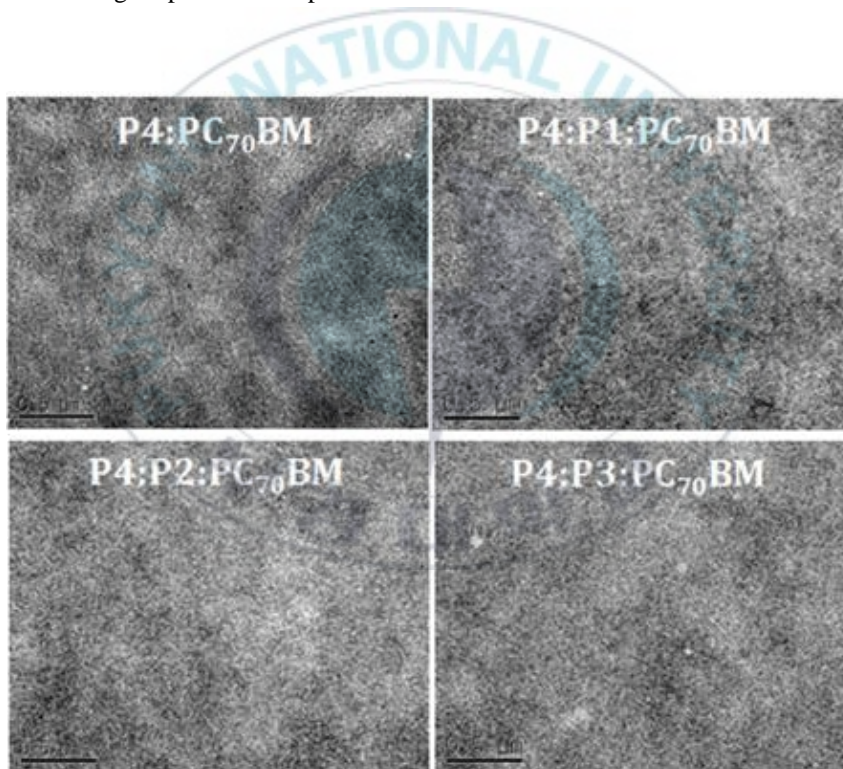


Figure 3-17. TEM images for the active layer films.

3.2.3 Conclusion

A series of polymers, P1-P3, containing different ratios of benzodithiophene, pyrrolo[3,4-c]pyrrole-1,3-dione, and difluoro-benzothiadiazole derivatives were prepared with the aim of enhancing the photovoltaic performance of ter-PSCs. The estimated E_gs and HOMO levels of P1-P3 were 2.11, 1.74, and 1.71 eV, and -5.38, -5.32, and -5.26 eV, respectively. The XRD analysis revealed that the crystallinity of the polymers is increased in the order of P1 < P2 < P3. Overall, the incorporation of difluoro-benzothiadiazole derivatives on polymer backbone notably altered their photophysical, electrochemical and crystallinity. However, all three polymers displayed comparable photovoltaic performance for the bi-PSCs made by using P1-P3:PC₇₀BM blends and the maximum PCEs obtained were 5.41 %, 5.55 %, and 4.01 %, respectively. Surprisingly, the inclusion of 20 wt% of P1-P3 on P4:PC₇₀BM blends found to be notably improved the photovoltaic performance resulting ter-PSCs. The maximum PCEs achieved for the ter-PSCs made by using P4:P1-P3:PC₇₀BM blends were 9.31 %, 9.60 %, and 9.85 %, respectively, and which is 10 %, 15 %, and 20 % higher than that of the bi-PSCs made by using P4:PC₇₀BM blend. Overall, the property modulation of co-absorbing polymers results greatly enhanced photovoltaic performances for ter-PSCs via the improved absorption, crystallinity, and charge extraction with suppressed charge recombination. We think this study is very much helpful to the researchers working on PSCs.

Chapter 4 Study on the Novel Metal Oxide based Functional Materials

4. 1 Preparation and Characterization of Novel Metal Oxide based Functional Materials

4.1.1 Introduction

Highly efficient organic solar cells (OSCs) are attracting continuous attention as the promising technology for commercialization due to its potential in large scale processability and a wide range of applications. The field of OSCs has progressed during the last decades in terms of device performance, lifetime and range of applications that have been accompanied by the development of interfacial materials.^{4,7,29} Consequently, tremendous efforts have been devoted to developing interfacial materials, among various candidates, metal oxides (MOs) have most extensively studied due to its superior properties for high performing PSCs such as high transparency, thermal/chemical stability, electrical homogeneity.^{23,29,119} Especially, sol-gel derived titanium sub-oxide (STO) has been focused as an effective cathode interfacial material because of its solution processability and ease of fabrication. It is known that the STO based interfacial layer has many advantages such as enhancement of the charge selectivity by modifying the energy level alignment at the interface^{26,120}, reinforcement of the light intensity within the active layer by redistribution of light intensity³²⁻³⁴, and enhancement the device stability by protecting active layer and scavenging O₂ / H₂O from the active layer.^{9,32,121}

4.1.2 Result and Discussion

(1) Shelf stability of novel solid-state titanium sub-oxide

The major concern on the commercialization of STO arises from its short shelf-life time due to severe hydrolysis in ambient air. As described in Figure 4-1, the aim of this work is to suppress the hydrolysis reaction by separate them from the hygroscopic solvent and reducing the surface area through solidification of STO while letting the major benefits of STO to be maintained. We used many different anions for salt formations, among them, the HCOO⁻ (formate ion) was found to undergo effective salt formation reaction with STO and provided white and smooth precipitates instantly.

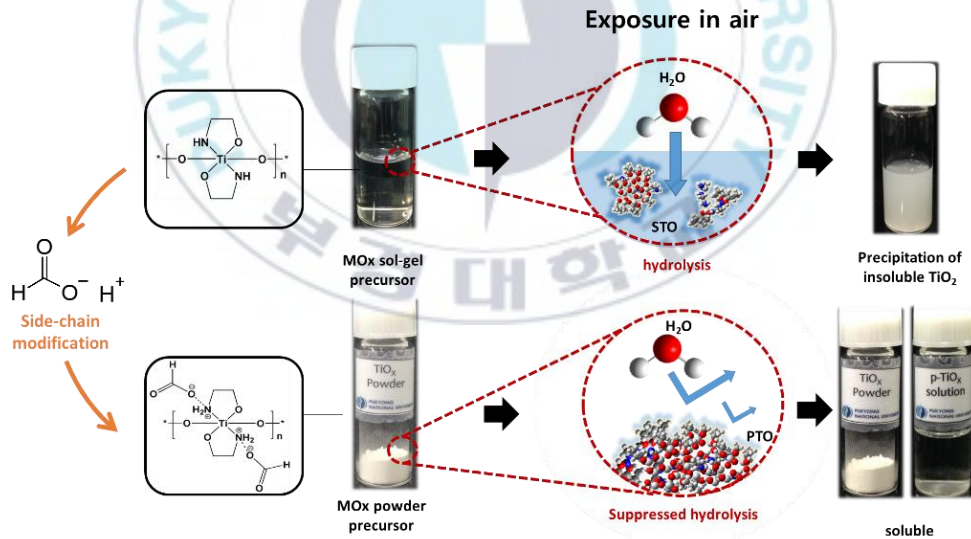


Figure 4-1. Conceptual figure of this work: a comparison between solid-state metal oxide precursor and conventional sol-gel derived metal oxide precursor.

The appearance, solubility in different solvents and stability results for PTO are shown in Figure 4-2. Notably, newly prepared PTO shows negligible changes in color and solubility upon 10 days of storage in ambient condition. As it could be seen from the UV-Vis spectra of STO precursor solution, after 10 days of exposure, STO became opaque while the PTO maintained to be the same.

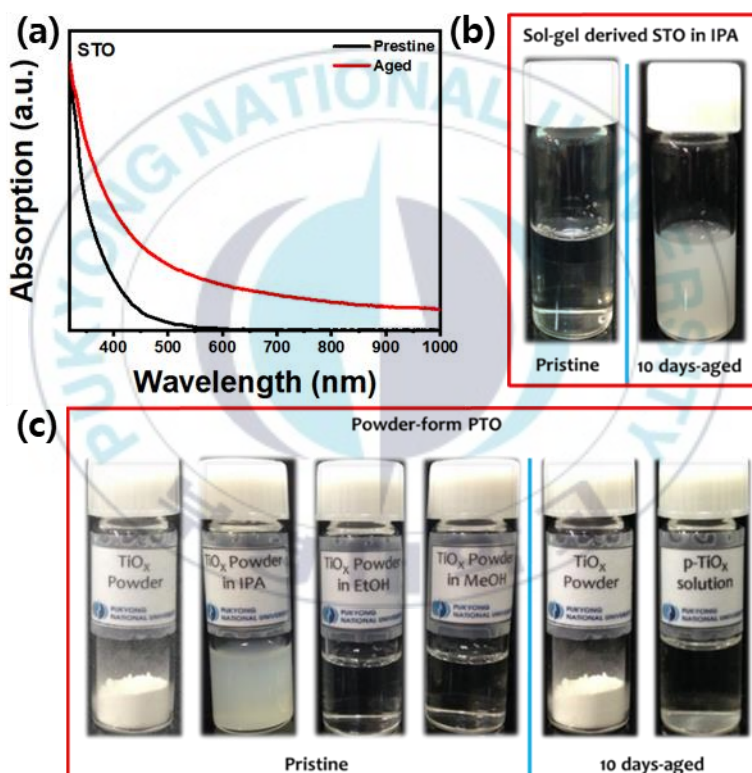


Figure 4-2. Absorption spectra of STO (a), and the picture of STO(b) and PTO before/after storage in ambient condition for 10 days and solubility of PTO in various solvent(c).

Figure 4-3 shows the XPS spectra of the film made with STO and PTO before and after exposure in ambient conditions. The O1s spectra of STO show three peaks at 529.9, 530.3 and 531.3 eV which attributed to TiO_2 , Ti_2O_3 and amorphous oxygen species including surface OH groups.^{122,123} In the case of STO, the peaks at 531.3 eV decrease with the increase of peaks at 529.9 eV which indicates severe hydrolysis of STO resulting insoluble TiO_2 . However, in the case of PTO, the change of peak intensity is strongly suppressed, indicates enhanced stability of PTO.

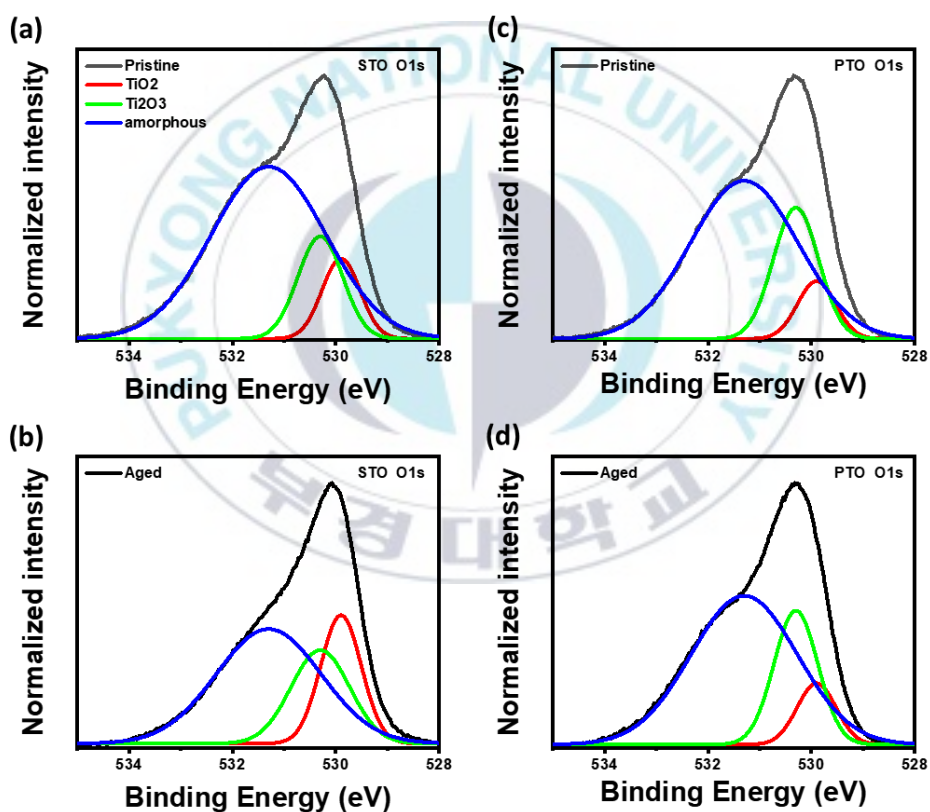


Figure 4-3. The XPS spectra of O1s in STO and PTO. (a) O1s spectra of STO before exposure to air, (b) after exposure to air. (c) O1s spectra of PTO before exposure to air, (d) after exposure to air.

(2) Properties of solid-state titanium sub-oxide

The chemical structure of synthesized PTO was verified with X-ray photoelectron spectroscopy (XPS), Fourier-transform infrared spectroscopy (FTIR) and X-ray diffraction (XRD) measurement. Figure 4-4 (a) presents the XPS spectra of N1s peaks for the synthesized PTO and TiO₂. The PTO exhibit N1s peaks that can't be seen from TiO₂, where shows the existence of amine groups. The N1s peaks of XPS show a double peak, each corresponds to a neutral amine (~399 eV) and positively charged N (~401 eV).¹²³ The existence of peak signal at ~401 eV for PTO shows the cationization of nitrogen in amine group due to the formation of ionic bonds with injected ions (i.e. formate ion), and which evidence the existence of salt formation between formate ion and amine group in PTO. Figure 4-4 (b) shows the FTIR spectra of PTO film. The peaks at 1900-2200 cm⁻¹ (corresponds to quaternary amine, R₄N⁺) and around 1500 cm⁻¹ (-C=O stretching from HCOO⁻) indicate the presence of quaternary amine salt (R₄N⁺HCOO⁻) on PTO.¹²⁴⁻¹²⁷ These results suggest that the addition of formic acid to a solution containing STO readily forms quaternary amine salt and which leads to precipitation of PTO with high purity. Figure 4-4 (c) shows the XRD spectra of PTO film. The XRD indicates that PTO maintains the amorphous nature of STO, infers that no crystallization takes place upon the precipitation. In addition, PTO appears to form a crystalline TiO₂ (anatase crystal form) after thermal treatment for 2 hours at 500 °C, which confirms that newly formed PTO is none other than titanium compounds.

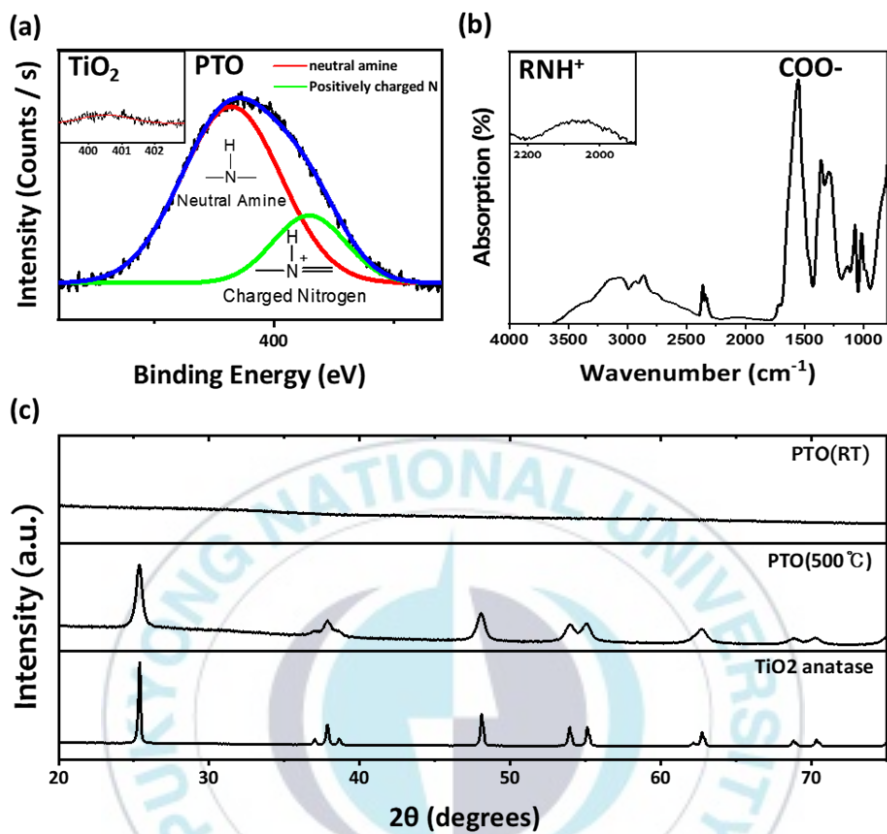


Figure 4-4. The chemical properties of PTO. (a) XPS N1s spectra (inset : N1s spectra of TiO₂), (b) FTIR, and (c) XRD of PTO film.

We investigated the film-forming ability of PTO using a methanolic solution of PTO precursor via spin casting method. As shown in the UV-Vis spectra and scanning electron microscope (SEM) image (Figure 4-5 (a) and (b)), the dense and transparent film is easily formed on top of the glass substrate. This fulfills the requirement for an optical spacer which redistributes the light intensity and enhances the light absorption of the solar cell. Figure 4-5 (c) shows the low contact angle (CA) of PTO (40.1°), indicates hydrophilicity of PTO film

surface which could form better interfacial contact when it introduced as an interfacial layer in the multi-layered device. Further, as could be seen from the Kelvin probe (KP) measurement (Figure 4-5 (d)), the PTO shown to modify the effective work function at the interface could induced by interfacial dipole as been reported from STO. The better interfacial contact with enhanced built-in electric field/ Ohmic contact at the interface by modification of effective work function could resulting better charge extraction accompanied with enhanced fill factor (FF) and open-circuit voltage (V_{oc}).

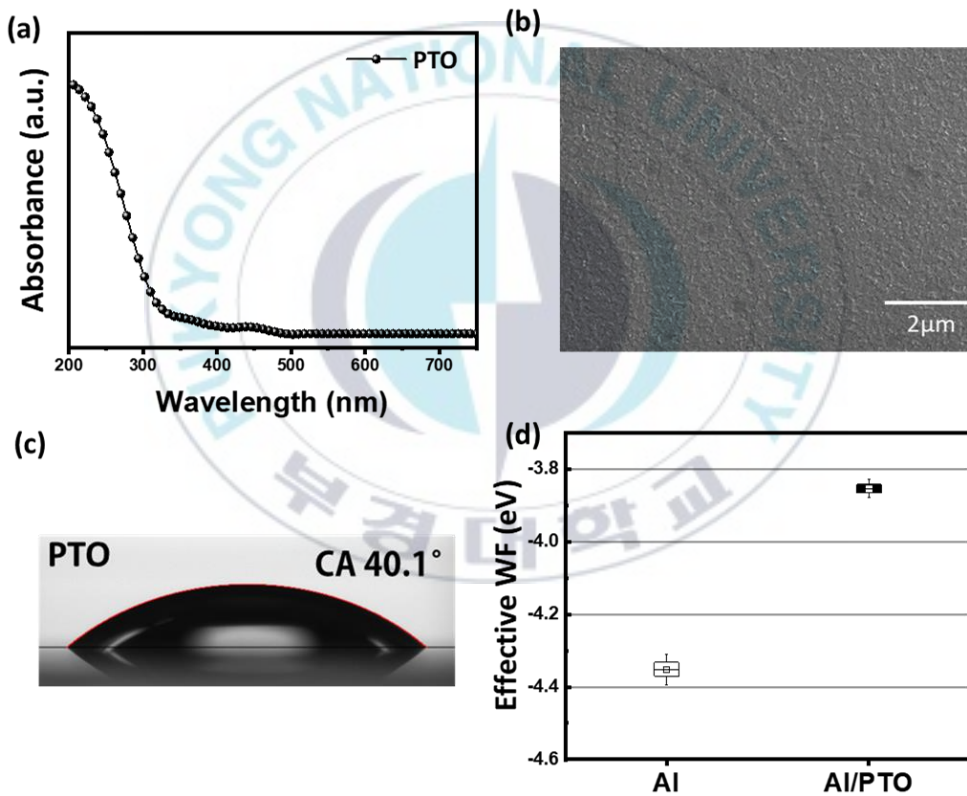


Figure 4-5. Properties of PTO film. (a) Absorption spectra, (b) FE-SEM image, and (c) contact angle of PTO film, (d) work function of aluminum with/without PTO film on top.

(3) Role of PTO interfacial layer on the photovoltaic performance

We fabricated PSCs using PTO interfacial layer with conventional device configuration, consisting of ITO/PEDOT:PSS/PTB7-Th:IEICO-4F/interlayer/Al (interlayer = none or PTO). The corresponding current density-voltage (J-V) characteristics (Figure 4-6 (b)) clearly shows an enhancement of overall device performance by insertion of PTO layer. The device without PTO gave a power conversion efficiency (PCE) of 9.11 % with V_{oc} at 0.71 V, a short circuit current density (J_{sc}) at 22.12 mA/cm², and FF at 0.58. When the PTO layer inserted at the interface, the PCE increased to 11.85 %, accompanied by remarkable enhancement in J_{sc} to 26.12 mA/cm² and FF to 0.63, while V_{oc} shows slight increment to 0.72 V. Further, the PCE versus storage time of a OSCs with/without PTO layer (Figure 4-6 (c)) shows drastic enhancement of device lifetime by incorporation of PTO. This result indicates that the PTO preserve the function as shielding and oxygen scavenging layer.

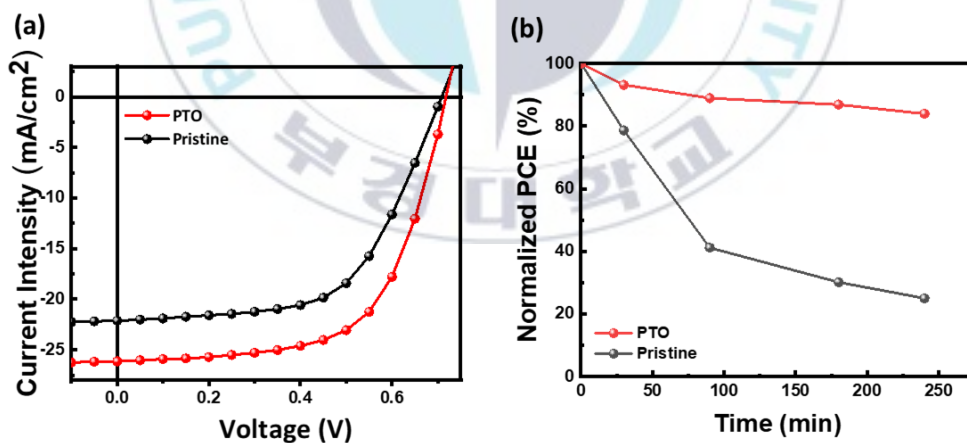


Figure 4-6. Performance of OSCs with/without PTO layer. (a) J-V characteristics and (b) normalized PCE as a function of storage time.

To analyze the remarkable enhancement in the J_{sc} , incident photon to current efficiency (IPCE) was investigated for the device with and without PTO layer. Figure 4-7 (a) shows an enhancement in IPCE, and the trend of enhancement is well matching with the reflection spectra shown in Figure 4-7 (b) which shows the enhancement of J_{sc} partially originated from the optical spacer effect. However the enhancement of overall performance factor including fill factor cannot solely explained by incorporation of optical spacer.

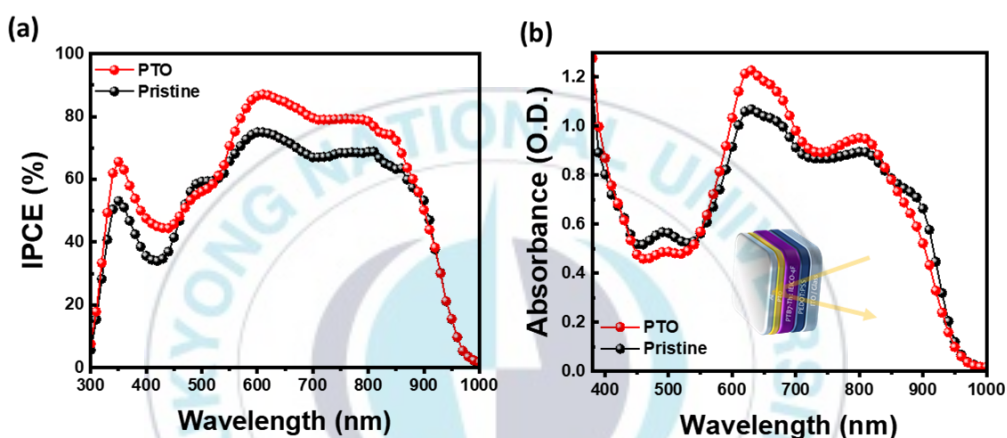


Figure 4-7. Role of PTO film as an optical spacer for OSCs. (a) IPCE and (b) Absorption spectra of OSCs with/without PTO in reflection geometry.

The enhancement in performance could be originated from the improved charge extraction due to modified energy level alignment at the interface, reduced surface trap and contact resistance as it could be expected from KP, CA, SEM result in Figure 4-5. In order to verify the role of the PTO layer on the carrier extraction/blocking at the interface, light intensity dependence of J_{sc} and V_{oc} , and dark J-V characteristics were performed. Figure 4-8 (a) shows the dependence of J_{sc} on light intensity. In general, J_{sc} under illumination follows a power-law dependence on light intensity ($J_{sc} \propto P^\alpha$), where the deviation of α from unity indicates the

strength of bimolecular recombination loss during charge transport process. The device with PTO exhibited higher α value (0.962) than the pristine device (0.931) which indicates more carriers are extracted prior to the bimolecular recombination with PTO layer.

In addition, the ideality factor of the device is obtained with the V_{oc} dependence on light intensity and dark J-V characteristics. The ideality factor is directly related to the generation-recombination process, thus a deviation of the ideality factor from unity implies non-ideal transport behavior due to recombination on the diode current through surface or interface states. The ideality factor from the dependence of V_{oc} on light intensity (light ideality factor, n_l) and from dark J-V characteristics (dark ideality factor, n_d) was derived using following equations.

$$n_l = \frac{q}{kT} \frac{dV_{oc}}{d \ln(P)} \quad n_d = \frac{q}{kT} \frac{dV_e}{d \ln(J_d)} \quad (4.1)$$

As shown in Figure 4-8 (b), (c) and (d), the resulting light and dark ideality factor from the device with the PTO layer were reduced from 1.4 to 1.27 and from 1.85 to 1.65, respectively. The deviation of ideality factor clearly indicates a reduction in recombination at the contact by forming better charge selective contact at the interface. The dark ideality factor achieved larger value than light ideality factor, matching with the previous study from Cowan et al. The study explained that the different carrier density dependence recombination mechanism imposes a crossover from trap-assisted recombination to bimolecular recombination under illumination. Furthermore, the saturation current density (J_s) decreased by a factor of 4 (from 4.137×10^{-6} to 2.32×10^{-10} mA/cm²) and shunt resistance (R_{sh}) increased 20 folds (from 8.76×10^2 to 1.70×10^4 Ω cm²) while the series resistance (R_s) show negligible

difference (from 1.34 to 1.42 Ωcm^2). The n , J_s , and R_{sh} are the factor reflects the recombination in the device. Especially, the reduction of J_s could imply the reduction of undesirable hole extraction through cathode interface by forming charge selective contact that may explain reduction of ideality factor.

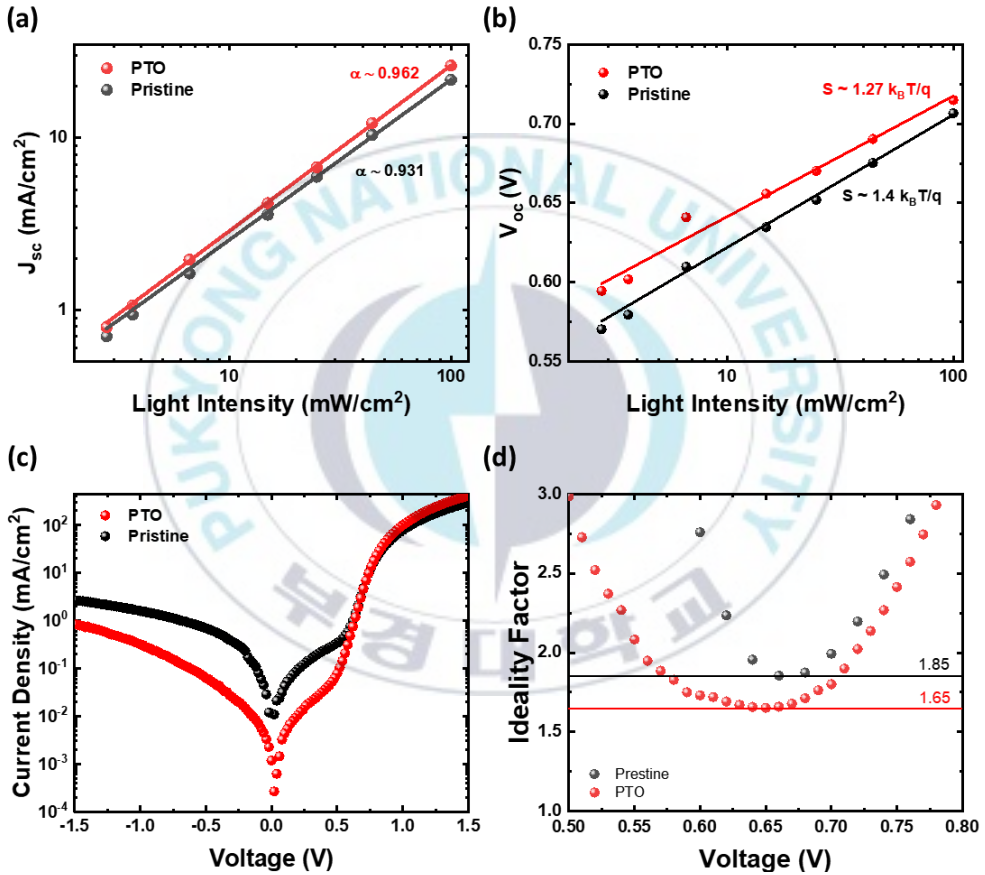


Figure 4-8. (a) J_{sc} and (b) V_{oc} dependence upon incident light intensity, (c) dark J-V characteristics of OSCs with/without PTO layer, and (d) calculated ideality factor from dark J-V characteristics.

For further analysis of interface dynamics, impedance spectroscopy (IS) has performed. Figure 4-9 show Nyquist plots of impedance measurement of devices with and without PTO layer. The data were fitted using an equivalent circuit model (ECM) in Figure 4-9 (c) and (d). For the device with PTO layer, ECM with a double RC exhibited the best match with Nyquist plot(Figure 4-9 (b)). However, the same model could not be applied for the pristine but required additional RC component which corresponds to previous study from Huiqiong et al (Figure 4-9 (a)). The additional RC components from ECM indicates the existence of significant surface trap for pristine device which may have disappeared upon incorporation of PTO layer. In addition to passivation of the surface trap, surface resistance (R_{sur}) has significantly reduced (from 487.08 to 24.33 Ωcm^2) indicates the charge transport at the interface has significantly improved by incorporation of PTO layer while the R_s maintained to be similar with incorporation of PTO layer which is in accord with the result from dark J-V characteristics.

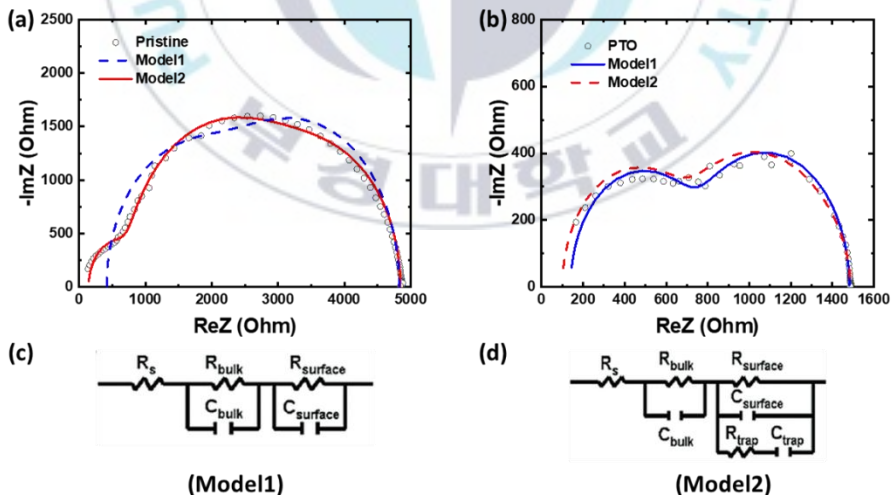


Figure 4-9. Nyquist plots of OSCs with(a) and without PTO layer(b) and equivalent circuit model without(c) and with additional interfacial trap.(d)

In order to confirm the universal effect of PTO, we fabricated solar cells using PTO interlayer with different active layers. Since the OSCs in our work is based on the non-fullerene acceptor, we fabricated PCDTBT:PC₇₀BM based OSC, and MAPbI₃/PCBM based perovskite solar cell (PeSC) to compare. The device structure, performance and IPCE results are displayed in Figure 4-10. The incorporation of PTO interfacial layer increases the PCE of OSC and PeSC from 4.81 to 5.87 % and 16.84 to 18.24 %, due to the enhancement of performance factors including J_{sc} , V_{oc} , and FF. These results clearly indicate that the role of PTO could be widely applied.

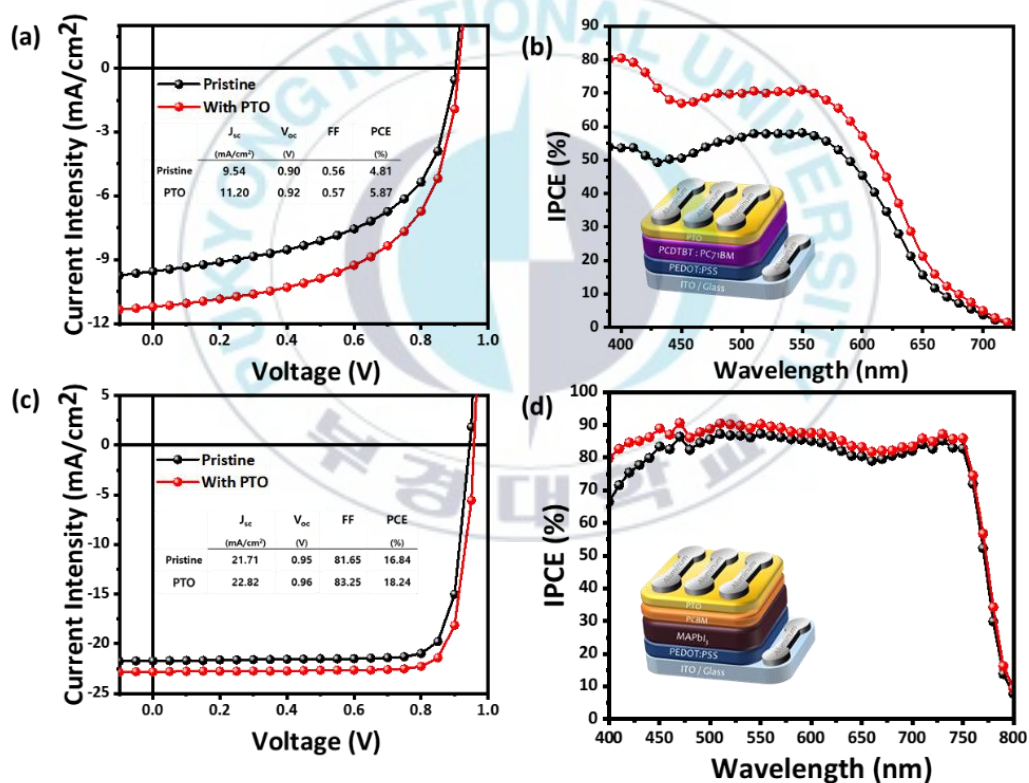


Figure 4-10. Performance of solar cells with/without PTO layer. (a) J-V characteristics and (b) IPCE of OSCs with PCDTBT:PC₇₀BM. (c) J-V characteristics and (d) IPCE of MAPbI₃ perovskite solar cells.

4.1.3 Conclusion

We developed a novel solution-processable powder-like titanium sub-oxide (PTO) precursor with the aim of improving the shelf-lifetime of sol-gel derived conventional titanium sub-oxide (STO) precursor. The inclusion of the formic acid to STO precursor in isopropyl alcohol (IPA) instantly precipitate the titanium sub-oxide through the salt formation between formate ions (HCOO^-) and amine groups ($-\text{NH}-$) in STO. The resulting PTO shows excellent stability in the ambient air compared to STO. By incorporation of the PTO layer as cathode interfacial layer, a high-efficiency polymer solar cell (PTB7-Th:IEICO-4F) with PCE of 11.85 % was achieved. The role of PTO interfacial layer in the enhancement of device efficiency is shown to result from the optical spacer effect and the formation of a charge selective contact by modification of the effective work function of the cathode and passivation of the surface traps. As a result of these effects, a significant improvement in PCE and device lifetime were achieved compared to that of devices made without a PTO interlayer. The advantages of PTO as a charge selective contact as well as high stability makes PTO a unique candidate as an interlayer.

4.2 Incorporation of Novel Metal Oxide based Functional Material in Perovskite Solar Cell

Organic-inorganic halide perovskite solar cells (PeSCs) have attracted significant attention as promising alternative energy sources due to their advantages of solution processability and high device performance originate from their superior physical/optical properties such as high absorption coefficient, ambipolar transport property, and long exciton diffusion length.

The performance of PeSCs is directly affected by the state of the perovskite layer, including crystallinity, film coverage, and grain size. The electrical properties of perovskite are shown to be strongly affected by the size of grain, cause of the existence of deep trap at the grain boundary. Therefore, grain boundary engineering is considered to be important in the field of PeSCs.

There are two ways of approach in grain boundary engineering to reducing the impact of grain boundary; (i) reducing the grain boundary by controlling the morphology, (ii) suppress the impact of the defect at the grain boundary by passivation. However, the larger grain size could accompany the undesirable wide vacancy at the grain boundary, thus it requires the methodologies to fine tune the morphology.

In this work, we studied the methodology to control the morphology of in perovskite layer. We developed a new method based on the impact of moisture and thermal annealing on the growing process of perovskite crystalline grains. Further, we have shown the impact of incorporating PTO on the crystalline growth, morphology, and passivation of defects.

4.2.1 Impact of morphology on perovskite solar cells¹²⁸

For high performing solar cells, high quality perovskite film with smooth, homogeneous, and pin-hole free surface with the larger grain is desirable.³⁹ The idea of MPT originated from the concept of slow-growth and solvent annealing method from OSCs, the existence of solvent vapor within the active layer could efficiently prolong the crystallization process, thus resulting in better film quality with higher grain size and crystallinity.^{129,130} Further, the moisture known to initiate the spontaneous recrystallization process, could result in merged grain boundaries, thus, better film coverage.¹³¹⁻¹³³ Meanwhile, the low thermal conductivity of perovskite and substrate could result in the temperature gradation between the top and bottom surface,¹³⁴ which induces undesirable non-homogeneous conformation and a low degree of coverage with smaller grain size. To solve this issue we replaced hot-plate with convection oven for annealing. (HAAP) The temperature gradient could severely be suppressed by simultaneously heating the top and the bottom with the convection oven.



Figure 4-11. Concept of HAAP.

To investigate the effect of each method, the sample prepared with each process and compared to each other. The spin-casted film changes the color from yellow to greenish-brown after the MPT, due to the hygroscopicity of methylammonium cation. In the MPT process, the quantity of moisture in the perovskite precursor film is a critical parameter for determining the moisture-induced recrystallization process, which is very sensitive to the exposure time as well as the humidity level. It is clear that the size of grain increases with the exposure time, indicating the recrystallization promoted by the MPT process and it is dependent on the quantity of moisture the film absorbed. However, the coverage of films starts to be affected over a certain quantity of moisture, thus we chose the 2 minutes for MPT which shown the best morphology.¹²⁸

The morphologies of the perovskite films prepared using the three different methods are shown in Figure 4-12. The conventionally formed film exhibited a rough and non-uniform film with low coverage. However, the morphology of the film with MPT process shows a smoother film with greater coverage and larger grain size. It is clearly shown that the remaining moisture due to the moisture pre-treatment could promote the better crystallization process since the moisture partially solvates the methylammonium component and allows the quicker formation of the perovskite phase. The highest quality perovskite film was obtained using HAAP. The HAAP perovskite film exhibited a significantly higher uniformity and greatest coverage with the largest grain size among the methods applied in this work.

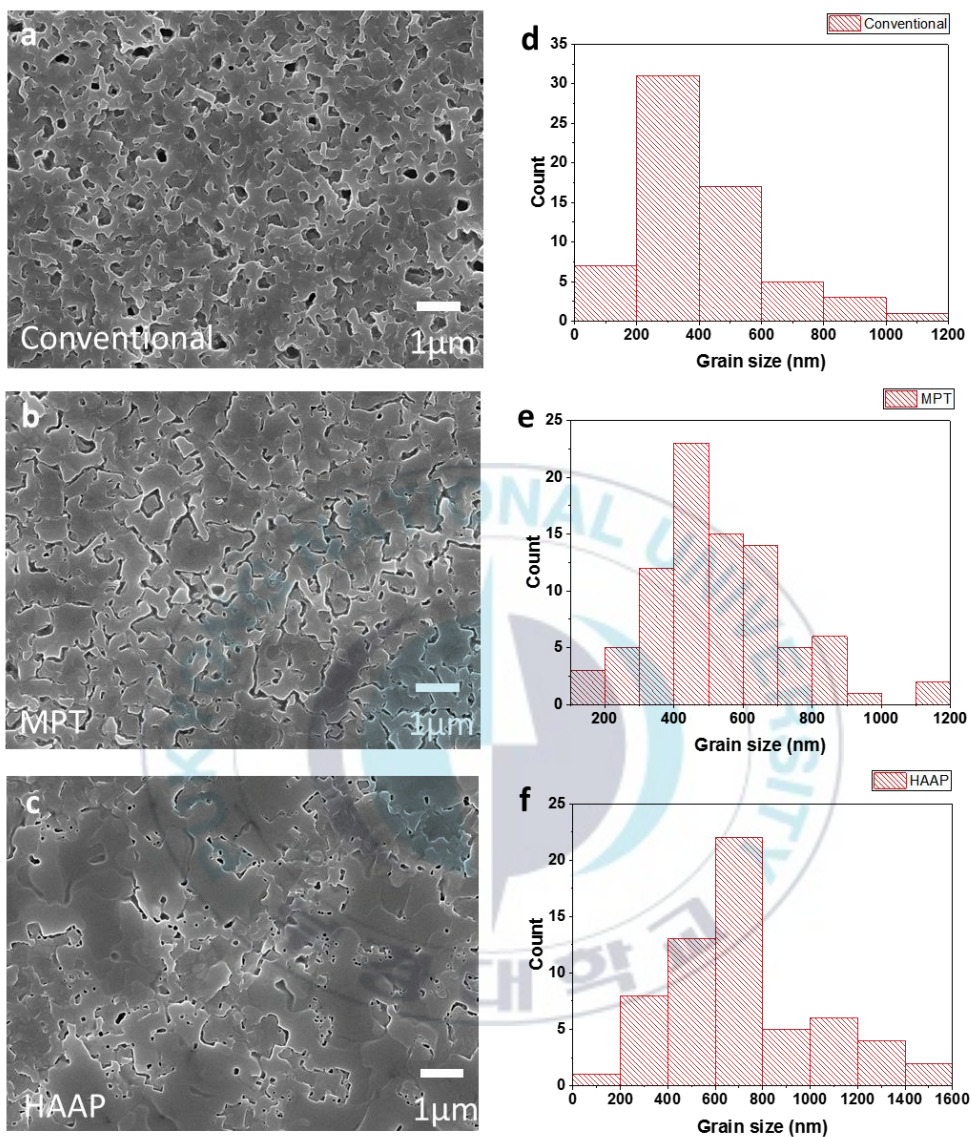


Figure 4-12. The top-view FE-SEM images of the perovskite films formed using the (a) conventional, (b) MPT, (c) HAAP method and (d-f) grain size distributions of the films.

To verify the correlation between the morphology and trap density, we have calculated the Urbach energy (E_U) for three perovskite films. The Urbach tail absorption is originated from sub-band gap absorption due to the electronic disorder of semiconductor. According to a previous study on perovskite crystalline structure, the defects of MAPbI_3 crystalline structure would be detected as a broadening of the Urbach tail. Therefore, the variation in the E_U would give a good estimation of the density of defects.^{135,136} Figure 4-13 shows the absorption spectra of the three films. The calculated E_U for the conventional, MPT and HAAP film was 28.8, 16.8, and 15.1 meV, respectively. Those values indicate that the lower level of energetic disorder for HAAP and MPT film compared to the conventional, which corresponding to a suppressed defect density. This clearly shows that the defect density is directly correlated to the morphology of perovskite film, especially the coverage and the size of grains.

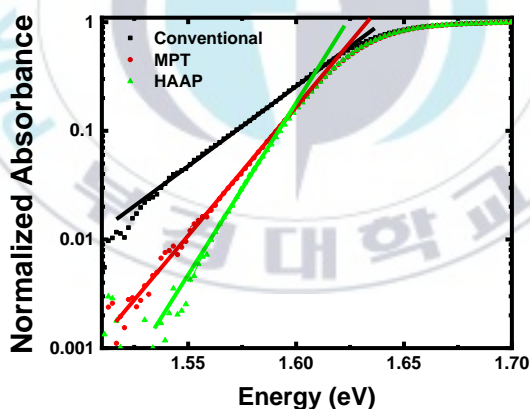


Figure 4-13. Absorption spectra of perovskite films.

4.2.2 Incorporation of metal oxide based functional material in perovskite

(1) Role of PTO on the morphology of perovskite

In case of our the titanium oxide based functional material(PTO), it could control the impact of moisture since it scavenges the water and oxygen while in undergoes hydrolysis reaction,^{9,121} and the lone-paired oxygen unit on the side chain of functional material could form a Lewis adduct and expected to modulate the crystallization process.^{48,49}

To investigate the role of PTO, we have prepared a solution of MAI, PbI₂, and DMSO with a molar ratio of 1:1:1 dissolved in DMF and various amount of PTO has added into the prepared solution. Figure 4-14 shows the morphology of perovskite film formed with various quantity of PTO. Interestingly, the gaps between each grains became narrower and the surface became smoother and more uniform while the grain size is almost unchanged. Since the uniformity and the coverage of film affects to device characteristics, the device with PTO expected to show higher performance due to suppressed recombination.

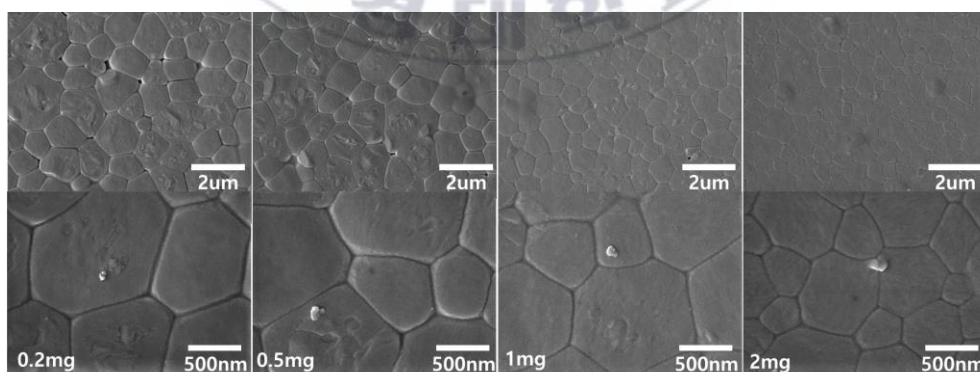


Figure 4-14. Impact of incorporating PTO on morphology of perovskite

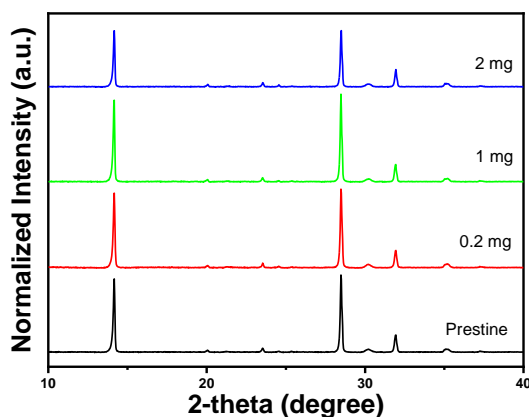


Figure 4-15. XRD spectra of perovskite films with various quantity of PTO incorporation.

Figure 4-15 presents the X-ray diffraction (XRD) patterns of the perovskite films prepared with various quantity of PTO. All the perovskite films show the peaks at 14.12, 28.46, and 31.85 in the XRD spectra, which corresponds to the (110), (220), and (310) crystal planes of perovskite. The XRD peaks are getting intensive and sharper as we increase the quantity of PTO up to 1mg/ml, indicating the high crystallinity of the perovskite films. Further, the film with 1mg/ml of PTO has highest peak ratio of (110) to (310), compared to the pristine film. The ratios were calculated to 4.1, 4.2, 4.7, and 3.4 for the pristine, the film with 0.5, 1, and 2 mg/ml of PTO, respectively. A higher peak ratio of (110)/(310) indicates highly (110)-oriented crystals with a long-range order parallel to the substrate, which beneficial for charge transport.^{50,137}

In order to verify the effect of the PTO incorporation, we fabricated PeSCs and investigated its characteristics. Figure 4-16 (a) shows the J-V characteristics of the device measured under the standard AM 1.5 G irradiation of 100 mW/cm². The conventionally fabricated device exhibited a reasonably high efficiency of 13.7 %, while the performance of

the device with PTO exhibited better performance of 14.5 % mainly due to the enhancement of J_{sc} from 18.6 mA/cm² to 19.9 mA/cm². To investigate the origin of the enhancement in performance light intensity dependence of J_{sc} and V_{oc} were performed. Figure 4-16 (b) shows the dependence of J_{sc} on light intensity. According to the power-law dependence on the light intensity, the device with PTO exhibited almost identical α value (~ 1) while the pristine device shows lower α value (~ 0.97) which indicates the bimolecular recombination has significantly suppressed by incorporation of PTO.^{21,138-140}

In addition, the ideality factor of the device is obtained with the V_{oc} dependence on light intensity. The ideality factor is directly related to the generation-recombination process, thus a deviation of the ideality factor from unity implies non-ideal transport behavior due to monomolecular recombination on the diode current through surface or interface states. The resulting light ideality factor from the device with the PTO layer was reduced from 1.8 to 1.3. The deviation of the ideality factor clearly indicates a reduction in recombination at the trap, due to the trap passivation by incorporation of PTO.^{109,119,138,139,141}

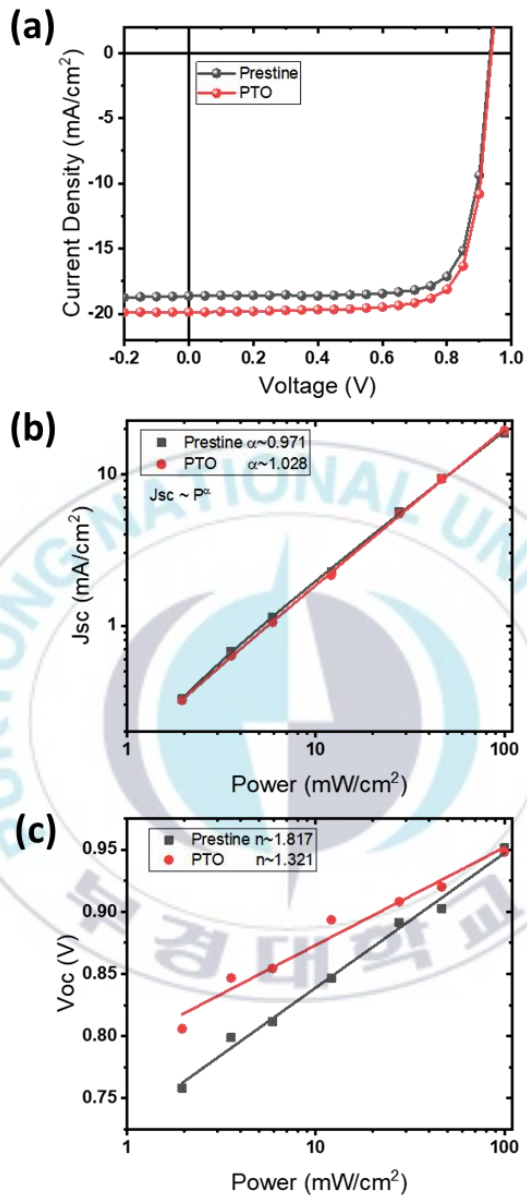


Figure 4-16. Impact of incorporating PTO in performance of perovskite solar cells. (a) J-V characteristics of device, (b) light intensity versus J_{sc}, and (c) light intensity versus V_{oc} of the device with/without PTO.

(2) Further work on the stability of perovskite

From the previous study on OSCs with PTO, we reported the stability of OSCs has improved due to PTO's role in protecting and oxygen/water scavenging layer. However, according to contact angle measurement(Figure 4-17), STO (52°) became more hydrophilic after forming PTO (40.8°) and therefore, there's still a concern that the water molecule could penetrate and disrupt the device stability if some pores exist within the film.

The aim of this work is to alter the nature of PTO to become hydrophobic, for better moisture protection. By partially (PTO-FA:SA) or fully replace the formic acid with hydrophobic stearic acid, we could successfully alter the nature of the resulting PTO (PTO-SA). Figure 4-17 shows the contact angle of the STO and PTO derived with formic acid, stearic acid, and the mixture of formic acid and stearic acid. The contact angle of the PTO has significantly altered by increasing the ratio of stearic acid during a synthetic procedure. This hydrophobic functional material is expected to enhance device stability, however, it still requires further optimization since the addition of stearic acid also increases the resistance of functional material.

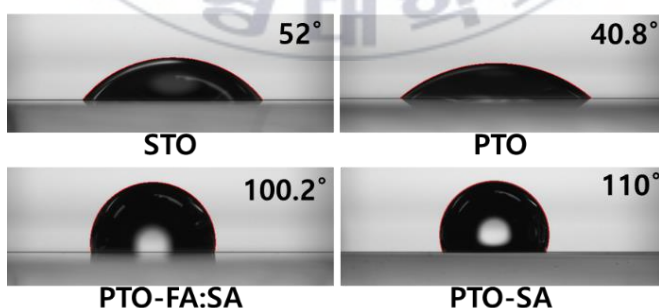


Figure 4-17. Contact angle of various titanium oxide based functional materials

In addition, PTO-SA has also incorporated into perovskite active layer to verify the impact of hydrophobic PTO on the stability of perovskite. Figure 4-18 shows the water contact angle of perovskite film with PTO, PTO-SA, and pristine perovskite film. The resulting contact angle has slightly increased as expected, accords with the addition of hydrophobic PTO. Interestingly the time-dependent contact angle shows a noticeable variation with PTO-SA, in contrast, the other film exhibits only negligible changes upon a time. This might because of the time lack between the disposition of the water and contact angle measurement. Since the methylammonium component in the MAPbI_3 perovskite is immediately dissolved right after the deposition of the water. However, the time-dependent contact angle of the perovskite with PTO-SA indicates that the PTO-SA in the perovskite repels the water and prolong the dissolution of the methylammonium component.

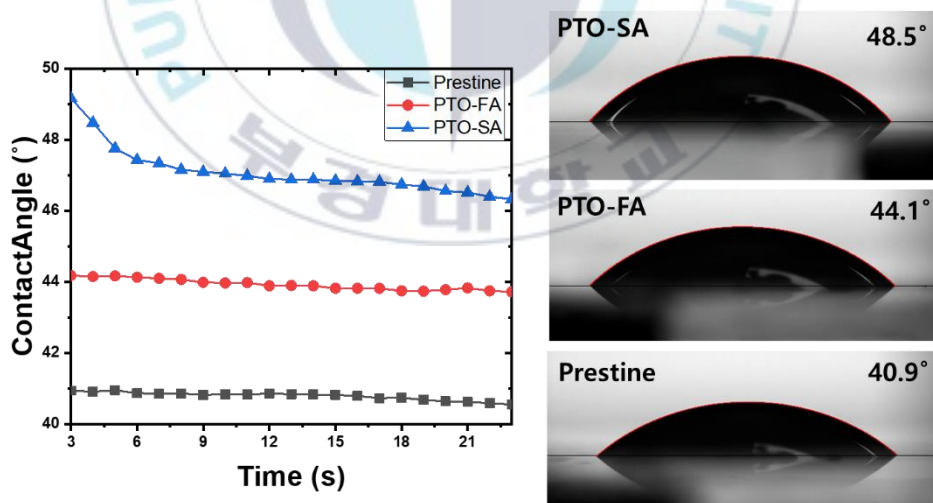


Figure 4-18. Contact angle of Perovskite with/without titanium oxide based functional materials

Chapter 5 Conclusion

This thesis focuses on the development of high performing soluble semiconducting functional materials and its application on organic polymer and halide perovskite based optoelectronic devices. A soluble semiconducting functional material is highly desired in the field of solution processed optoelectronic devices for the alteration of electronic properties and morphology of the active layer. The impact of a functional material could be varied depending on the position it is incorporated; from energy level alignment at the interface to the morphology of the active layer. On this basis, we developed two categories of functional materials, conjugated polymers as 3rd components of OSCs and a soluble metal oxide for interfacial engineering.

In the first chapter, we developed crystalline conjugated polymer as a 3rd component of ternary OSCs. The newly developed highly crystalline polymeric functional material was successfully incorporated and thereafter modified the carrier mobility of OSCs. By incorporating a small amount of crystalline polymeric functional material, the crystallinity of the BHJ layer improved, thereby significantly improving the mobility of the charge carriers. The OSCs with polymeric functional material exhibited enhanced IPCE owing to improved charge extraction with balanced mobility.

In the second chapter, we developed novel solution-processable powder-like titanium sub-oxide (PTO) precursor with the aim of improving the shelf-lifetime of sol-gel derived conventional titanium sub-oxide (STO) precursor. The resulting PTO showed excellent stability in the ambient air compared to STO. By incorporation of the PTO layer as a cathode

interfacial layer, a high-efficiency polymer solar cell (PTB7-Th:IEICO-4F) with PCE of 11.85 % was achieved. The role of the PTO interfacial layer in the enhancement of device efficiency was shown to result from the optical spacer effect and the formation of a charge selective contact by modification of the effective work function of the cathode and passivation of the surface traps.

In the last chapter, we studied the methodology required to control the morphology of solution processed perovskite layer. We developed a new method based on the impact of moisture and thermal annealing on the growing process of perovskite crystalline grains. Further, we have shown the possibility that, by incorporating the proper quantity of PTO functional material in the perovskite precursor solution, the crystalline growth could be controlled, and in turn the properties of perovskite film including morphology and electrical properties could be controlled.

In this work, I developed low-temperature solution processable functional materials and have demonstrated the role of our novel functional materials in photovoltaic application. Our newly developed soluble functional materials have shown great potential to hasten the commercialization of solution processable photovoltaics by modulating the characteristics of photovoltaics.

Chapter 6 References

1. Shirakawa, H., Louis, E. J., MacDiarmid, A. G., Chiang, C. K. & Heeger, A. J. Synthesis of electrically conducting organic polymers: halogen derivatives of polyacetylene, $(\text{CH})_x$. *J. Chem. Soc. Chem. Commun.* 578 (1977).
doi:10.1039/c39770000578
2. Heeger, A. J., Kivelson, S., Schrieffer, J. R. & Su, W.-P. Solitons in conducting polymers. *Rev. Mod. Phys.* **60**, 781–850 (1988).
3. Heeger, A. J. Semiconducting and metallic polymers: The fourth generation of polymeric materials. *Curr. Appl. Phys.* **1**, 247–267 (2001).
4. Li, G., Zhu, R. & Yang, Y. Polymer solar cells. *Nat. Photonics* **6**, 153–161 (2012).
5. Heeger, A. J. 25th anniversary article: Bulk heterojunction solar cells: understanding the mechanism of operation. *Adv. Mater.* **26**, 10–27 (2014).
6. Gurney, R. S., Lidzey, D. G. & Wang, T. A review of non-fullerene polymer solar cells: From device physics to morphology control. *Reports Prog. Phys.* **82**, (2019).
7. Gusain, A., Faria, R. M. & Miranda, P. B. Polymer solar cells-interfacial processes related to performance issues. *Front. Chem.* **7**, (2019).
8. Zhang, C. *et al.* Understanding the correlation and balance between the miscibility and optoelectronic properties of polymer-fullerene solar cells. *J. Mater. Chem. A* **5**, 17570–17579 (2017).

9. Lee, K. *et al.* Air-stable polymer electronic devices. *Adv. Mater.* **19**, 2445–2449 (2007).
10. Galuskin, E. V. *et al.* Lakargiite CaZrO₃: A new mineral of the perovskite group from the North Caucasus, Kabardino-Balkaria, Russia. *Am. Mineral.* **93**, 1903–1910 (2008).
11. Jeng, J. Y. *et al.* CH₃NH₃PbI₃ perovskite/fullerene planar-heterojunction hybrid solar cells. *Adv. Mater.* **25**, 3727–3732 (2013).
12. Zhou, H. *et al.* Interface engineering of highly efficient perovskite solar cells. *Science* **345**, 542–546 (2014).
13. Chen, B., Rudd, P. N., Yang, S., Yuan, Y. & Huang, J. Imperfections and their passivation in halide perovskite solar cells. *Chem. Soc. Rev.* **48**, 3842–3867 (2019).
14. Zhao, P., Kim, B. J. & Jung, H. S. Passivation in perovskite solar cells: A review. *Mater. Today Energy* **7**, 267–286 (2018).
15. Jena, A. K., Kulkarni, A. & Miyasaka, T. Halide Perovskite Photovoltaics: Background, Status, and Future Prospects. *Chem. Rev.* **119**, 3036–3103 (2019).
16. Wetzelaer, G. J. A. H. & Blom, P. W. M. Diffusion-driven currents in organic-semiconductor diodes. *NPG Asia Mater.* **6**, e110-13 (2014).
17. Markvart, T. & Castañer, L. Principles of Solar Cell Operation. *Sol. Cells* 3–25 (2013). doi:10.1016/B978-0-12-386964-7.00001-9
18. Breitenstein, O. Understanding the current-voltage characteristics of industrial

- crystalline silicon solar cells by considering inhomogeneous current distributions. *Opto-Electronics Rev.* **21**, 259–282 (2013).
19. Servaites, J. D., Ratner, M. A. & Marks, T. J. Organic solar cells: A new look at traditional models. *Energy Environ. Sci.* **4**, 4410–4422 (2011).
 20. Proctor, C. M. & Nguyen, T. Q. Effect of leakage current and shunt resistance on the light intensity dependence of organic solar cells. *Appl. Phys. Lett.* **106**, (2015).
 21. Cowan, S. R., Roy, A. & Heeger, A. J. Recombination in polymer-fullerene bulk heterojunction solar cells. *Phys. Rev. B - Condens. Matter Mater. Phys.* **82**, 1–10 (2010).
 22. Elumalai, N. K. & Uddin, A. Open circuit voltage of organic solar cells: an in-depth review. *Energy Environ. Sci.* **9**, 391–410 (2016).
 23. Lattante, S. Electron and Hole Transport Layers: Their Use in Inverted Bulk Heterojunction Polymer Solar Cells. *Electronics* **3**, 132–164 (2014).
 24. Zhang, X. *et al.* A solution-processed binary cathode interfacial layer facilitates electron extraction for inverted polymer solar cells. *J. Colloid Interface Sci.* **514**, 328–337 (2018).
 25. Kim, G. *et al.* Overcoming the light-soaking problem in inverted polymer solar cells by introducing a heavily doped titanium sub-oxide functional layer. *Adv. Energy Mater.* **5**, 21–23 (2015).
 26. Seo, J. H., Kim, H. & Cho, S. Build-up of symmetry breaking using a titanium

- suboxide in bulk-heterojunction solar cells. *Phys. Chem. Chem. Phys.* **14**, 4062–4065 (2012).
27. Yeh, Y. C. *et al.* Stoichiometric dependence of TiO_x as a cathode modifier on band alignment of polymer solar cells. *Sol. Energy Mater. Sol. Cells* **125**, 233–238 (2014).
28. Tada, A. *et al.* Interfacial modification of organic photovoltaic devices by molecular self-organization. *Phys. Chem. Chem. Phys.* **14**, 3713–3724 (2012).
29. Chueh, C. C., Li, C. Z. & Jen, A. K. Y. Recent progress and perspective in solution-processed Interfacial materials for efficient and stable polymer and organometal perovskite solar cells. *Energy Environ. Sci.* **8**, 1160–1189 (2015).
30. Park, S. H. *et al.* Bulk heterojunction solar cells with internal quantum efficiency approaching 100. *Nat. Photonics* **3**, 297–302 (2009).
31. Lee, B. H., Coughlin, J., Kim, G., Bazan, G. C. & Lee, K. Efficient solution-processed small-molecule solar cells with titanium suboxide as an electric adhesive layer. *Appl. Phys. Lett.* **104**, (2014).
32. Roy, A. *et al.* Titanium suboxide as an optical spacer in polymer solar cells. *Appl. Phys. Lett.* **95**, 013302 (2009).
33. Kim, J. Y. *et al.* New Architecture for High-Efficiency Polymer Photovoltaic Cells Using Solution-Based Titanium Oxide as an Optical Spacer. *Adv. Mater.* **18**, 572–576 (2006).

34. Lee, J. K. *et al.* Efficacy of Ti Ox optical spacer in bulk-heterojunction solar cells processed with 1,8-octanedithiol. *Appl. Phys. Lett.* **92**, 1–4 (2008).
35. Zhang, L. Q. *et al.* Highly efficient and stable planar heterojunction perovskite solar cells via a low temperature solution process. *J. Mater. Chem. A* **3**, 12133–12138 (2015).
36. Shin, H. Y. & Suh, M. C. Effect of the thermal evaporation rate of Al cathodes on organic light emitting diodes. *Mater. Sci. Eng. B* **188**, 8–12 (2014).
37. Reddy, S. S. *et al.* Lewis acid-base adduct-type organic hole transport material for high performance and air-stable perovskite solar cells. *Nano Energy* **58**, 284–292 (2019).
38. Idígoras, J. *et al.* The interaction between hybrid organic-inorganic halide perovskite and selective contacts in perovskite solar cells: An infrared spectroscopy study. *Phys. Chem. Chem. Phys.* **18**, 13583–13590 (2016).
39. Li, Y. *et al.* A review on morphology engineering for highly efficient and stable hybrid perovskite solar cells. *J. Mater. Chem. A* **6**, 12842–12875 (2018).
40. Sahare, S., Veldurthi, N., Datar, S. & Bhave, T. Photon assisted conducting atomic force microscopy study of nanostructured additives in P3HT:PCBM. *RSC Adv.* **5**, 102795–102802 (2015).
41. Yu, R. *et al.* Design and application of volatilizable solid additives in non-fullerene organic solar cells. *Nat. Commun.* **9**, 4645 (2018).

42. Yu, R. *et al.* Enhanced π - π Interactions of Nonfullerene Acceptors by Volatilizable Solid Additives in Efficient Polymer Solar Cells. *Adv. Mater.* **31**, 1900477 (2019).
43. Nian, L. *et al.* Ternary non-fullerene polymer solar cells with 13.51% efficiency and a record-high fill factor of 78.13%. *Energy Environ. Sci.* **11**, 3392–3399 (2018).
44. Zhang, L. & Ma, W. Morphology optimization in ternary organic solar cells. *Chinese J. Polym. Sci. (English Ed.)* **35**, 184–197 (2017).
45. Ma, Y. *et al.* Understanding and Tailoring Grain Growth of Lead-Halide Perovskite for Solar Cell Application. *ACS Appl. Mater. Interfaces* **9**, 33925–33933 (2017).
46. Liu, Y. *et al.* Single-Crystal-like Perovskite for High-Performance Solar Cells Using the Effective Merged Annealing Method. *ACS Appl. Mater. Interfaces* **9**, 12382–12390 (2017).
47. Liu, Y. *et al.* Bulk Heterojunction-Assisted Grain Growth for Controllable and Highly Crystalline Perovskite Films. *ACS Appl. Mater. Interfaces* **10**, 31366–31373 (2018).
48. Lee, J. W., Kim, H. S. & Park, N. G. Lewis Acid-Base Adduct Approach for High Efficiency Perovskite Solar Cells. *Acc. Chem. Res.* **49**, 311–319 (2016).
49. Cao, X. B. *et al.* High quality perovskite films fabricated from Lewis acid-base adduct through molecular exchange. *RSC Adv.* **6**, 70925–70931 (2016).
50. Ma, Y. *et al.* Controlled crystal facet of MAPbI₃ perovskite for highly efficient and stable solar cell via nucleation modulation. *Nanoscale* **11**, 170–177 (2019).

51. Zhang, F. & Zhu, K. Additive Engineering for Efficient and Stable Perovskite Solar Cells. *Adv. Energy Mater.* 1902579 (2019). doi:10.1002/aenm.201902579
52. Cai, Y., Huo, L. & Sun, Y. Recent Advances in Wide-Bandgap Photovoltaic Polymers. *Adv. Mater.* **29**, 1605437 (2017).
53. Lu, L. *et al.* Recent Advances in Bulk Heterojunction Polymer Solar Cells. *Chem. Rev.* **115**, 12666–12731 (2015).
54. Zhang, G. *et al.* Nonfullerene Acceptor Molecules for Bulk Heterojunction Organic Solar Cells. *Chem. Rev.* **118**, 3447–3507 (2018).
55. Yan, C. *et al.* Non-fullerene acceptors for organic solar cells. *Nat. Rev. Mater.* **3**, 18003 (2018).
56. Carlé, J. E. *et al.* Overcoming the Scaling Lag for Polymer Solar Cells. *Joule* **1**, 274–289 (2017).
57. Gu, X. *et al.* Roll-to-Roll Printed Large-Area All-Polymer Solar Cells with 5% Efficiency Based on a Low Crystallinity Conjugated Polymer Blend. *Adv. Energy Mater.* **7**, 1602742 (2017).
58. Kim, T. *et al.* Flexible, highly efficient all-polymer solar cells. *Nat. Commun.* **6**, 8547 (2015).
59. Gasparini, N., Salleo, A., McCulloch, I. & Baran, D. The role of the third component in ternary organic solar cells. *Nat. Rev. Mater.* **4**, 229–242 (2019).
60. Liu, X., Yan, Y., Yao, Y. & Liang, Z. Ternary Blend Strategy for Achieving High-

- Efficiency Organic Solar Cells with Nonfullerene Acceptors Involved. *Adv. Funct. Mater.* **28**, 1802004 (2018).
61. Hosseini, P., Wright, C. D. & Bhaskaran, H. An optoelectronic framework enabled by low-dimensional phase-change films. *Nature* **511**, 206–211 (2014).
62. Huang, W., Cheng, P., Yang, Y. M., Li, G. & Yang, Y. High-Performance Organic Bulk-Heterojunction Solar Cells Based on Multiple-Donor or Multiple-Acceptor Components. *Adv. Mater.* **30**, 1705706 (2018).
63. An, Q. *et al.* Versatile ternary organic solar cells: a critical review. *Energy Environ. Sci.* **9**, 281–322 (2016).
64. Lu, L., Kelly, M. A., You, W. & Yu, L. Status and prospects for ternary organic photovoltaics. *Nat. Photonics* **9**, 491–500 (2015).
65. Yang, Y. (Michael) *et al.* High-performance multiple-donor bulk heterojunction solar cells. *Nat. Photonics* **9**, 190–198 (2015).
66. Ameri, T., Khoram, P., Min, J. & Brabec, C. J. Organic Ternary Solar Cells: A Review. *Adv. Mater.* **25**, 4245–4266 (2013).
67. Tamilavan, V. *et al.* Synthesis and characterization of indenofluorene-based copolymers containing 2,5-bis(2-thienyl)-N-arylpyrrole for bulk heterojunction solar cells and polymer light-emitting diodes. *J. Polym. Sci. Part A Polym. Chem.* **48**, 3169–3177 (2010).
68. Agneeswari, R. *et al.* Opto-electrical, charge transport and photovoltaic property

- modulation of 2,5-di(2-thienyl)pyrrole-based polymers via the incorporation of alkyl, aryl and cyano groups on the pyrrole unit. *Polym. Bull.* **72**, 1899–1919 (2015).
69. Tamilavan, V., Song, M., Jin, S.-H. & Hyun, M. H. Synthesis of three new 1-(2,6-diisopropylphenyl)-2,5-di(2-thienyl) pyrrole-based donor polymers and their bulk heterojunction solar cell applications. *J. Polym. Sci. Part A Polym. Chem.* **48**, 5514–5521 (2010).
70. Brabec, C. J. *et al.* A Low-Bandgap Semiconducting Polymer for Photovoltaic Devices and Infrared Emitting Diodes. *Adv. Funct. Mater.* **12**, 709–712 (2002).
71. Tamilavan, V., Song, M., Jin, S.-H. & Hyun, M. H. Synthesis of conjugated polymers with broad absorption bands and photovoltaic properties as bulk heterojunction solar cells. *Polymer* **52**, 2384–2390 (2011).
72. Tamilavan, V., Song, M., Jin, S.-H. & Hyun, M. H. Synthesis and photovoltaic properties of heteroaromatic low-band gap oligomers for bulk heterojunction solar cells. *Synth. Met.* **161**, 1199–1206 (2011).
73. Tamilavan, V. *et al.* Pyrrolo[3,4-c]pyrrole-1,3-dione-based large band gap polymers containing benzodithiophene derivatives for highly efficient simple structured polymer solar cells. *J. Polym. Sci. Part A Polym. Chem.* **52**, 3564–3574 (2014).
74. Tamilavan, V. *et al.* Pyrrole N -alkyl side chain effects on the properties of pyrrolo[3,4- c]pyrrole-1,3-dione-based polymers for polymer solar cells. *New J. Chem.* **42**, 12045–12053 (2018).
75. Agneeswari, R. *et al.* Modulation of the properties of pyrrolo[3,4-c]pyrrole-1,4-

- dione based polymers containing 2,5-di(2-thienyl)pyrrole derivatives with different substitutions on the pyrrole unit. *New J. Chem.* **39**, 4658–4669 (2015).
76. Li, S. *et al.* A Wide Band Gap Polymer with a Deep Highest Occupied Molecular Orbital Level Enables 14.2% Efficiency in Polymer Solar Cells. *J. Am. Chem. Soc.* **140**, 7159–7167 (2018).
77. Zhang, S., Qin, Y., Zhu, J. & Hou, J. Over 14% Efficiency in Polymer Solar Cells Enabled by a Chlorinated Polymer Donor. *Adv. Mater.* **30**, 1800868 (2018).
78. Li, H., Zheng, X., Wang, X., Liu, F. & Fu, H. Effect of chain curvature on the performance of diketopyrrolopyrrole-based polymer solar cells. *Polym. Chem.* **6**, 6637–6643 (2015).
79. Gallaher, J. K. *et al.* Spectroscopically tracking charge separation in polymer : fullerene blends with a three-phase morphology. *Energy Environ. Sci.* **8**, 2713–2724 (2015).
80. Vezie, M. S. *et al.* Exploring the origin of high optical absorption in conjugated polymers. *Nat. Mater.* **15**, 746–753 (2016).
81. Rong, Y. *et al.* Challenges for commercializing perovskite solar cells. *Science* **361**, eaat8235 (2018).
82. Che, X., Li, Y., Qu, Y. & Forrest, S. R. High fabrication yield organic tandem photovoltaics combining vacuum- and solution-processed subcells with 15% efficiency. *Nat. Energy* **3**, 422–427 (2018).

83. Chen, S. *et al.* A Nonfullerene Semitransparent Tandem Organic Solar Cell with 10.5% Power Conversion Efficiency. *Adv. Energy Mater.* **8**, 1800529 (2018).
84. Zhang, Y. *et al.* Nonfullerene Tandem Organic Solar Cells with High Performance of 14.11%. *Adv. Mater.* **30**, 1707508 (2018).
85. Zheng, Z. *et al.* Over 11% Efficiency in Tandem Polymer Solar Cells Featured by a Low-Band-Gap Polymer with Fine-Tuned Properties. *Adv. Mater.* **28**, 5133–5138 (2016).
86. Park, S. H. *et al.* Tandem Solar Cells Made from Amorphous Silicon and Polymer Bulk Heterojunction Sub-Cells. *Adv. Mater.* **27**, 298–302 (2015).
87. Ameri, T., Li, N. & Brabec, C. J. Highly efficient organic tandem solar cells: a follow up review. *Energy Environ. Sci.* **6**, 2390 (2013).
88. Ameri, T., Dennler, G., Lungenschmied, C. & Brabec, C. J. Organic tandem solar cells: A review. *Energy Environ. Sci.* **2**, 347 (2009).
89. Kim, J. Y. *et al.* Efficient Tandem Polymer Solar Cells Fabricated by All-Solution Processing. *Science* **317**, 222–225 (2007).
90. Aqoma, H. *et al.* 11% Organic Photovoltaic Devices Based on PTB7-Th: PC 71 BM Photoactive Layers and Irradiation-Assisted ZnO Electron Transport Layers. *Adv. Sci.* **5**, 1700858 (2018).
91. Liao, S.-H., Jhuo, H.-J., Cheng, Y.-S. & Chen, S.-A. Fullerene Derivative-Doped Zinc Oxide Nanofilm as the Cathode of Inverted Polymer Solar Cells with Low-

- Bandgap Polymer (PTB7-Th) for High Performance. *Adv. Mater.* **25**, 4766–4771 (2013).
92. Chen, J.-D. *et al.* Single-Junction Polymer Solar Cells Exceeding 10% Power Conversion Efficiency. *Adv. Mater.* **27**, 1035–1041 (2015).
93. He, Z. *et al.* Single-junction polymer solar cells with high efficiency and photovoltage. *Nat. Photonics* **9**, 174–179 (2015).
94. Chang, W.-H. *et al.* A Selenophene Containing Benzodithiophene- alt - thienothiophene Polymer for Additive-Free High Performance Solar Cell. *Macromolecules* **48**, 562–568 (2015).
95. Lee, J. *et al.* Overcoming Fill Factor Reduction in Ternary Polymer Solar Cells by Matching the Highest Occupied Molecular Orbital Energy Levels of Donor Polymers. *Adv. Energy Mater.* **8**, 1702251 (2018).
96. Chen, Y. *et al.* Achieving High-Performance Ternary Organic Solar Cells through Tuning Acceptor Alloy. *Adv. Mater.* **29**, 1603154 (2017).
97. Xiao, Z., Jia, X. & Ding, L. Ternary organic solar cells offer 14% power conversion efficiency. *Sci. Bull.* **62**, 1562–1564 (2017).
98. Li, H., Xiao, Z., Ding, L. & Wang, J. Thermostable single-junction organic solar cells with a power conversion efficiency of 14.62%. *Sci. Bull.* **63**, 340–342 (2018).
99. Zhang, S. *et al.* Efficient and 1,8-diiodooctane-free ternary organic solar cells fabricated via nanoscale morphology tuning using small-molecule dye additive.

- Nano Res.* **10**, 3765–3774 (2017).
100. Wang, C. *et al.* Ternary organic solar cells with enhanced open circuit voltage. *Nano Energy* **37**, 24–31 (2017).
 101. Wang, Y. *et al.* A small molecule/fullerene binary acceptor system for high-performance polymer solar cells with enhanced light-harvesting properties and balanced carrier mobility. *J. Mater. Chem. A* **5**, 2460–2465 (2017).
 102. Chen, Y. *et al.* From Binary to Ternary: Improving the External Quantum Efficiency of Small-Molecule Acceptor-Based Polymer Solar Cells with a Minute Amount of Fullerene Sensitization. *Adv. Energy Mater.* **7**, 1700328 (2017).
 103. Tamilavan, V. *et al.* Efficient pyrrolo[3,4- c]pyrrole-1,3-dione-based wide band gap polymer for high-efficiency binary and ternary solar cells. *Polymer* **125**, 182–189 (2017).
 104. Gasparini, N. *et al.* High-performance ternary organic solar cells with thick active layer exceeding 11% efficiency. *Energy Environ. Sci.* **10**, 885–892 (2017).
 105. Kumari, T., Lee, S. M., Kang, S.-H., Chen, S. & Yang, C. Ternary solar cells with a mixed face-on and edge-on orientation enable an unprecedented efficiency of 12.1%. *Energy Environ. Sci.* **10**, 258–265 (2017).
 106. Zhao, W., Li, S., Zhang, S., Liu, X. & Hou, J. Ternary Polymer Solar Cells based on Two Acceptors and One Donor for Achieving 12.2% Efficiency. *Adv. Mater.* **29**, 1604059 (2017).

107. Lee, T. H. *et al.* Investigation of Charge Carrier Behavior in High Performance Ternary Blend Polymer Solar Cells. *Adv. Energy Mater.* **6**, 1600637 (2016).
108. Lu, L., Chen, W., Xu, T. & Yu, L. High-performance ternary blend polymer solar cells involving both energy transfer and hole relay processes. *Nat. Commun.* **6**, 7327 (2015).
109. Tamilavan, V. *et al.* Highly crystalline new benzodithiophene–benzothiadiazole copolymer for efficient ternary polymer solar cells with an energy conversion efficiency of over 10%. *J. Mater. Chem. C* **6**, 4281–4289 (2018).
110. Zhang, J. *et al.* Conjugated Polymer–Small Molecule Alloy Leads to High Efficient Ternary Organic Solar Cells. *J. Am. Chem. Soc.* **137**, 8176–8183 (2015).
111. Park, K. H., An, Y., Jung, S., Park, H. & Yang, C. Locking-In Optimal Nanoscale Structure Induced by Naphthalenediimide-Based Polymeric Additive Enables Efficient and Stable Inverted Polymer Solar Cells. *ACS Nano* **11**, 7409–7415 (2017).
112. Li, Z. *et al.* Highly efficient polymer solar cells via multiple cascade energy level engineering. *J. Mater. Chem. C* **6**, 9119–9129 (2018).
113. Wang, N., Chen, Z., Wei, W. & Jiang, Z. Fluorinated Benzothiadiazole-Based Conjugated Polymers for High-Performance Polymer Solar Cells without Any Processing Additives or Post-treatments. *J. Am. Chem. Soc.* **135**, 17060–17068 (2013).
114. Tamilavan, V. *et al.* Property modulation of dithienosilole-based polymers via the incorporation of structural isomers of imide- and lactam-functionalized pyrrolo[3,4-

- c]pyrrole units for polymer solar cells. *Polymer* **65**, 243–252 (2015).
115. Tamilavan, V., Song, M., Jin, S.-H. & Hyun, M. H. Synthesis and application of low band gap broad absorption oligomers based on 2,5-bis(2-thienyl)-N-arylpyrrole for bulk heterojunction solar cells. *Curr. Appl. Phys.* **12**, S124–S130 (2012).
116. Tamilavan, V. *et al.* Synthesis of N-[4-Octylphenyl]dithieno[3,2-b:2',3'-d]pyrrole-based broad absorbing polymers and their photovoltaic applications. *Polymer* **54**, 3198–3205 (2013).
117. Agneeswari, R., Tamilavan, V., Song, M. & Hyun, M. H. Property modulation of benzodithiophene-based polymers via the incorporation of a covalently bonded novel 2,1,3-benzothiadiazole-1,2,4-oxadiazole derivative in their main chain for polymer solar cells. *J. Mater. Chem. C* **2**, 8515–8524 (2014).
118. Tamilavan, V. *et al.* Side-chain influences on the properties of benzodithiophene-alt-di(thiophen-2-yl)quinoxaline polymers for fullerene-free organic solar cells. *Polymer* **172**, 305–311 (2019).
119. Shin, S. S., Lee, S. J. & Seok, S. II. Metal Oxide Charge Transport Layers for Efficient and Stable Perovskite Solar Cells. *Adv. Funct. Mater.* **1900455**, 1–30 (2019).
120. Kim, H., Hwa Seo, J. & Cho, S. Effect of a symmetry breaking layer on the open circuit voltage of conventional bulk-heterojunction solar cells. *Appl. Phys. Lett.* **99**, 1–4 (2011).
121. Cho, S., Lee, K. & Heeger, A. J. Extended lifetime of organic field-effect transistors

- encapsulated with titanium sub-oxide as an 'Active' passivation/barrier layer. *Adv. Mater.* **21**, 1941–1944 (2009).
122. Bharti, B., Kumar, S., Lee, H. N. & Kumar, R. Formation of oxygen vacancies and Ti³⁺ state in TiO₂ thin film and enhanced optical properties by air plasma treatment. *Sci. Rep.* **6**, 1–12 (2016).
123. Zheng, L., Wang, C., Shu, Y., Yan, X. & Li, L. Utilization of diatomite/chitosan–Fe (III) composite for the removal of anionic azo dyes from wastewater: Equilibrium, kinetics and thermodynamics. *Colloids Surfaces A Physicochem. Eng. Asp.* **468**, 129–139 (2015).
124. Mozafari, M. *et al.* Synthesis and characterization of electrospun polyvinyl alcohol nanofibrous scaffolds modified by blending with chitosan for neural tissue engineering. *Int. J. Nanomedicine* **25** (2012). doi:10.2147/ijn.s25376
125. Meneses, C. *et al.* Physical Characterization of TiO_x layers deposited from sol-gel technique. *Chip Curitiba 2013 - SBMicro 2013 28th Symp. Microelectron. Technol. Devices* 1–4 (2013). doi:10.1109/SBMicro.2013.6676158
126. Mazurek, P., Daugaard, A. E., Skolimowski, M., Hvilsted, S. & Skov, A. L. Preparing mono-dispersed liquid core PDMS microcapsules from thiol-ene-epoxy-tailored flow-focusing microfluidic devices. *RSC Adv.* **5**, 15379–15386 (2015).
127. Mrad, N. A. *et al.* Laboratory experimental simulations: Chemical evolution of the organic matter from interstellar and cometary ice analogs. *Bull. la Soc. R. des Sci. Liege* **84**, 21–32 (2015).

128. Liu, Y. *et al.* Effective hot-air annealing for improving the performance of perovskite solar cells. *Sol. Energy* **146**, (2017).
129. Chen, Q. *et al.* Planar heterojunction perovskite solar cells via vapor-assisted solution process. *J. Am. Chem. Soc.* **136**, 622–5 (2014).
130. Sun, X. *et al.* Mixed-solvent-vapor annealing of perovskite for photovoltaic device efficiency enhancement. *Nano Energy* **28**, 417–425 (2016).
131. Eperon, G. E. *et al.* The Importance of Moisture in Hybrid Lead Halide Perovskite Thin Film Fabrication. *ACS Nano* **9**, 9380–9393 (2015).
132. Bass, K. K. *et al.* Influence of moisture on the preparation, crystal structure, and photophysical properties of organohalide perovskites. *Chem. Commun.* **50**, 15819–15822 (2014).
133. You, J. *et al.* Moisture assisted perovskite film growth for high performance solar cells. *Appl. Phys. Lett.* **105**, 183902 (2014).
134. Pisoni, A. *et al.* Ultra-Low Thermal Conductivity in Organic–Inorganic Hybrid Perovskite $\text{CH}_3\text{NH}_3\text{PbI}_3$. *J. Phys. Chem. Lett.* **5**, 2488–2492 (2014).
135. Zhang, W. *et al.* Ultrasmooth organic-inorganic perovskite thin-film formation and crystallization for efficient planar heterojunction solar cells. *Nat. Commun.* **6**, (2015).
136. Wang, T. *et al.* Indirect to direct bandgap transition in methylammonium lead halide perovskite. *Energy Environ. Sci.* **10**, 509–515 (2017).

137. Zhu, W. *et al.* Facile Face-Down Annealing Triggered Remarkable Texture Development in CH₃NH₃PbI₃ Films for High-Performance Perovskite Solar Cells. *ACS Appl. Mater. Interfaces* **9**, 6104–6113 (2017).
138. Koster, L. J. A., Mihailetschi, V. D., Xie, H. & Blom, P. W. M. Origin of the light intensity dependence of the short-circuit current of polymer/fullerene solar cells. *Appl. Phys. Lett.* **87**, 1–3 (2005).
139. Song, X. *et al.* Controlling Blend Morphology for Ultrahigh Current Density in Nonfullerene Acceptor-Based Organic Solar Cells. *ACS Energy Lett.* **3**, 669–676 (2018).
140. Zhang, X. *et al.* Understanding charge transport and recombination losses in high performance polymer solar cells with non-fullerene acceptors. *J. Mater. Chem. A* **5**, 17230–17239 (2017).
141. Su, W. *et al.* Efficient ternary blend all-polymer solar cells with a polythiophene derivative as a hole-cascade material. *J. Mater. Chem. A* **4**, 14752–14760 (2016).

Acknowledgements

이 논문이 나오기까지 정말 많은 분들의 도움이 있었습니다. 물리학 박사라는 어릴 적부터 동경해 왔던 학위를 얻기까지 저를 도와주셨던 많은 분들께 이렇게나마 감사의 말씀을 드리고자 합니다.

먼저, 언제나 지도와 격려를 아끼지 않으시는 지도 교수님이신 박성흠 교수님께 깊은 감사를 드립니다. 제가 물리학 박사학에 대한 막연한 동경심으로 처음 박성흠 교수님 방의 문을 두드린지 벌써 8년이 흘렀습니다. 아직 교수님의 수업을 수강한 적이 없었던 저였지만, 함께 고민하며 응원해주시던 진심 어린 말씀에 대학원 진학을 결심하게 되었습니다. 정말 어려모로 미숙하고 실수도 잦았던 저에게 항상 큰 기대와 격려 그리고 지원을 아끼지 않으시고 나아갈 길을 알려주셨던 교수님이 계셨기에 학위과정을 끝까지 해낼 수 있었습니다. 아직 갈 길이 멀지만 박사 학위에 걸맞는 한 사람의 연구자로서 교수님의 기대와 가르침에 부응 할 수 있도록 계속 노력하겠습니다.

항상 관심과 격려를 아끼지 않으셨던 정윤경 교수님과 이보람 교수님께도 감사 드립니다. 바쁘신 중에도 마치 지도교수님처럼 저의 연구와 논문에 많은 도움을 주시고, 관심 가져주셔서 감사합니다. 친근히 건네 주시던 말씀 한마디가 제겐 큰 힘이 되었습니다.

바쁘신 와중에도 저의 학위 논문 심사에 기꺼이 시간을 내어 자리해 주신 정중현 교수님, 손세모 교수님, 박운익 교수님께도 감사의 말씀을 드립니다. 저의 연구와 진로에 대해 해 주셨던 조언, 정말 감사 드립니다. 심사가 끝나고 악수를 건네며 해 주셨던 축하의 말씀은 평생 잊지 못할 것 같습니다. 인정해 주신 학위에 걸맞는 한 사람의 연구자가 되도록 항상 정진하겠습니다.

연구를 진행함에 있어 많은 조언과 도움을 주셨던 조신욱 교수님과 황인욱 박사님께도 감사의 말씀을 드립니다. 실험과 측정에 필요한 도움을 아끼지 않으셨고, 또한 저에게 해 주셨던 조언은 연구를 진행함에 있어서 정말 큰 도움이 되었습니다.

또한 석사과정을 처음 시작할 무렵부터 많은 연구를 함께 진행했던 Tamilavan 박사님과 Agneeswari 박사님에게 감사를 전합니다. 마치 실험실 선배처럼 제가 연구를 처음 시작할 무렵부터 해 주셨던 조언과 함께한 연구는 화학에 무지하던 제가 고분자태양전지와 다양한 기능성소재에 대해 연구를 진행하는 데 정말 큰 도움이 되었습니다.

저에게 새로운 분야의 경험을 얻게 해 준 Anshuman Roy 박사님에게도 감사를 전합니다. 경험도 지식도 부족하던 저를 한 사람의 연구자로 대해주었고, 중성자탐지라는 새로운 분야에서 많은 경험을 쌓을 기회를 주었습니다. 박사님과 함께 연구를 진행한 시간들은 제게 정말 값진 경험이 되었습니다.

석사시절부터 함께 동고동락했던 지훈이 형, 그리고 이제는 오랜 친구 같은 실험실 동생 경환, 승민, 서로 실험실 생활에서 시답잖은 이야기부터 연구논문의 고민까지 상담해 주던 달용, 누구보다 열심히 실험하고 또 많은 연구를 함께하며 도움을 주었던, 하지만 여러모로 속 썩이던, 손 많이 가는 동생 Liang, 묵묵히 열심히 하는 모범스러운 후배 Chao, Yuan, 그리고 연구와 실험, 그리고 졸업준비를 헌신적으로 도와주었고, 연구 내적으로나 외적으로 대학원 생활에 버팀목이 되어준 후배 단비, 현석, Pesi, 그리고 오랜시간 실험실에서 가족처럼 지내온 후배 근녕, 소영, 은혜, 동근 모두에게 정말 감사합니다. 여러분 덕분에 학위과정 동안의 실험실 생활이 제게 좋은 추억이 되었습니다. 실험실은 다르지만 대학원 생활 동안 함께 동고동락했던 연우누나, 현미누나, 지철, 승훈, 창목, 주현, 미선, 현정, 도림, Kai, 병찬, 옥희에게도 고맙다는 말을 전하고 싶습니다.

매번 제가 바쁘다는 핑계로 자주 보지 못해도 늘 응원해주고 늦은 시간 푸념 섞인 전화 받느라 고생한 친구 유민, 정훈 에게도 늘 고맙다는 말을 전하고 싶습니다.

마지막으로 오랜 시간 동안 제가 학업에 전념할 수 있도록 믿고 지원해 주신 우리 가족에게 감사를 전합니다. 항상 저를 믿고 성원을 보내주시는 가족이 있었기에 저는 물리학 박사라는 꿈을 이룰 수 있었습니다. 앞으로 성원에 부끄럽지 않은 모습을 보여드릴 수 있도록 노력하겠습니다. 정말 감사합니다.



2020. 1.

신인수 올림